Orbital Observations of Dust Lofted by Daytime Convective Turbulence

Orbital Observations of Dust Lofted by Daytime Convective Turbulence

Lori Fenton

SETI Institute, 189 Bernardo Ave. Suite 100, Mountain View, CA, 94043, USA
Phone: (650) 810-0121
Fax: (650) 962-9419
Email: lfenton@seti.org

Dennis Reiss

Institut für Planetologie, WWU Münster
Email: dennis.reiss@uni-muenster.de

Mark Lemmon

Texas A&M University
Email: lemmon@tamu.edu

Béatrice Marticorena

Laboratoire Interuniversitaire des Systèmes Atmosphériques (LISA)
Email: Beatrice.Marticorena@lisa.u-pec.fr

Stephen Lewis

The Open University
Email: stephen.lewis@open.ac.uk

Bruce Cantor

Malin Space Science Systems
Email: cantor@msss.com

Abstract:

Over the past several decades, orbital observations of lofted dust have revealed the importance of mineral aerosols as a climate forcing mechanism on both Earth and Mars. Increasingly detailed and diverse data sets have provided an ever-improving understanding of dust sources, transport pathways, and sinks on both planets, but the role of dust in modulating atmospheric processes is complex and not always well understood. We present a review of orbital observations of entrained dust on Earth and Mars, particularly that produced by the dust-laden structures produced by daytime convective turbulence called "dust devils". On Earth, dust devils are thought to contribute only a small fraction of the atmospheric dust budget; accordingly, there are not yet any published accounts of their occurrence from orbit. In contrast, dust devils on Mars are thought to account for several tens of percent of the planet's atmospheric dust budget; the literature regarding martian dust devils is quite rich. Because terrestrial dust devils may temporarily contribute significantly to local dust loading and lowered air quality, we suggest that martian dust devil studies may inform future studies of convectively-lofted dust on Earth.

As on Earth, martian dust devils form most commonly when the insolation reaches its daily and seasonal peak and where a source of loose dust is plentiful. However this pattern is modulated by variations in weather, albedo, or topography, which produce turbulence that can either enhance or suppress dust devil formation. For reasons not well understood, when measured from orbit, martian dust devil characteristics (dimensions, and translational and rotational speeds) are often much larger than those measured from the ground on both Earth and Mars. Studies connecting orbital observations to those from the surface are needed to bridge this gap in understanding. Martian dust devils have been used to remotely probe conditions in the PBL (e.g., CBL depth, wind velocity); the same could be done in remote locations on Earth. Finally, martian dust devils appear to play a major role in the dust cycle, waxing and waning in relative importance and spatial patterns of occurrence with the planet's orbital state. Orbital studies of terrestrial dust devils would provide a basis for comparative planetology that would broaden the understanding of these dusty vortices on both planets.

Keywords: Atmospheric dust; dust devil; Mars; dust storm; boundary layer

Abbreviations: ADEOS: Advanced Earth Observing Satellite; AOT: aerosol optical thickness; ASTER: Advanced Spaceborne Thermal Emission Spectrometer; AVHRR: Advanced Very High Resolution Radiometer; CALIOP: Cloud-Aerosol Lidar with Orthogonal Polarization; CALIPSO: Cloud-Aerosol Lidar and Infrared Pathfinder Satellite Observations; CBL: convective boundary layer; CTX: Context Camera; DD: dust devil; DOD: dust optical depth; DOT: dust optical thickness; EPF: emission phase function; EY: Earth year; FOV: field of view; GCM: global circulation model; GLAS: Geoscience Laser Altimeter System; GLI: Global Imager; GOCART: Goddard Chemistry Aerosol Radiation and Transport; HiRISE: High Resolution Imaging Science Experiment; HRSC: High Resolution Stereo Camera; ICESat: Ice, Cloud and land Elevation Satellite; IR: infrared; IRIS: Infrared Interferometric Spectrometer; IRTM: Infrared Thermal

Mapper; LITE: Lidar In-Space Technology Experiment; LW: long wave; MARCI: Mars Reconnaissance Orbiter Mars Color Imager; MCS: Mars Climate Sounder; MEX: Mars Express; MGS: Mars Global Surveyor; MOC NA: Mars Orbiter Camera Narrow Angle; MOC WA: Mars Orbiter Camera Wide Angle; MODIS: Moderate-resolution Imaging Spectro-radiometer; MOLA: Mars Orbiter Laser Altimeter; MRO: Mars Reconnaissance Orbiter; MSG: Meteosat Second Generation; MSL: Mars Science Laboratory; Multi-angle Imaging Spectro-Radiometer; MY: Mars Year; MVIRI: Meteosat Visible Infra-Red Imager; NOAA: National Oceanic and Atmospheric Administration; ODY: Mars Odyssey; PBL: planetary boundary layer; POLDER: Polarization and Directionality of the Earth's Reflectances; PSD: particle size distribution; SeaWiFS: Sea-viewing Wide Field of view Sensor; SRC: Super-resolution Camera; SEVIRI: Spinning Enhanced Visible Infra-Red Imager; SPICAM: Spectroscopy for Investigation of Characteristics of the Atmosphere of Mars; SW: short wave; TES: Thermal Emission Spectrometer; THEMIS IR: Thermal Emission Imaging System, Infrared camera; THEMIS VIS: THEMIS Visible camera; TIROS: Television and Infra-Red Observation Satellite; UV: ultraviolet; VCS-MA: Vidicon Camera System – Medium Angle; VIS: TOMS: Total Ozone Mapping Spectrometer; Visual Imaging Subsystems; VL1: Viking Lander 1; VL2; Viking Lander 2; VO1: Viking Orbiter 1; VO2: Viking Orbiter 2

1 Introduction

Spaceborne observations of lofted dust began with the first weather satellites in the 1960s (see Figure 1a). Until recently, most such phenomena have been associated with dust hazes and smog that have been transported far from their source regions (e.g., United States 1964), but new data have highlighted a complex interplay between dust emission and daytime dry convective turbulence in the planetary boundary layer. The CBL is composed of structured turbulent eddies, containing tens-of-meter-scale vortices that form most commonly in narrow updrafts at the intersections of three or more kilometer-scale convection cells (e.g., Willis and Deardorff 1979; Hess and Spillane 1990; Kanak et al. 2000). When dust-laden, these vortices become visible to the eye as dust devils (DDs). Non-rotating gusts may also entrain dust, likely occurring most commonly along upwelling sheets where two convection cells meet. For a detailed review of the meteorological context of convectively-lofted dust, we refer the reader to Chapters 5 and 7 of this volume.

On Earth, the amount of dust lofted by daytime convective turbulence, mainly by DDs, was first estimated by Koch and Renno (2005) to be ~0.7 Tg/year, or 34 ± 19% of the global terrestrial mineral dust budget. Jemmett-Smith et al. (2015) revised this estimate down to only ~3.4% of the global terrestrial mineral dust budget by refining estimates of the temporal and spatial occurrence of dust entrainment. Although small, this input could be significant on a regional scale (e.g., Gillette and Sinclair 1990; Jemmett-Smith et al. 2015), with potentially significant environmental consequences and hazards (Goudie and Middleton 2006). DDs have not yet been identified in images obtained from terrestrial satellites, although the tracks they sweep out on the surface have been studied (see Sec. 3.1 and Chapter 4). The continued monitoring of such features from orbital platforms opens new avenues of research that, informed by the extensive studies performed on Mars, could prove to be of use to the field of terrestrial climate science.

Dust on Mars has long been known from Earth-based telescopic observations; Martin and Zurek (1993) summarized observations of “yellow clouds” dating as far back as 1873. These phenomena were correctly attributed to lofted dust, but the determining details of their formation, development, and dissipation required a closer inspection from orbiting spacecraft. The best first look at martian dust from space is that from Mariner 9, which entered orbit

around Mars in November 1971, in the midst of one of the most intense planet-encircling dust storms on record (see Figure 1b). Features related to dust entrained by sub-kilometer-scale daytime convective turbulence, such as DDs, were not expected to be resolved in images from 1970s-era spacecraft; as a result they were only identified many years later after careful inspection of these data sets (Thomas and Gierasch 1985).

We present a review of atmospheric dust research from orbital spacecraft, both on Earth and Mars, with a particular emphasis on DDs. This chapter is complementary to a review of field measurements, which can be found in Chapter 2. We first summarize the orbital platforms used and the observed spatial and temporal patterns of dust lifting and transport, in part to provide a context for the DD studies, but also because instrument capabilities dictate what may be learned from the data sets they produce. We then describe the current body of literature on orbital observations of martian DDs, including regional and global surveys, spatial and temporal patterns of their occurrence, physical characteristics, their relation to the martian dust cycle, and the potential role of convectively-lofted dust as a climate forcing mechanism (a more detailed discussion of how dust lofted by DDs relates to the climate system can be found in Chapter 11). The conclusions begin with a comparison of global mean estimates of dust load, the contribution contributed by DDs, and the DOT, providing a high-level comparison of the quantity of atmospheric dust on Earth and Mars. This is followed by a summary of the major knowledge gaps that could be addressed with use of orbital data. In particular, we emphasize that, although observations of terrestrial DDs from space have yet to be reported, the extensive surveys and detailed investigations from Mars suggest that similar work on Earth could be quite informative.

The martian year is 668.6 sols (martian days) long, nearly twice as long as that of the Earth. An annual "calendar" for Mars is denoted by the solar longitude, or L_s, in which the year begins at the northern vernal equinox ($L_s = 0^o$) and circumscribes its orbit around the sun over the following 360º (i.e., northern summer solstice occurs at $L_s = 90^o$, autumnal equinox occurs at $L_s = 180^o$, and northern winter solstice occurs at $L_s = 270^o$). Mars years (MY) are numbered beginning with MY 1 on 11 April, 1955, following the convention of Clancy et al. (2000); a convenient tool for converting Earth dates to Martian dates can be found at http://www-mars.lmd.jussieu.fr/mars/time/martian_time.html. Because the martian sol is 24 hours, 39 minutes, and ~35.2 seconds long, the convention is to divide the day into 24 "hours" that are

~3698.7 seconds in duration. Lacking oceans, Mars has no equivalent elevation for sea level, so the topographic datum is defined as the equipotential surface at the mean equatorial radius (3396.2 km), which is located at a pressure level of ~520 Pa at $L_s = 0^o$ (Smith et al. 2001).

2 Orbital Measurements of Lofted Dust

2.1 Earth

2.1.1 Aerosols on Earth

Compared to Mars, sources of atmospheric particulate matter (aerosols) are numerous on the Earth. Primary aerosols, directly emitted as particles, are distinguished from secondary aerosols, resulting from chemical or physical transformation of gaseous precursors (e.g., Boucher et al. 2013). Primary aerosols are produced by the mechanical action of the atmosphere on the surface: over the continents, it produces mineral dust (see Figure 2); over the sea, it produces sea salts. Secondary aerosols are produced by the combustion of biomass and all types of fuels, as well as by chemical reactions of gases naturally emitted by vegetation, oceanic surfaces, and volcanic activity. In terms of radiative forcing and health impacts, most of the scientific attention is focused on secondary aerosols resulting from human activities, because of the aerosols' size (mostly <~1μm) and composition. In terms of annual emissions, mineral dust (emitted in arid and semi-arid regions) and sea-salts are the most abundant aerosols on the Earth, with annual emissions estimated respectively to 1000-4000 Tg and 1400-6800 Tg (Boucher et al. 2013). Total anthropogenic annual emissions are of the order of 400 Tg, whereas the atmospheric input of cosmic dust in the terrestrial atmosphere is estimated to be 0.0018 to 0.1 Tg yr^{-1}, based on daily input reported by Plane (2012). Aerosols emitted in the terrestrial troposphere have lifetimes of a few days, indicating that the concentrations of the different aerosols are not homogeneously distributed. Aerosols are often subjected to transport ranging from tens to thousands of kilometers, but the highest concentrations are observed within and immediately downwind of their source regions. In addition, different aerosol sources are located in different geographic areas, producing regions with different dominant aerosol types: mineral dust is prevalent downwind of the main desert areas (North Africa, Asia, etc.), sea salts are common over sea-surfaces and remote coastal areas, and anthropogenic aerosols form over the developed and developing countries of the northern hemisphere. Figure 3 shows a global map of AOT retrieved from MISR data over a 5 year period, showing regions of strong aerosol emission on continents and its transport over both land and water.

Different aerosols interact with radiation in different ways: many of them (e.g., sulfates, nitrates, organic aerosols) primarily backscatter solar radiation, but a few types have strong absorption properties (e.g., carbonaceous aerosols). Mineral dust has the capacity not only to backscatter radiation in the visible range, but also to absorb radiation in the IR and UV range (e.g., Redmond et al. 2010). Regarding the variety of different aerosols and the geographic distribution of their sources, detection from orbital platforms is a powerful tool for investigating the spatial and temporal variability of the atmospheric content (Lenoble et al. 2013; Chiapello 2014).

2.1.2 Orbital Platforms

Quantitative measurements of the atmospheric aerosol load, and of particular interest to this review, mineral dust, can be derived from satellite measurements of backscattered radiation; many commonly-used instruments are listed in Table 1. The columnar extinction of solar radiation by atmospheric aerosols is quantified by the AOT (or equivalently, the AOD). For a given aerosol type, and assuming homogeneous properties exist along the atmospheric column, the AOT is proportional to the vertically-integrated atmospheric concentration weighted by the extinction efficiency. The extinction efficiency is itself largely controlled by the aerosol size distribution and composition.

The first operational algorithms to detect and quantify the aerosol atmospheric load from instruments onboard satellite platforms were developed in the 1990s and applied to observations from weather satellites: the European Meteosat (Jankowiak and Tanré 1992) and the American NOAA AVHRR (Swap et al. 1996; Husar et al. 1997). The AOT derived at the global scale revealed that desert dust is responsible for the largest and most persistent aerosol loads over the world's oceans (Herman et al. 1997; Husar et al. 1997).

For many years, the retrieval of AOT was restricted to surfaces with low albedo, and in particular, to oceanic surfaces. As an alternative, indicators of the presence of an absorbing aerosol (carbonaceous aerosols and mineral dust) have been developed based on measurements both in the UV (Herman et al. 1997; Torres et al. 1998) and in the IR (Legrand et al. 1994; 2001). These aerosol indices have been used widely, in particular for mineral dust source identification (i.e., Prospero et al. 2002). Sensors of novel generation, with spectral capabilities or additional types of measurements (i.e. polarization, several view angles), have significantly

increased the capacity to characterize the different aerosol types and to retrieve AOT over land surfaces (e.g., Martonchik et al. 2004). As an example, the MODIS data subsets from Collection 5 includes the retrieval of aerosols over "dark targets", i.e., surfaces dark enough to enable the separation of the surface and aerosol signals, such as vegetated areas. For mineral dust studies, the recent developments for the retrieval of AOT over bright desert surfaces (e.g., the "Deep Blue" algorithm by Hsu et al. 2004; 2013) offers new perspectives on the investigation of dust emission and dust storms inside and close to source regions. AOT can also be retrieved from IR observations of the SEVIRI instruments onboard the Meteosat Second Generation (Banks and Brindley 2013; Carrer et al. 2014).

Retrieved AOTs may differ depending on the instrument and the algorithm. In addition, temporally-averaged AOTs can vary from one sensor to another depending on the temporal sampling. Typically, satellites in geostationary orbits provide higher sampling rates than polar-orbiting satellites, but for limited regions. Another limitation is that AOT retrieval from satellites is still generally constrained to clear-sky conditions.

Most of the algorithms applied to satellite sensors allow the retrieval of the AOT with an uncertainty that has been significantly reduced from that of early sensors (Meteosat, AVHRR) relative to that of the current satellite missions, which are dedicated to aerosol research (e.g., sensors from the A-Train: MODIS, MISR, POLDER). These new sensors allow the retrieval of additional parameters that provide information on aerosol size, shape or optical properties. The spectral dependence of the AOT, known as the Angström coefficient, can be used to discriminate aerosols of different size distributions. Aerosols with a significant coarse mode, such as mineral dust or sea salt, have Angström coefficient values close to 0, whereas aerosols dominated by fine-mode particles, such as particles from fossil fuel combustion and biomass burning, have Angström coefficients higher than 1. Simultaneous information on AOT and Angström coefficients can thus be used to estimate the atmospheric load of mineral dust containing large amounts of coarse particles. Some of the recent sensors enable discrimination of the contribution of fine and coarse modes to the total AOT (e.g., MODIS), which, for example, helps to distinguish fine pollution aerosols from coarse mineral dust. Aerosol retrieval from the POLDER instrument can be used to distinguish spherical and non-spherical aerosols within the coarse mode (Herman et al. 2005), and thus further refine the detection of mineral dust (Tanré et al. 2011; Peyridieu et al. 2010). Several parameters (Angström exponent, size fraction, absorption), especially those derived from MODIS data, can be combined to separate

the different types of aerosols (Kaufman et al. 2005; Ginoux et al. 2012). However, the unambiguous identification of dust is still challenging, particularly in regions where dust can be mixed with other optically active species (e.g., biomass burning aerosols). It must also be noted that most of these aerosol products are available from instruments onboard polar-orbiting platforms, providing one observation per day at one time of the day. This orbital configuration is relevant for documenting medium to long-range transport of mineral dust, identifying source regions, and for climatological studies, but it is not well-suited to monitoring specific dust storms at regional and local scales. Spatial resolution is also an issue, with the AOT collection most frequently binned to a spatial resolution on of the order of 1º. The spatial and temporal resolution provided by geostationary platforms is much higher. Color composites of observations from SEVIRI instruments onboard the MSG satellites have been widely used to monitor dust events over the Sahara and the Sahel either for large continental dust storms (e.g. Slingo et al. 2006) or to identify dust plumes associated with mesoscale convective systems (e.g. Marticorena et al. 2010). The AOT over land, including desert surfaces, can be retrieved from SEVIRI measurements with a nadir spatial resolution of 3 km, as well as an extra high-resolution visible channel at a nadir resolution of 1 km (Banks and Brindley 2013).

In parallel with the development of new, but vertically-integrated, aerosol products, lidar techniques have been developed both from ground-based and airborne platforms. They provide the unique opportunity to document the vertical structure of mineral dust distribution. The first lidar observations of dust from space were provided by LITE, which flew on the Space Shuttle Discovery in 1994 (e.g, Berthier et al. 2006), and GLAS, on ICEsat (Spinhirne et al. 2005), although it is interesting to note that these sensors were preceded by the original MOLA on the failed Mars Orbiter mission (Zuber et al. 1992). Since 2006, lidar aerosol and cloud observations have been available from the CALIPSO mission (Winker et al. 2010). The CALIOP lidar onboard CALIPSO measures aerosol profiles with a 30 m vertical resolution and 70 m horizontal resolution, and thanks to depolarization measurements, it enables aerosol classification, including identification of nonspherical particles typified by mineral dust (Omar et al. 2009).

2.1.3 Spatial and temporal patterns of dust lifting

From satellite observations, significant progress has been made regarding specific dust transport events, including determining their regional transport patterns, seasonal and interannual variability, and long-term trends in relation to climatic conditions or change in

anthropogenic pressure. Climatology of aerosols and/or mineral dust has been extensively investigated with different aerosol products, from the "historical" weather sensors (Meteosat, AVHRR) and from dedicated sensors (e.g., Remer et al. 2008). The transport of mineral dust from the Sahara, the most intense dust source on Earth, has been the most frequently studied, allowing, for example, identification of the synoptic conditions associated with its transport pattern over the Atlantic Ocean (Huang et al. 2010). Lidar observations from CALIOP have been used to estimate the flux of the Saharan dust exported along this pathway (Yu et al. 2015). A re-analysis of the SeaWiFS decadal data set has been performed with the "Deep Blue" algorithm to analyze the trends in the variation of aerosols, including mineral dust, both over oceanic and continental surfaces of the world (Hsu et al. 2012). Since AOT retrieval can be performed only in clear-sky conditions, dust transport from other source regions can be difficult to detect. This is the case, for example, for dust coming from sources at high latitudes in the southern hemisphere, where the viewing geometry is not always ideal and bright sea ice interferes with AOT retrieval (e.g., Gasso and Stein 2007). However, dust has also been detected by remote sensing at high latitudes, such as in Alaska, New Zealand or Iceland (Prospero et al. 2012). The distribution of the main sources of desert dust on the Earth has been investigated using the TOMS aerosol index with a spatial resolution of 1°×1.25° (Prospero et al. 2002). To investigate the link between dust emission occurrence and meteorological processes, Shepanski et al. (2009) used a combination of aerosol index and AOT retrieval in the IR with a 15-min timescale at 1°×1° resolution. Over time, there has been a trend toward the production of ever-higher resolution products, largely motivated by the need for aerosol retrievals over continental urban areas for air quality applications. As an illustration, the Collection 6 algorithm that produces MODIS aerosol products includes, in addition to the standard retrieval at a resolution of 10 km×10km, a new product with a resolution of 3km×3km (Levy et al. 2013). The AOTs derived from SEVIRI are also available in the native geographical projection of MSG/SEVIRI (AERUS-GEO product, Carrer et al. 2014).

Figure 4 illustrates continental regions prone to high aerosol concentrations that are either entrained locally or transported from elsewhere (Ginoux et al. 2012). Areas of high optical depth include the Sahara and Sahel deserts, the Middle East, northern India, the coasts of the Aral and Caspian seas, basins in central Asia, the Lake Eyre Basin in Australia, and deserts in Namibia, Chile, and Peru. Prospero et al. (2002) found that most sources of mineral dust are located in topographic depressions that contain deep alluvial and lacustrine deposits subject to (and often built by) episodes of flooding. Because of the higher proportion of land coverage,

the northern hemisphere is dustier than the southern hemisphere. In most areas, the dusty season occurs in local spring and/or summer, with the season of minimum dust occurring in local autumn (e.g., Ginoux et al. 2012).

Monitoring interannual variations in dust loading has shed some light on the forcing mechanisms that control dust entrainment and transport. Most multi-year studies have focused on dust transport from northern Africa over the north Atlantic (Chiapello 2014). Years with increased dust in the north Atlantic correlate with lower rainfall rates in the Sahel during the preceding year (Prospero and Lamb 2003; Moulin and Chiapello 2004; Chiapello et al. 2005). For example, long-term measurements indicate a peak in dustiness over the north Atlantic in the 1980s that has declined in the years since (Foltz and McPhaden 2008; Evan and Mukhopadhyay 2010). This decline in DOD/AOT corresponds with an increase in rainfall in the Sahel since the mid-1980s (Chiapello 2005), which may have increased vegetation cover, thus reducing dust emission (Cowie et al. 2013). However, Chin et al. (2014) proposed that dust emission decreased instead as a result of reduced wind speeds in north Africa, driven by increased sea surface temperatures in the North Atlantic. Establishing a causal relationship between observed trends is critical for understanding the role of aerosols in the Earth's climate system.

2.1.4 Changed perspectives on the role of dust in the terrestrial climate system?

Figure 3 and Figure 4 show the spectacular extent of mineral dust plumes and the fact that mineral dust is responsible for the highest measured AOT on Earth. The analysis of a long time-series from orbital observations highlights the interannual variability of the dust content and multidecadal trends in relation with climatic parameters. In addition, satellite observations have been used to estimate the impact of aerosol forcing. For example, based on multiple satellite data sets and a radiative model, Zhu et al. (2007) estimated the shortwave (visible) and longwave (IR) radiative impact of dust downwind of the three largest mineral dust source regions: eastern Asia, the Arabian Peninsula and the Sahara Desert. The mean seasonal and regionally-averaged reduction of radiative flux (visible+IR) at the surface has been estimated in clear-sky conditions to be 5.9 W m^{-2}, 17.8 W m^{-2}, and 14.2 W m^{-2}, over the Yellow Sea, the Arabian Sea and the west African coasts, respectively. The relative contributions of shortwave and longwave heating both at the surface and at the top of the atmosphere have been estimated and found to be very different for these three regions. The dust plume over the Arabian Sea was found to produce the largest effect on atmospheric heating, mainly due to shortwave heating.

The maximum longwave effect on heating rates occurred over the western African coast downwind of the Sahara, resulting in strong cooling throughout the dust layer that offset up to 80% of the shortwave heating, with moderate heating below. Finally, the net radiative heating rate over the Yellow Sea is the smallest among these three regions. This heating or cooling effect can impact atmospheric dynamics at both local and synoptic scales. In the eastern Atlantic, Wong et al. (2009) suggested that Saharan dust contributed to about 50% of the detected heating rate anomalies and thus has a substantial impact on atmospheric stability. This effect is also suspected to influence the development of cyclones and may explain a possible inhibition on the formation of tropical cyclones, revealed by an anti-correlation between north tropical cyclone activity and Saharan dust cover (Evan et al. 2006).

Mineral dust, being of natural origin, is not accounted for in the estimation of the radiative forcing as defined by the IPCC, except for the fraction of the global dust load attributed to "anthropogenic" dust (i.e., that which is emitted from disturbed land). However, the large radiative effect of mineral dust and its variability in space and time must be accounted for in the estimation of the change in the aerosol load and its impact on climate. An analysis of global simulations and observations of multi-decadal (1980 to 2009) aerosol variations suggests that the strong variability of mineral dust emission and transport has partly dampened the changes in anthropogenic aerosol loads and highlights the fact that natural aerosols, such as mineral dust, play an important role in determining the regional and global aerosol budget, even over major pollution source regions (Chin et al. 2014). A comparison of the simulations of the mineral dust cycle by 15 global models, mainly driven by meteorological re-analysis, has been performed in the frame of the AeroCom project (Huneeus et al. 2011), and it shows large discrepancies between models. On average, the climatology of AOT due to mineral dust was reproduced to within a factor of two, and the surface concentrations and deposition were reproduced to within a factor of ten. The capacity of climatic models to reproduce the present-day AOT climatology is even lower (Evan et al. 2014). Further work is needed to understand the response of aerosols to, and their interaction with, Earth’s changing climate system (Boucher et al. 2013).

Paleoarchives from ice cores (e.g., Vallelonga and Svensson 2014), deep-sea sediments (e.g., Winckler et al. 2008) and loess sequences (e.g., Muhs et al. 2014) have revealed variations of the atmospheric dust load variations between glacial and interglacial periods (Maher et al. 2010), with dust concentrations at the Last Glacial Maximum (25 ka BP) of 80-100 times that of interglacials and the present-day. Understanding the link between the mineral dust cycle and

climate for past periods on Earth is still challenging. Uncertainties mainly arise from the need for climate models to properly represent dust emission processes and their link with surface properties (e.g., soils, vegetation, moisture, etc.) and the feedback that dust radiative effects can have on the climate, which are equally as complex as modeling the mineral dust cycle on Mars.

2.2 Mars

In this subsection we discuss our knowledge of aerosols in the martian atmosphere, how lifting has been observed from orbital platforms and the spatial and temporal variability of dust in the atmosphere that results. We briefly review, by comparison with the Earth, what orbital observations tell us about the role of convectively-lofted dust, such as that from DDs, in the martian climate system.

2.2.1 Aerosols on Mars

Many of the processes that create aerosols on Earth, such as sulfate emissions from volcanic eruptions and fossil fuel combustion, sea salt from spray, and smoke and soot from fires, do not occur on Mars (although volcanic eruptions and possibly sea salt spray contributed to atmospheric aerosols in the distant past). Failing to account for light scattering by atmospheric dust led early 20^{th} century efforts to overestimate the surface air pressure of Mars by more than a factor of five (Kieffer et al. 1992). Mineral dust is a major forcing mechanism in the martian atmosphere, and it is intimately linked with interannual variability in the martian climate (e.g., Zurek et al. 1992; Read and Lewis 2004). Lifting may be accomplished by winds linked to large-scale weather systems or atmospheric tides (Wang et al. 2003; Hinson and Wang 2010; Hinson et al. 2012; Wang and Richardson 2015), local mesoscale gusts or topographic flows (Spiga and Lewis 2010; Mulholland et al. 2015), or on much smaller scales by convective motions (Spiga and Forget 2009), such as the DDs (Balme and Greeley 2006; Greeley et al. 2010) that are the primary focus of this review.

The primary effect of martian dust is to provide local heating to the atmosphere through absorption of solar shortwave radiation. Dust in the atmosphere also absorbs, scatters and re-radiates radiation at longer wavelengths, such as thermal infrared emission originating from the surface (Smith 2004). The net effect is to warm the atmosphere where it is most dusty and in daylight, and to cool the surface below regions with very high dust opacity. If atmospheric dust loading varies from place-to-place, this may introduce or steepen horizontal temperature

gradients within the atmosphere that are, in turn, linked to winds. Winds in the atmosphere both advect dust and may lift more from the surface. In a heavily dust-laden atmosphere, the effect is to warm the atmosphere relative to the surface, which increases its static stability and tends to ultimately reduce both vertical convection during the day and large-scale wave-like instabilities, both reducing the likelihood of dust lifting from the surface and ultimately leading to the slow decay of planet-encircling dust events (e.g., Cantor 2007). In this way, atmospheric dust provides complex positive and negative feedbacks to the martian climate system.

Dust aerosols have an additional potential feedback as nuclei for cloud ice particles, which in turn impact atmospheric radiative heating and cooling (Montmessin et al. 2004; Wilson et al. 2008; Madeleine et al. 2012a; Hinson et al. 2014; Navarro et al. 2014; Steele et al. 2014a; 2014b), although, unlike on Earth, it seems likely that there will always be a sufficient supply of small dust particles on Mars to nucleate the relatively thin water ice clouds that have been observed (Heavens et al. 2010; Madeleine et al. 2012b). Clouds, in turn, may further increase the complexity of the climate feedbacks, by accelerating the removal of dust from the atmosphere by scavenging smaller particles, thereby enhancing the sedimentation rate (Madeleine et al. 2012a; Navarro et al. 2014).

2.2.2 Orbital Platforms

Spacecraft orbiting Mars with instruments useful for monitoring the dust aerosol distribution are listed in Table 2. The reader is referred to Snyder and Moroz (1992) for a review of the early reconnaissance of Mars including additional television camera and other instrumentation.

Most orbital observations of martian atmospheric dust have been made with nadir-viewing cameras that sense reflected solar light, or with spectrometers that sense thermal emissions of dust and gasses. The first quantitative observations came from the Mariner 9 Infrared Interferometric Spectrometer (IRIS), which provided 5-50 μm spectral coverage showing CO_2 and dust emission/absorption features that were used to monitor the decay of the 1971 planet-encircling dust storm (Hanel et al. 1972). CO_2 has a strong and distinctive 15-μm band that allows temperature sounding. Silicate dust has a 9-μm band that, with atmospheric temperature, can be used to derive column opacity. Orbital instruments tend to be least sensitive to boundary layer dust, as a strong temperature contrast with the surface is helpful in thermal emission

460 sounding. The Viking Orbiters made similar measurements with the IRTM. Martin (1986)
461 modeled the data using albedo from the solar channel, thermal inertia from 20-μm emission,
462 and gas and dust emissions from 7- to 15-μm channels, and derived a time-series of AOT that
463 compared well with contemporaneous Viking Lander data. IRTM data was used to characterize
464 the onset and decay of both planet-encircling dust storms (Martin and Richardson 1993).
465 Fenton et al. (1997) applied the Martin (1986) technique to IRIS data to quantify the decay of
466 the 1971 storm, showing that dust spatial distributions varied less as the storm decayed, with
467 exponential timescales ranging from 42 to 67 sols.
468
469 Contemporaneously, imaging of the surface was used for geologic mapping and meteorology.
470 The Viking Orbiters mapped the planet with two vidicon visible-light cameras (VIS). Solar
471 reflectance imaging of dust is hampered by the extensive dust coverage of the surface, so that a
472 low dust load in the atmosphere is difficult to distinguish. However, dust storms have been
473 distinguished due to color, morphology, and temporal changes. Baroclinic storms were
474 identified using imaging and thermal data from VO (Hunt and James 1979). Local and regional
475 dust storms were identified and confirmed as dust – rather than water ice – using color data,
476 with most occurring near perihelion and southern summer, including many at the receding cap
477 edge (Briggs et al. 1979). Orbital monitoring of martian atmospheric dust has been essentially
478 continuous since the arrival of MGS in 1997, with each orbiter carrying at least one imager (see
479 Table 2).
480 On polar orbiting spacecraft, cameras with limb-to-limb fields of view build up a daily map
481 over the course of ~12 2-hour orbits. MOC WA obtained daily global maps that have been used
482 to track the evolution of local, regional, and planet encircling dust storms (e.g., Cantor et al.
483 2001; Cantor 2007). Cantor et al. (2001) characterized the source regions of local and regional
484 dust storms, showing differences compared to the Viking era. Frontal storms frequently follow
485 the receding (springtime) polar cap (Wang and Fisher 2009). Regional storms tend to originate
486 in the low-lying Acidalia, Utopia, Arcadia, and Hellas Planitiae (Wang and Richardson 2015).
487 Storms exhibiting visible structures on the cloud tops have been interpreted to indicate regions
488 of active dust lifting; these features are most common in the low-lying planitiae that produce
489 regional storms (Guzewich et al. 2015). MARCI data have shown north polar region dust
490 storms at all times of year, but especially in early northern spring and mid-summer (Cantor et
491 al. 2010). Mars Daily Global Maps (MDGMs) allow the tracking of individual storms (see
492 Figure 5) and the aggregation of data over time. Figure 6 shows typical storm tracks, including

493 the north-to-south Acidalia, Arcadia, and Utopia cross-equatorial storms; and the Hellas and
494 Solis sources of southern east-west storm tracks.
495
496 In addition to imaging, thermal emission has been used to monitor atmospheric dust on each
497 orbiter. Interferometric sounders like IRIS comprise MGS TES and Mars Express PFS. Multi-
498 channel sounders like IRTM comprise ODY THEMIS IR and MRO MCS. MGS TES observed
499 thermal emission of dust and gas, and has been used to track the zonal and seasonal
500 development of the 9-μm AOT (Smith 2004). TES data show 3 Mars years of dust variations
501 (MYs 24-26), in context with temperature and water vapor and ice variations, and include one
502 planet-encircling dust storm (in MY 25). THEMIS has been used to obtain maps with 5
503 reflectance bands and 10 thermal emission bands (Christensen et al. 2004). The thermal bands
504 have allowed the cross-calibration with TES results and the temporal extension of the 9 μm
505 optical depth maps past the end of the MGS mission (Smith 2009). Unlike MGS, Odyssey, and
506 MRO, Mars Express is not in a circular or polar orbit and it samples varied local times each
507 periapse. However, the effects of dust storms on the thermal environment can still be studied;
508 for example, Määttänen et al. (2009) found that the thermal impact of one local dust storm was
509 confined to the lowest two scale heights. PFS data suggest the dust is well mixed with the gas
510 even far from dust storms, with a mean AOT of 0.25 at 0-km elevation (Zasova et al. 2005;
511 Grassi et al. 2007). In addition to nadir-looking measurements, MCS acquires multi-channel
512 radiometry in a limb-scanning geometry. It thus retrieves AOT as well as vertical profiles of
513 dust (Kleinböhl et al. 2009). Detached layers have been found with the vertical profiling,
514 helping to diagnose heating and circulation (Heavens et al. 2011). For comparison across bands,
515 the ratio of visible AOT to infrared AOT was determined by contemporaneous rover-based
516 observations to vary from about 3 in northern summer to about 1.3 during southern summer
517 dust storms, with the differences likely coming from different particle sizes (Lemmon et al.
518 2015).
519
520 Mars Express and MRO carry infrared reflectance mapping spectrometers, OMEGA and
521 CRISM, respectively. For the purpose of monitoring dust aerosols, these can function as
522 context imagers (Reiss et al. 2014). However, they have the advantage of additional gas
523 absorption bands, which enable vertical sounding. Further, they aim in differing directions, and
524 can image the same area in multiple viewing geometries (an emission phase function, or EPF,
525 sequence) or even image in a limb-viewing geometry. These capabilities are used to study

physical properties of the dust (e.g., Wolff et al. 2009) and the vertical distribution (Smith et al. 2013).

The first occultation spectrometer to orbit Mars, capable of vertical sounding of AOT from photometry of the Sun as it rose (or set) above the limb of the planet, was flown on the Soviet Phobos mission. During its short operational lifetime, the Phobos mission obtained 9 solar-occultation profiles, in 2 infrared channels, of the dust extinction at altitudes of 12-35 km (Korablev et al. 1993). These data suggested 1-2 μm dust existed in radiatively significant quantities at altitudes of 15-25 km. The Mars Express SPICAM has UV and IR channels, and operates in nadir mode and limb mode, as well as stellar (UV only) and solar occultation modes. Solar occultations have been used for a climatology of vertical distribution of the dust over 4 Mars years including the MY 28 (2007) planet encircling dust storm (Määttänen et al. 2013). Such observations traced the summer to winter dust transport pathway at high altitudes. Combining UV and IR occultation data allowed the particle size distribution (PSD) to be inferred. A bimodal size distribution was found, with a small mode unstable to coagulation and too large to be supplied by meteoric inflow, suggesting a continual supply of fine surface dust from DDs and other winds (Federova et al. 2014). An additional vertical sounder, MOLA, used nadir-looking LIDAR for altimetry. As a by-product, scattering from aerosols was also seen, showing column abundance, vertical extent, and relationship to clouds (Smith et al. 2001). MOLA tracked dust storms for 1.25 Mars years, including the MY 25 (2001) planet encircling dust storm, and identified dust-ice fogs and possible DDs (Neumann et al. 2003).

2.2.3 Spatial and temporal patterns of dust lifting

Having summarized observations made from spacecraft in the previous subsection, we now turn to a description of the dust loading of the martian atmosphere as observed from space. It is important to note first that although lifting processes are sometimes observed directly (e.g. Cantor et al. 2006) or inferred from the sudden growth of dust loading in a region (Cantor et al. 2001; Wang et al. 2003; Strausberg et al. 2005; Wang 2007; Wang and Richardson 2015) or by the texture of dust clouds (Guzewich et al. 2015), lifting is rarely observed directly and the observations are really of dust once it is airborne, and potentially after advection over large distances from its original source. Similarly, landed spacecraft may see passing DDs (Ferri et al. 2003; Greeley et al. 2010) or monitor changing background dust loading (Colburn et al. 1989; Smith and Lemmon 1999; Smith et al. 2004; Lemmon et al. 2015), without observing the lifting process. The sparse nature of the coverage in both space and time for Mars relative to

559 that of the Earth means that it is difficult to quantify the relative sizes and distributions of dust
560 lifting sources based on observations alone.
561
562 Martian dust is generally observed at either visible or infrared wavelengths. Earlier
563 observations of Mars dust, with particular emphasis on large and planet-encircling events were
564 documented by Martin and Zurek (1993). This record was later extended to include smaller and
565 regional storms using more detailed visible wavelength imaging from polar orbiters (e.g.,
566 Cantor et al. 2001; Cantor 2007; Wang 2007; Wang and Fisher 2009; Wang and Richardson
567 2015). The emphasis in all these studies is, however, on discrete dust storms. These occur
568 principally from northern hemisphere autumn equinox to spring equinox, i.e., throughout the
569 winter period. Dust loading is much lower and discrete storms are rarely observed throughout
570 the northern hemisphere summer half of the year (L_s = 0°–180°), which is the period when Mars
571 is presently furthest from the Sun (aphelion is close to L_s = 70°), and the circulation and winds
572 are at their least intense. It is during this period, when the atmosphere is relatively clear and the
573 surface-atmosphere thermal contrast is at its greatest, that convection (Petrosyan et al. 2011),
574 and so DDs (Rennó et al. 1998; Newman et al. 2002a; 2002b), are likely to be most active and
575 to contribute to the background dust levels that are observed.
576
577 Polar orbiters have also provided an almost continuous record of near-infrared dust optical
578 depths ranging from MGS/TES (Smith 2004), through ODY/THEMIS (Christensen et al.
579 2004), to more recent MRO/MCS observations (McCleese et al. 2010; Heavens et al. 2011a).
580 The MRO/MCS observations are limb soundings that include information on the vertical
581 distribution of the dust (Heavens et al. 2011b) in contrast to previous infrared soundings that
582 were mostly nadir observations of total dust opacity. MRO/MCS has revealed dust to be more
583 complex in its vertical distribution than previously suspected, with layering possibly related to
584 deep convective motions (Spiga et al. 2010; Rafkin 2012).
585
586 The observations described above are neatly summarized into an eight-year climatology of
587 martian dust by Montabone et al. (2015). Figure 7 shows the infrared column dust absorption
588 optical depth from this dataset, averaged over all longitudes, as a function of latitude and time
589 of year (L_s). The dust absorption optical depth was measured at 9.3 μm, and then normalized to
590 a consistent reference pressure of 610 Pa. This optical depth should be multiplied by about 2.6
591 to get an equivalent broadband visible dust total extinction. Two features are of particular note:
592 the variability in the timing and occurrence of the periods of high dust loading in northern

hemisphere winter (L_s = 180°–360°), in particular the planet-encircling dust events in MY 25 (2001) and MY 28 (2007); and the remarkable repeatability and much lower levels of dust loading in northern hemisphere summer (L_s = 0°–180°)

2.2.4 Changed perspectives on the role of dust in the martian climate system?

In contrast to those performed for Earth, the majority of recent martian dust observations have been made from space (mostly from orbiting spacecraft, but including images from the Hubble Space Telescope), with the exception of a handful of discrete surface landers and earlier telescopic observations from Earth (see Chapter 2 for further detail on dust observations from the martian surface). Hence, understanding of the role of dust on a global scale has been gradually accumulated primarily through orbital monitoring rather than any other source of observations, in direct contrast to the Earth. The major qualitative change in our understanding of dust on Mars has come from the increased temporal and spatial resolution of observations. Before the late 1970s, observations naturally tended to select the largest dust events only, since these could be most readily observed either by a ground-based telescope or from a spacecraft that was either on a fly-past or in a high orbit with limited resolution (Martin and Zurek 1993). Dust variability has now been observed over a much wider range of spatial and temporal scales with the advent of polar orbiting spacecraft in relatively low orbits carrying optical cameras, such as MGS/MOC and MRO/HiRISE and MARCI (Cantor et al. 2001; Cantor 2007; Bell et al. 2009; McEwen et al. 2010), and infrared sounders, such as MGS/TES, ODY/THEMIS and MRO/MCS (Smith et al. 2000; 2001; Christensen et al. 2004; Smith 2004; McCleese et al. 2010; Heavens et al. 2011a), and of landers with increasing spectroscopic capability (Smith et al. 2004). Despite this progress, many questions about the relative role of DDs within the martian dust cycle remain unanswered.

Considerable progress can be made through modeling the martian dust cycle (Newman et al. 2002a; 2002b; Basu et al. 2004; Newman et al. 2005; Basu et al. 2006; Kahre et al. 2006; Mulholland et al. 2013; 2015). These are discussed further in Chapter 11 of this volume. It is worth noting at this stage that different combinations of dust lifting schemes can be tuned to produce results that are very broadly in accordance with the observed dust opacity on Mars throughout the year (see Figure 8). Of these, Kahre et al. (2006) make a direct assessment that about one half of the total dust lifted through the year comes from their DD lifting sub-model, with the other half coming from near-surface wind stress lifting, including saltation processes. Newman et al. (2005) do not provide a comparable number, but an estimate from figures

included for their present day simulation suggests that a smaller, but perhaps not significantly so, fraction of the dust comes from their DD lifting model. An important caveat is that the total dust opacity has been broadly tuned to observations, but there is no guarantee that all the near-surface wind stress processes are properly accounted for in these moderate resolution models. The DD lifting sub-model may, in practice, also be accounting for small-scale winds, such as at the polar cap edges, that are missed by the models. The estimate of roughly half the total dust lifted being from DDs is therefore potentially an overestimate.

Finally, it can be noted that dust opacity measurements have begun to be assimilated into Mars GCMs. Early efforts (Montabone et al. 2005; Lewis et al. 2007) permit dust to be tracked in three dimensions even from sparse spacecraft observations, but are not yet sufficiently developed to isolate the various sources of dust at the surface unambiguously, although work is ongoing. Figure 8 demonstrates this by showing dust broadband visible optical depth, normalized to 610 Pa, at intervals of 4, 4, 4, 4, and 12 sols made during a regional dust storm in Noachis Terra in MY 23 (1997), at a time when MGS/TES was taking limited data (about one orbit per day) during its aerobraking hiatus observing phase. The plots are polar stereographic with the south pole at the centre, the equator at the edge, the prime meridian pointing upward and a grid spacing of 15° in latitude and 30° in longitude. The evolution of the dust in longitude as well as latitude can be tracked by the data assimilation technique.

3 Dust Devils

In this section we describe the discovery of prevalent DD formation as observed from orbiting spacecraft, primarily that on Mars. As with dust storms, the physical characteristics and spatio-temporal patterns of convectively-lofted dust tell a story about atmospheric conditions in the PBL, filling a gap in knowledge on Mars that is yet largely unaddressed on Earth.

3.1 Earth

Terrestrial DDs have not yet been observed directly with orbital data. Given their prevalence in orbital images of Mars, it is a mystery as to why none have yet been reported on Earth. Ground-based measurements suggest that they are wide enough to be visible in high resolution images (Balme and Greeley 2006; Lorenz 2011). A plot of the minimum martian dust devil diameter detected from imagers of varying spatial resolution shows that smaller dust devils are detected with finer resolution cameras (see Fig. 9); the same trend is likely present on Earth, implying that image resolution is not the problem. Note from Fig. 9 that the more extensive surveys are

more likely to identify smaller (and more plentiful) DDs, indicating that sample size is important for orbital DD detection (see Chapter 8 for further discussion of DD size distributions). There may be other factors at play in the failure to detect terrestrial DDs from orbit. For example, DDs form most frequently when insolation is at a maximum, whereas most high resolution imagers orbit sun-synchronously with equatorial crossing times ~10:30, before much DD activity gets underway. In addition, Earth is much more cloudy than Mars, which would inhibit DD detection from above (also, clouds are also likely to suppress DD formation). Despite these limiting factors, we propose that DDs should be visible in orbital images of arid landscapes on Earth, and that a search for their presence in images should be considered.

In contrast to direct DD detection, tracks of DD passages have been identified in orbital images in several desert regions on Earth. The first DD tracks on Earth were identified in ASTER images by Rossi and Marinangeli (2004) in the Ténéré Desert, Niger. Further DD tracks on Earth were found in publicly-available high resolution satellite images such as GeoEye, Quickbird, and WorldView through the web interfaces of Google Earth and Bing Maps. Neakrase et al. (2008; 2012) found DD tracks in the east-central Sahara, including southwestern Libya, southern Libya, northeastern Chad, and the Egypt-Libya border. Reiss et al. (2010) identified DD tracks in the Turpan depression desert (north-west China) and analyzed them in-situ (Reiss et al. 2010; 2011a). Hesse (2012) and Reiss et al. (2013) observed DD tracks in the coastal desert of southern Peru in orbital imagery, which were also analyzed in situ by Reiss et al. (2013). For further details on DD tracks, we refer the reader to Chapter 4.

3.2 Mars

The first orbital detections of DDs on Mars were found in VO images by Thomas and Gierasch (1985), although convective vortices had been previously identified on the surface, in temperature and wind data from VL1 and VL2 (Ryan and Lucich 1983). These discoveries were no surprise, with their presence having been previously predicted both from a theoretical standpoint and from observations of dust clouds (Ryan 1964; Neubauer 1966; Gierasch and Goody 1973). These early investigations from 1970s-era Viking data verified the suspected prevalence of insolation-driven free convection in the martian atmosphere, fueled by a superadiabatic layer near the surface.

691 Since those first observations, DDs have been observed by nearly every camera in orbit around
692 Mars; Figure 10 shows visible images of DDs from each instrument used for their study. As on
693 Earth, martian DDs stand out as distinctive nearly-vertical, tapered dust columns, with shadows
694 extending to the base of the dust column at the surface. With every successive mission to Mars,
695 new cameras have imaged the surface with generally increasing spatial and spectral resolution
696 (see Table 2), allowing for both DD monitoring and detailed study of DD morphology and
697 dynamics. Although a broad view from above may appear the best way to monitor DD
698 occurrence and physical characteristics, it is worth emphasizing that there are biases in orbital
699 data sets. For example, DD densities measured from orbit appear to be higher than those
700 measured from the surface. Lorenz (2013) proposed that this enhancement is caused by the
701 (typically nearly nadir) viewing angle being partly aligned with the (typically nearly vertical)
702 DDs, such that the bright dust columns are foreshortened and thus appear brighter than they
703 would from an oblique or horizontal perspective (e.g., from the ground). A further bias in
704 orbital imagery is towards larger DDs. This is caused in part by camera resolution, which
705 cannot reliably detect any features smaller than a few pixels. However, as Lorenz (2013)
706 discussed, this is exacerbated by DD longevity, which is correlated with DD size (Sinclair
707 1969).
708
709 DDs have not been observed in every location on Mars. However, the lack of detection from
710 orbit does not imply that vortices have not formed or cannot form at a given location or time.
711 Areas that lack sufficient amounts of loose dust may experience vigorous daytime convective
712 turbulence, but fail to entrain enough dust to render vortices visible in orbital images. Surface
713 lineations interpreted to be DD tracks have been identified in many locations where DDs have
714 not been directly observed (for further discussion see Chapter 4). Another factor influencing
715 DD detection is the local time of image acquisition, as DD formation is highly sensitive to the
716 thermal contrast between the ground and lower PBL (e.g., Deardorff 1978). Image data sets
717 routinely obtained during peak DD formation hours are more likely to capture them in action
718 (e.g., MOC, CTX, and HiRISE), whereas DDs are less likely to be seen in images obtained
719 either at a different routine local time or at varying local times (e.g., VO, THEMIS, and
720 HRSC).
721

3.2.1 DD inventories

There have been several global-scale surveys of martian DDs, each using image datasets of vastly different spatial resolution and temporal coverage (see Table 3). The first survey was conducted by Thomas and Gierasch (1985) using VIS images from VO during MYs 12-14, corresponding to the late 1970s on Earth (an example is shown in Figure 10a). Their study required that DDs be transient phenomena for positive detections (i.e., identified in only one of two overlapping images), to ensure they were not mistaken for landforms. Although DDs typically have a distinctive morphology, small hills can replicate their shape, and so the requirement of transience is often still in use today. Because of the limited amount of overlapping high resolution VO image coverage, Thomas and Gierasch (1985) identified only 99 DDs, found in two limited regions in the northern hemisphere lowlands (see Figure 11). Although the VO images did not fully sample the martian surface, Thomas and Gierasch (1985) did examine the entire data set, so that their survey was as "global" as the 1970s-era mission permitted. A similar but unpublished survey of DDs in VO images by Wennmacher et al. (1996) focused on these areas and the Viking Lander sites, finding more than 30 DDs, many of which were previously unidentified. An automated pattern recognition algorithm detected 313 individual DDs in the high resolution VO images of Amazonis Planitia as a first step towards applying the algorithm to HRSC images, although the rest of the VO data set has not yet been investigated (Stanzel 2007).

The advent of the MGS mission in 1997 permitted the first truly global-scale inventories and interannual monitoring surveys of geomorphic features and atmospheric phenomena, including DDs (Edgett and Malin 2000; Malin and Edgett 2001). MOC WA images typically have a lower spatial resolution than the best VO images (see Figure 10b), but their dramatically broader spatial and temporal coverage produced an unprecedented record of the martian surface and atmosphere. These images have been used to identify DDs ≥230 m in apparent height or width (here referred to as "large DDs"). In contrast, the MOC NA images sampled the surface at much higher resolution, revealing surface details to complement the context provided by MOC WA images (see Figure 10c). Although they occasionally captured "small DDs" (≥~28 m in width, ≥~170 m in height, as measured by Fisher et al. 2005), the small footprint of MOC NA images precluded sampling the likely DD population in a statistically significant way (see Table 2). DD studies using MOC images benefited from the spacecraft's nearly polar orbit, which obtained images in the early afternoon when DDs commonly form (typically 13:00-15:00), albeit at a cost of diurnal time coverage.

Fisher et al. (2005) searched MOC WA and NA images in nine broad regions on Mars (see Figure 11), greatly expanding on the Thomas and Gierasch (1985) survey. Their study areas spanned a broad range of elevation, latitude, and topographic relief, specifically targeting areas known to be sources of atmospheric dust storms (Hellas Planitia, Solis and Sinai Plana) and spacecraft landing sites (Meridiani Planum, Chryse Planitia). In MOC NA and red MOC WA images spanning ~1.25 MY from MYs 24-25 (1999-2001) in each study area, Fisher et al. (2005) tallied the number of images containing DDs into seasonal bins centered on each solstice and equinox. Depending on season and location, DDs were identified in 0% to 54% of the MOC WA images and 0% to 18% of the MOC NA images. The following year, Cantor et al. (2006) published a significantly more extensive survey of martian DDs across the entire planet, including all MOC NA and MOC WA images with spatial resolutions <500 m/px, spanning ~4.5 MY from MYs 23-27 (1997-2006). To investigate the likely seasonal dependence of DD formation rate, three monitoring sites were established in locations where DDs had frequently been observed, targeting red MOC WA images on a weekly to biweekly basis over the last ~3 MY of the survey (see Figure 11). Cantor et al. (2006) found 11,456 DDs in 0.4% of the inspected images; this work remains the most exhaustive DD imaging survey ever published. Attempts have been made at automating DD detection in MOC WA images (Gibbons et al. 2005; Yang et al. 2006), but full surveys of the image data set have yet to be completed.

The MEX mission arrived at Mars in 2003, bringing the HRSC. This camera provides stereo color images with an image footprint area on the order of that of MOC WA, but with a spatial resolution only slightly lower than that of MOC NA (see Figure 10d). These images effectively span the gap in resolution between MOC WA and MOC NA images, although they are not obtained as regularly and thus do not provide as much detail on seasonal trends in DD activity. However, MEX's orbit permits acquisition at a wider range of local times than MGS, providing more information on the diurnal pattern of DD activity. Stanzel et al. (2008) conducted a DD survey with HRSC images spanning ~1.3 MY from MYs 26-28 (2004-2006), partly overlapping in time with the MOC survey of Cantor et al. (2006). They focused on three targeted areas: Amazonis Planitia, Chryse Planitia, and Syria Planum, which were selected for their previous DD detections in orbiter and lander data. Stanzel et al. (2008) identified 205 DDs, measuring their location as well as translational velocity, diameter, and height. The average measured DD diameter and height were 230 and 660 m, respectively, indicating that

790 the previous studies using MOC WA images were unable to capture DDs smaller than the mean
791 size, highlighting the limitations of image resolution.
792
793 THEMIS obtains images of the surface in both visible and thermal IR wavelengths. This data
794 set is not optimal for a large-scale DD survey because 1) these images have a relatively low
795 spatial resolution relative to other recent data sets (although it is significantly better than that of
796 MOC WA), and 2) the sun-synchronous orbit typically passes over the surface with local times
797 later than 16:00h, when diurnal DD activity has typically waned. As a result, there are only a
798 few DD studies involving THEMIS images (Fisher et al. 2005; Cushing et al. 2005; Towner
799 2009). However, the thermal signal of a DD on either Mars or Earth is rarely measured, and
800 thus THEMIS IR images can provide valuable information regarding heat transfer between
801 DDs and the surrounding air. Towner (2009) searched THEMIS VIS images from 20ºS-50ºN
802 and from L_s=0-270º of MYs 27-28 for DDs, specifically targeting the northern hemisphere
803 summer season (see Figure 10e). They found only 8 DDs in THEMIS VIS images with
804 simultaneous THEMIS IR coverage; the small number of detections is likely a result of imaging
805 times during the late afternoon (15:42-16:30).
806
807 Recent studies of martian DDs have mainly used images from CTX, HRSC, HiRISE, and
808 CRISM, often in combination. Each of these data sets has its own advantages, reflecting
809 technological advancements over the last few decades (see Table 2). CTX images combine a
810 relatively high spatial resolution similar to that of MOC NA but with an image footprint
811 typically ~100x larger. HRSC images have a moderate spatial resolution, but they cover broad
812 swath areas and produce multiple images that can be used to track DD motion. HiRISE images
813 span only a small area, but they provide astonishing detail in color with image resolutions
814 reaching to 25 cm/px; however, they are unsuitable for broad surveys. Some DD inventories
815 have focused on specific regions, such as Arsia Mons (Reiss et al. 2009) and Amazonis Planitia
816 (Fenton and Lorenz 2015); others specifically searched through temporally-overlapping image
817 data sets to estimate DD velocities and lifetimes (Reiss et al., 2011b; 2014a). For example,
818 Reiss et al. (2014a) compiled a global inventory of DDs using CRISM VNIR images in order to
819 determine DD velocities through comparison with CTX and HiRISE images, which are
820 typically obtained with temporal offsets within ~1 minute (see Sec. 3.2.5). These detailed
821 studies step beyond simple descriptions of DD morphology and behavior, delving into DD
822 dynamics and their relation to the CBL.

3.2.2 Spatial Patterns of DD formation

To first order, DD occurrences are widespread across the surface of Mars. Cantor et al. (2006) found DDs at nearly all latitudes outside the polar regions, with detections ranging from 71.9ºS to 62.2ºN (see Figure 12). Similarly, Reiss et al. (2014a) identified DDs ranging from 68.4ºS to 68.3ºN. Martian DDs appear to form over different kinds of terrain, as well as a wide range of surface Minnaert albedos (~0.11 to ~0.22; Cantor et al. 2007 reported a global mean of ~0.18).

Despite their occurrence over a wide range of terrains, martian DDs are much more prevalent in some areas than in others. The most DD-prone region on the planet is northern Amazonis Planitia, a 2809 km diameter, low-lying basin centered on 197.09ºE, 25.75ºN. Of all surveyed DDs on Mars, Cantor et al. (2006) found that 7 out of 8 (87.5%) were located on this plain (see Figure 12). Fisher et al. (2005) found DDs in 32% of MOC WA and 12% of MOC NA images in Amazonis Planitia, whereas their other study sites averaged <1%. The high detection rate in Amazonis Planitia is likely biased because this area was an observational target for MOC WA; however, CRISM images also showed that DDs are numerous there, with 53% of all identified DDs located on this plain (Reiss et al. 2014a). It is likely a fortuitous combination of this exceptional abundance and VO high resolution image targeting that led to their initial discovery by Thomas and Gierasch (1985). In contrast, Stanzel et al. (2008) found only six Amazonis Planitia DDs in HRSC images. However, the HRSC images used in that study are not likely representative of the region: many of the images do not extend into the area most densely populated by DDs. Because of their relatively large size and frequent occurrence, DDs in Amazonis Planitia have been the target of much scrutiny (see Sec. 3.2.4).

West of the Amazonis Planitia site, there is a minor center of DD generation in Arcadia Planitia, where Cantor et al. (2006) found 0.98% of the DDs in their survey and Thomas and Gierasch (1985) identified the only two DDs in their survey that were not located in Amazonis Planitia. Otherwise, Fisher et al. (2005) and Cantor et al. (2006) found that both large and small DDs are fairly uncommon in both MOC WA and NA images in the northern hemisphere (see Figure 12). However, approximately half of the DDs identified by Stanzel et al. (2008) were located in southern Chryse Planitia, although Fisher et al. (2005) and Cantor et al. (2006) found few MOC images with DDs in this area. Stanzel et al. (2008) attributed this high DD density to the low elevation (and thus high air pressure) of Chryse Planitia, coupled with channeled air flows down Simud Vallis (an ancient outflow channel that flowed northward into Chryse Planitia). The spatial patterns of DD production zones on Mars (most notably those of

857 Amazonis and Chryse Planitiae) vary more from one spacecraft mission to another than they do
858 from interannual observations. These disparities are likely created by differences in the sampled
859 locations, local times, seasons, and imaging spatial resolutions of each mission, indicating that
860 no single instrument is perfectly suited to monitoring all degrees of DD activity over all regions
861 on Mars.
862
863 The MOC and HRSC surveys found that in the southern hemisphere, large DDs were
864 concentrated in the high-standing Solis, Syria, Thaumasia, and Sinai Plana (with elevations
865 >~3 km), as well as in Noachis Terra (located west of Hellas Planitia, with elevations ~1-2 km).
866 In contrast to the clustered production zones of the north, the MOC surveys found that small
867 southern hemisphere DDs are more widely distributed, with a slight concentration in the low-
868 lying Hellas Planitia (elevation <~-4 km). The difference in small vs. large southern DDs also
869 appears in their latitudinal distribution, in which large DDs are uncommon south of ~50ºS, but
870 smaller DDs are well-distributed down to ~70ºS. The HRSC survey found a relatively high
871 density of DDs from 50-60ºS, matching the high density of DD tracks in the same area found
872 by Whelley and Greeley (2008). Showing consistency with the MOC surveys, these HRSC
873 DDs were typical in size compared to others found elsewhere in that study (100-500 m in
874 diameter), but none were as large as the towering dust columns of the high plateaus and
875 Amazonis Planitia (i.e., few exceeded heights of 1 km). Stanzel et al. (2008) attributed this
876 southern midlatitude activity to the enhanced southern summer insolation relative to that in the
877 northern hemisphere, caused by Mars' eccentric orbit. However, it is not clear what process
878 would create large DDs in some areas but not in others.
879
880 Fisher et al. (2005) and Cantor et al. (2006) observed DDs at elevations on Mars ranging from
881 the deepest basin (<-6 km) to the highest plateaus (>7 km). However, the DD distribution with
882 elevation does not follow a simple trend: larger DDs are more prevalent at higher elevations
883 and (with the exception of Amazonis Planitia) smaller DDs are more prevalent at lower
884 elevations; this is the result of the clustering on the southern tropical Plana and in Hellas
885 Planitia discussed above. Cantor et al. (2006) attributed the abundance of small DD
886 observations at low elevation to a correspondingly higher air pressure, in which the threshold
887 conditions for particle entrainment are reduced relative to those elsewhere on Mars. Thus,
888 vortices need not be so intense to entrain dust at lower elevations, so that a higher proportion of
889 the more common, weaker vortices become visible. In turn, the large DDs at high elevation
890 could be created by a relatively deep CBL (Hinson et al., 2008; Spiga et al., 2010) accompanied

by strong updrafts (Spiga and Lewis, 2010), which could in turn produce taller DDs (Fenton and Lorenz, 2015).

There are many locations on Mars where DD production appears to be enhanced by local conditions. Cantor et al. (2006) noted that DDs are more common near the boundaries of contrasting albedo features, which are known to generate vortices in terrestrial field studies (Snow and McClelland 1990; Renno et al. 2004). In some cases, DDs cluster in groups or align in rows (Biener et al. 2002; Fisher et al. 2005; Stanzel et al. 2006; Fenton and Lorenz 2015). It is possible that some surface factor, such as a roughness element or albedo contrast, locally enhances DD production in these locations. Stanzel et al. (2006) proposed that DDs might form along an air mass boundary, similar to those that been observed on Earth (e.g., Markowski and Hannon 2006). Alternatively, Fenton and Lorenz (2015) proposed that these regularly-spaced DDs could instead denote vertices of intersecting convection cells, where DDs are most likely to form. Many such scenarios are possible.

Despite many years of continued monitoring from orbit and landed missions, there have been no simultaneous observations of DDs both from above and on the ground. Despite a dedicated imaging campaign by MGS MOC, no DDs were identified from orbit that were within the same fields of view as the MER Spirit and Opportunity cameras (Cantor et al. 2006). This result is consistent with the lack of DD detection in Opportunity images (Greeley et al. 2010). However, Greeley et al. (2006) found 533 DDs in Spirit images during the most complete monitoring season in MY 27 (2005). These DDs were typically 10-20 m in diameter, with only a few large enough to have been resolved in MOC WA images. A similar attempt was made to coordinate observations from HRSC with Spirit rover images (Stanzel 2007). However, once again, no DDs were captured from orbit, as a result of mismatching fields of view with the rover and differences in the image acquisition times. The smallest DDs imaged by HRSC were ~50 m in diameter, so that the most abundant size range observed from Spirit is still not resolved by the newer camera in orbit. This disconnect between orbital and landed surveys has made it difficult to use orbital observations of DDs to make quantitative assessments of conditions at the surface.

3.2.3 Temporal patterns of DD formation

All martian DD surveys indicate that, like their terrestrial counterparts, they most frequently form when insolation is near its seasonal and diurnal maximum. HRSC images, obtained at a range of local times, show that DDs across the martian surface form from noon through the afternoon, with peak hours between ~14:00-15:00 (Stanzel et al. 2008). DDs were rarely seen in THEMIS images, which were obtained from ~15:00-17:30, indicating that the circulations that produce these vortices typically shut down by midafternoon (Cushing et al. 2005; Fisher et al. 2005; Towner 2009). These observations are consistent with diurnal DD activity observed from the surface (e.g., Greeley et al. 2006).

On a seasonal timescale, Cantor et al. (2006) found that DD numbers reached a maximum during L_s=145-150º in the northern hemisphere and at L_s=305-310º in the southern hemisphere (i.e., local summer), although some studies have identified DDs during other seasons – even during local winter (e.g., Fisher et al. 2005; Cantor et al. 2006; Stanzel et al. 2006; Stanzel et al. 2008; Fenton and Lorenz 2015). All of the global-scale surveys found that the seasonal DD distribution is sensitive to latitude, such that terrains at higher latitudes are less likely to produce DDs during local winter. For example, Cantor et al. (2006) found no DDs within half of a season surrounding the local winter solstice poleward of 50º in either hemisphere (particularly in the north). In contrast, they found that lower latitudes have two seasonal DD peaks, centered near either solstice. In the latitudinal zone 0-30ºS, Cantor et al. (2006) found that DDs formed year-round, mainly as large DDs on the high plateaus of Solis, Syria, Thaumasia, and Sinai Plana.

Interannual variability superposed on the seasonal trend of DD activity is often linked to the occurrence of dust storms. Cantor et al. (2006) found that dust storms can influence DD production; most notably, that DDs have not been observed from orbit in the midst of dust storms. This is generally thought to be caused by a less strongly superadiabatic temperature profile near the ground, as a result of increased atmospheric heating aloft (from suspended dust absorbing solar radiation) and decreased atmospheric heating of the surface (from less solar radiation reaching the ground). However, the increase in atmospheric optical depth during dust storms also reduces image contrast, making DDs more difficult to identify: if they were present under the dust haze, they would be harder to spot. Because of these factors, DD observations are generally anti-correlated with dust events. For example, Cantor et al. (2006) noted that the

onset of summertime DDs in the southern midlatitudes (40-70º S) appears to be delayed until southern spring dust storms abate.

Despite the general anti-correlation with dust storms, the detailed interaction of DD activity with weather fronts is often more complex. DDs are often seen in front of the leading edge of dust storms, indicating that mechanical turbulence from storm fronts produces vortices that are vigorous enough to entrain dust (Cantor et al. 2006; Stanzel et al. 2008). In some cases, Cantor et al. (2006) showed that the same storm may trigger DD production in one stage of its evolution, and suppress DD activity in another stage. For example, the MY 25 (2001) global dust event during southern spring and summer (see Figure 7) may have caused a short spike in DD activity during northern autumn in Amazonis Planitia as a dust haze layer associated with the expanding storm passed overhead. However, as the same storm slowly decayed a few months later, the dust-laden atmosphere appears to have delayed the start of the southern summer DD season in Syria Planum by 40º of L_s relative to the following two years.

Loose dust on the surface (i.e., that which has been transported and then deposited in the wake of dust storms) can also modulate DD production rates by changing the surface albedo. For example, Cantor et al. (2006) investigated the passage of a series of late winter dust storms over MER Spirit in 2005 (MY 27, L_s = 170-173º). These storms produced strong winds that removed surface fines, reducing the albedo of dark surface areas by 10-14% and forming new dark surface features that contrasted with surrounding bright terrain by 12-18%. Despite a dedicated MOC WA imaging campaign to observe weather patterns in the vicinity of Spirit, Cantor et al. (2006) found that only one such image captured DDs (in MY 27, L_s = 264.7º): they were located near the margins of the newly-darkened ground a few months after the storms, during the peak of the DD season (unfortunately they were too far from Spirit to be visible from the ground).

Both planet-encircling dust storm activity and surface albedo patterns vary in degree and location from one year to the next, influencing the timing of and possibly the density of DD production. It is likely that DD activity could be predicted based on the occurrence of interannually-varying storms and their resulting albedo patterns. It is also possible that longer-term changes in the martian climate system affect DD formation rates, as well as their efficiency in lifting dust. For example, Cantor et al. (2006) predicted that the subtle change in

insolation during the 11 year solar cycle could also impact DD formation rates, although no studies have yet sought to test this hypothesis.

3.2.4 DD observations at specific locations

3.2.4.1 Northern Amazonis Planitia

Northern Amazonis Planitia is far and away the dominant producer of both large and small DDs on Mars. Figure 13 shows that there is a regularly-occurring active ("on") season that typically begins with sporadic activity just prior to the northern spring equinox and extends until just past the northern autumn equinox (Cantor et al. 2002; Fisher et al. 2005; Cantor et al. 2006, Fenton and Lorenz 2015). DDs generally do not form during the rest of the year (the "off" season), although Fenton and Lorenz (2015) reported a few isolated cases during late fall and early winter. Superposed on the seasonal pattern is a higher frequency variation in DD density on the order of 5-10º L_s, possibly related to regional weather patterns (e.g., dust storms and fronts) that might briefly enhance or suppress DD formation.

Figure 13 shows that the DD "on" seasons during Mars Years 26 (2002) and 27 (2004) in Amazonis Planitia experienced a gradual growth in activity, peaking at MOC WA densities of ~$2x10^{-3}$ DD/km^2 at L_s~140º (Fisher et al. 2005; Cantor et al. 2006). A survey of the same region using CTX images from MYs 28-31 (2006-2013) produced density peaks of ~$8x10^{-3}$ DD/km^2 (Fenton and Lorenz 2015); this relatively high density reflects the increase in spatial resolution of CTX images versus that of MOC WA images rather than any interannual variation (see Table 2). Fenton and Lorenz (2015) observed no similar growth in activity during northern spring and summer in MYs 29-31 (2007-2011), contrasting with the trend in MYs 26-27 (2002-2004). It is not yet clear whether this behavior is only apparent in MOC WA images or interannual variations have affected the DD production rate.

The most significant departures from the "on vs. off" seasonal trend in Amazonis Planitia appear in MYs 25 (2001) and 27 (2004), when DD production appears low late in summer (MOC WA densities <$1x10^{-3}$ km^2). The low DD occurrence in MY 25 occurs long before the onset of the MY 25 global dust event (just after northern autumn solstice), and therefore this lull in activity is unlikely to be related to this storm. Fisher et al. (2005) attributed the weak DD activity in MY 25 to low image exposures early in the MGS mission, making features less crisp (and thus DDs more difficult to identify). Unfortunately no MOC WA images of the area earlier during the "on" season in MY 25 are available for comparison, leaving this problem

unresolved. The early drop in DD production during the late summer of MY 27 (L_s~155º) occurred as dust haze from a global-scale dust event passed over Amazonis Planitia, following the general trend that high altitude dustiness suppresses DD production by increasing the stability of the lower CBL.

It is not immediately apparent why DD production rates in northern Amazonis Planitia are so high relative to the rest of the planet. By treating the lower atmosphere as a heat engine, the intensity of DD production can be represented as a function of the pressure thickness of the convective boundary layer (Rennó et al. 1998). When using this relation to create a parameterization of dust lifting by DD activity in martian atmospheric models (such as GCMs), Amazonis Planitia stands out as a major source of atmospheric dust (Newman et al. 2002a; Basu et al. 2004; Kahre et al. 2006). This appears to be caused by the low thermal inertia of the surface, which allows the daytime surface temperature in Amazonis Planitia to soar (e.g., Putzig et al. 2005). However, data from TES indicate that there are other regions on Mars with equally high summertime surface temperatures, similarly deep CBLs, and comparable sensible heat fluxes, but these regions do not produce correspondingly high densities of DDs (Fisher et al. 2005). It is possible that yet unidentified local and regional factors, such as dust availability or albedo/thermal inertia contrasts in the vicinity of the high DD density region, constructively interfere to enhance DD production in Amazonis Planitia.

3.2.4.2 Syria and Eastern Meridiani Plana

Being located not far south of the equator, Cantor et al. (2006)'s Syria Planum monitoring site (see Figure 11) experienced two seasonal peaks in DD production, one at each solstice. The southern winter peak is the stronger of the two, lasting from L_s=109-132º, with typical MOC WA densities exceeding $1.5x10^{-3}$ DD/km^2. The slightly weaker southern summer peak ranged from L_s=265-315º, with MOC WA densities less than $1.5x10^{-3}$ DD/km^2. It is not clear why the winter peak would be more intense than the summer peak, as the insolation during winter would be less than that during summer. Perhaps some dynamical effect from the nearby Tharsis volcanoes somehow plays a role in producing conditions conducive to DD formation. Further investigation with data from subsequent years might provide clues (or at least better statistics) to address this question.

Like its northern counterpart in Amazonis Planitia, Syria Planum experienced some interannual variability in DD activity (Cantor et al. 2006). In the two full years of monitoring in Syria

Planum during MY 26-27 (2002-2005), the second year's winter season was slightly more active, although the reason for this is not known. In both years, the winter DDs stopped abruptly after L_s~135º; in the case of MY 27 this shutdown may be related to the occurrence of a planet-encircling dust storm. The summer DD season onset in MY 25 was delayed by ~40º of L_s relative to those in MYs 26 and 27, likely as a result of the extensive MY 25 global dust event.

Cantor et al. (2006)'s monitoring site in Meridiani Planum experienced a lower rate of DD formation than the other two sites, although (perhaps because of this) it was not monitored as frequently. DDs at this nearly equatorial site were found nearly year-round, with a short southern winter break from L_s~130-190º. A slight peak in southern summer activity occurred from L_s=272.5-302.5º, with maximum MOC WA densities less than ~1.4×10^{-3} DD/km^2. An enhancement during late southern summer in MY 27 (2005) relative to that in MY 26 (2004) was attributed to local dust storm activity that may have deposited or abraded a source of dust for entrainment.

3.2.4.3 Arsia Mons

Surprisingly, DDs have been identified at elevations exceeding 16 km above the datum. Cushing et al. (2005) was the first to report the occurrence of 3 DDs in the Arsia Mons caldera in THEMIS VIS and IR images, and Cantor et al. (2006) identified 3 in MOC WA images. In a search of MOC NA, MOC WA, THEMIS VIS, HRSC, and CTX images, Reiss et al. (2009) found 28 DDs, 11 of which formed at elevations >16 km; most of these formed in the caldera. The DDs on Arsia Mons appear to form year-round, although there is a peak in activity during late local summer from L_s=340-360º. The air pressure at this altitude is ~1 mbar, six times lower than the global annual average surface air pressure, and wind stresses required to directly lift dust are 2-3 times higher than those found at the surface. Although it may seem unlikely that dust-laden vortices could form in such a sparse atmosphere (indeed, many Earth researchers might have supposed the same of any location on Mars prior to their discovery), the direct observations and many bright tracks attest to their profusion on the caldera floor.

It is not clear how DDs form and entrain dust at the top of this tall volcano, but it is notable that they have not been reported at the tops of the other, equally tall Tharsis volcanoes. Reiss et al. (2009) proposed that the illumination of a dusty surface at low air pressure enhances entrainment through a combination of a thermophoretic force and solid state greenhouse effect.

Comparing mesoscale and large eddy simulations at different elevations on Mars, Spiga and Lewis (2010) suggested that winds produced by convective activity are relatively stronger at high elevation, enhancing the likelihood of DD formation on Arsia Mons (Lorenz and Myers (2005) proposed that a similar effect on Earth may contribute to more DD-related aviation incidents at high elevation in the United States). In addition, their occurrence late in the afternoon (~15:00-16:00) in THEMIS VIS images is rare on Mars (e.g., Fisher et al. 2005; Stanzel et al. 2008), so that mechanical turbulence from some local factor (e.g., the 110 km wide, smooth caldera floor surrounded by steep cliffs ~1 km high) may be required to trigger DD generation at this altitude and local time.

In addition to DDs, Arsia Mons is also host to a 50 km wide "spiral dust storm" that regularly forms in late southern winter, shortly before the southern spring equinox (see Figure 14; Malin et al. 2010). Mesoscale model simulations by Rafkin et al. (2002) suggest that this storm is part of a larger thermally-driven circulation up the slopes of Arsia Mons that reaches ~30 km above the caldera; the dust is derived from the lower slopes of the volcano and carried aloft by daytime upslope winds that can exceed 25 m/s. Recent observations from MCS indicate that detached dust layers are common at this season over the Tharsis volcanoes, at altitudes higher (~65 km) and with mass mixing ratios higher (~150 ppm) than previously modeled (Heavens et al. 2015). This study suggests that daytime slope winds racing up the high-relief Tharsis volcanoes force the terrain to serve as a chimney, transporting dust to high altitudes. Although this mechanism is driven by mesoscale circulations, which are not a major topic of this review, it is possible that these slope winds bring the dust, and possibly the mechanical turbulence, that is responsible for DD generation in the Arsia Mons caldera.

3.2.5 Physical Characteristics of DDs

3.2.5.1 Dimensions

DD dimensions have been measured from orbital image data from several missions (Thomas and Gierasch 1985; Fisher et al. 2005; Stanzel et al. 2006; 2008; Towner 2009; Choi and Dundas 2011; Reiss et al. 2011b; 2014a; 2014b; Fenton and Lorenz 2015; see also Table 4). The diameter is usually determined by measuring the visible extent of the dust-laden columnar vortex, although in some cases the extent of the vortex shadow width was used (e.g., Fisher et al. 2005). The uncertainty in measuring DD diameter from orbital imagery depends on the spatial ground resolution of the image data. For example, Stanzel et al. (2008) observed a DD

in a HRSC nadir image with a spatial ground resolution of 25 m/px which was simultaneously imaged by the HRSC SRC camera with a spatial ground resolution of 5 m/px, obtaining diameters of 90 m versus 42 m, respectively. This suggests that errors in measuring DD diameters from orbit can be quite large (up to ~50 %) due to dust clouds surrounding the vortex, causing uncertainties in accurately determining the dust-laden vortex diameter. However, DD diameters measured with higher resolution image data are more accurate.

DD heights are calculated by measuring the shadow length and dividing it by the tangent of the solar incidence angle. There are several uncertainties for accurate measurements of shadow lengths, such as detached dust clouds and diffuse shadows. In addition, DDs are not necessarily vertical; they are typically tilted towards the direction of motion (i.e., downwind) with height (e.g., McGinnigle 1966; Maxworthy 1973). Thus, the error in measuring DD heights is estimated to be between ~20 to ~30 % (e.g., Reiss et al. 2014a; Fenton and Lorenz 2015). The accuracy in measuring heights is probably higher for relatively short DD, which exhibit sharper shadows (Fenton and Lorenz 2015). In 2012, the HiRISE team announced the tallest recorded DD, with an estimated height of 20 km (http://www.uahirise.org/ESP_026394_2160; this DD is also shown in Figure 10f and 10g). Fenton and Lorenz (2015) proposed that this height is an overestimate, produced by a combination of DD lean and shear by winds aloft, both of which would artificially stretch the dust column and make it appear taller. Imagers are not the only sensor that can estimate DD height: some DDs may have been dense enough to trigger returns in MOLA data (Neumann et al. 2003), raising the question of whether terrestrial lidars such as CALIOP have been able to detect convectively-lofted dust.

Table 4 summarizes orbital measurements of DD dimensions obtained by different instruments. DD diameters range between 10 and 1650 m and heights between 0.03 and 16.5 km. Fisher et al. (2005), Stanzel et al. (2006; 2008), Towner (2009), Choi and Dundas (2011), and Reiss et al. (2011b; 2014a; 2014b) provided detailed information about simultaneously measured DD diameters and heights. Based on this data set of about 300 measurements, average diameters and heights are 220 m and 0.63 km (median = 160 m and 0.45 km), respectively. **Error! Reference source not found.** shows a plot of measured DD dimensions, showing a general correlation of height and diameter. However, the wide scattering of the measurements also indicates that there is no clear analytical relationship between these two dimensions. This is not surprising, considering the large variety in DD morphologies (Balme and Greeley, 2006; see also Chapters 5 and 6). DD height-to-diameter ratios, based on the data shown in **Error!**

Reference source not found., range from ~0.5 to 28 with a mean of 3.8 (median = 2.5). This ratio is in broad agreement with the terrestrial and martian median height-to-diameter ratio of ~5 reported by Lorenz (2013), based on the studies by Flower (1936) and Fisher et al. (2005).

The minimum detectable DD diameter is dependent on the spatial ground resolution of each the orbital camera. At least two to three pixels are needed to resolve a DD, including any surrounding dust clouds. Thus DDs with diameters <~500 m are not identifiable in MOC WA images with spatial ground resolutions of ~230 m/px, whereas detection of DDs with diameters as small as~1m is theoretically possible in HiRISE imagery, with spatial ground resolutions of up to 0.25 m/px (although the smallest observed diameter in HiRISE to date is ~10 m). In general, orbital image data reveals larger DDs in comparison to those identified in lander observations. Greeley et al. (2010) observed ~760 DDs in images taken from MER Spirit on the martian surface, with diameters ranging between 2 and 276 m; the median diameter was 30 m, more than 5x smaller than that obtained from orbital camera images. Full DD heights from lander images could only be determined for 44 DDs (most extended beyond the top of the images), which ranged from 0.01 to 0.36 km (Greeley et al. 2006), compared to 0.03 to 16.5 km from orbital data.

DDs on Mars can be orders of magnitude larger than terrestrial ones. On Earth, in situ measurements of DD diameters and heights are typically in the range of ~1 to < 100 m and ~0.01 to < 1.2 km, respectively (Flower 1936; Williams 1948; Sinclair 1965; Snow and McClelland 1990; Mattson et al. 1993). However, Bell (1967) and Sinclair (1964) reported DDs as high as 2.5 km and 3.8 km, respectively. Although the typical size ranges of terrestrial DDs are comparable to those observed at martian landing sites, the diameters and heights obtained with orbital instruments imply that DDs on Mars can be several orders of magnitude larger. The lack of DD detections in terrestrial satellite imagery also suggests that DDs on Earth are smaller in size. This discrepancy might be caused by differences in the PBL on both planets, which limits the height extent of convective vortices. The CBL depth on Earth over land is usually below 2-3 km (e.g., Garratt, 1994), in contrast to Mars, which typically has CBL depths between 4 and 10 km (Hinson et al. 2008). Fenton and Lorenz (2015) analyzed seasonal DD height and PBL variations in Amazonis Planitia on Mars. They found that median DD heights are generally about 0.2 × PBL depth, in agreement with terrestrial studies (Willis and Deardorff 1979; Hess and Spillane 1990; Ansmann et al. 2009) comparing DD heights with that of the CBL. The difference in DD heights on Mars and Earth is likely caused by “a greater solar

energy (absorbed by the surface) to atmospheric mass ratio on Mars (tens of times greater than that on Earth), providing martian DDs with a more effective power source" (Kok et al. 2012). It is not yet clear whether DD dimensions on Earth correlate with length scales in the terrestrial PBL.

3.2.5.1 Translational ground speeds

Dynamic processes on Mars can be captured by orbital instruments or platforms acquiring time-delayed imaging data of the same surface area. Hence, the horizontal ground speed and direction of motion of DDs translating across the surface can be directly measured when imaged by such datasets. For example, Cantor et al. (2006) used two VO images taken 5 s apart from each other, which showed the same DD in the overlapping area of the two images. The DD moved ~880 m towards the northeast across the surface in the time between the two image observations, resulting in a horizontal ground speed of 17.6 ± 2.6 m s^{-1} (Cantor et al. 2006). However, such observations in acquired image pairs of frame cameras are rare, because the overlapping areas required to contain the same DD are relatively small. The unique imaging capabilities of the HRSC pushbroom instrument (Jaumann et al. 2007; Gwinner et al., submitted to Icarus) allow systematic measurements of DD translational ground speeds. The HRSC consists of nine line sensors simultaneously acquiring superimposed image swaths of the martian surface. The different emission angles (+18.9° to -18.9°) of each of the nine image channels result in a time delay at which the same surface area is covered. The maximum time delay between the outermost forward- and backward-looking image channels is about one minute. Stanzel et al. (2006; 2008) measured translational ground speeds of 205 DDs using HRSC images, with results ranging between 1 and 59 m s^{-1}, and a mean of 13 m s^{-1} (median: 10.4 m s^{-1}). Reiss et al. (2011b) measured translational ground speeds of an additional 26 DDs in HRSC images, which ranged between 3 and 22 m s^{-1}, with a mean of 12 m s^{-1} (median: 11.1 m s^{-1}) in the Syria-Claritas region on Mars.

Another method of systematically obtaining DD translational ground speeds was recently introduced by Reiss et al. (2014a) using the CRISM imaging spectrometer in combination with the CTX and/or HiRISE cameras, which are all located on the same instrument platform onboard MRO (see Table 2). The CRISM instrument uses an active pointing system for tracking targets with long exposure times (Murchie et al. 2007). The center of a surface target is imaged by forward- and backward-looking angles in the flight direction, in contrast to the exclusively nadir-looking angles of the CTX and HiRISE instruments, resulting in positive and

negative time offsets of ~±1 minute between the CRISM and CTX/HiRISE surface observations. Using this method, Reiss et al. (2014a) measured translational ground speeds of 44 DDs, which ranged from 4 - 25 m s^{-1} with a mean of 12 m s^{-1} (median: ~11.5 m s^{-1}). A further method measuring DD translational ground speeds is the usage of the HiRISE blue-green, red, and infrared color swaths, which cover the same surface area with a time delay of ~0.1 seconds. However, such measured horizontal ground speeds should be seen as an estimate due to the very short time interval between the color swaths, which introduces significant uncertainties. Choi and Dundas (2011) and Reiss et al. (2014b) estimated DD translational ground speeds in the range of ~5-20 m s^{-1} using HiRISE color swaths.

The comparison of some DD translational ground speeds and directions of motion with predicted wind speeds and directions from the Mars Climate Database (MCD; Forget et al. 1999) indicated that DDs move with speeds and in directions of the ambient wind field (Stanzel et al. 2006; 2008). A systematic study comparing measured DD translational ground speeds and directions of motion with MCD-predicted wind speeds and directions at various heights by Reiss et al. (2014a) showed that DDs on Mars move with ambient wind fields and with ground speeds commensurate with those at height within the PBL, hence faster than near-surface winds. This is in agreement with terrestrial in situ studies by Balme et al. (2012), who compared measured DD translational ground speeds and directions of motion with wind and direction measurements at 10 m height. They found that DDs move at speeds and in directions reflecting the ambient wind field within the PBL at about 20-30 m above the surface (Balme et al. 2012). As pointed out by Balme et al. (2012) and shown by Reiss et al. (2014a), orbital measurements of DD translational ground speeds and directions of motion can therefore be used as a proxy for local regional wind regimes within the PBL on Mars.

Table 5 summarizes horizontal ground speed measurements from both orbiting and landed missions on Mars. Greeley et al. (2010) measured horizontal ground speeds of nearly 500 DDs at the MER Spirit landing site in Gusev crater based on time sequential lander images. Although the range of translational ground speeds of the large dataset obtained by Greeley et al. (2010) is in agreement with orbitally-derived ranges of DD translational ground speeds, the median speeds are lower than those measured from orbit. Because orbital data can only resolve larger DDs, in contrast to lander missions, this might suggest that larger DDs move faster. However, neither the orbital nor landing site nor even terrestrial data sets have found a relationship between translational ground speeds and DD diameter (Stanzel et al. 2008; Greeley

et al. 2010; Balme et al. 2012; Reiss et al. 2014a). This implies that the differences between the globally-derived orbiter and locally-obtained lander results are reflecting differences in global and local wind regimes on Mars.

3.2.5.2 Tangential velocities

The threshold friction velocity required to directly entrain surface dust into the thin martian atmosphere is estimated to be ~30 m s^{-1} (Greeley and Iversen 1985). Thus measurements of tangential velocities provide a first order estimate of the intensity of DDs and their capacity to lift dust from the martian surface, although many other mechanisms are suggested to lower the threshold friction velocity for dust lifting by DDs on Mars and Earth (see Chapters 10 and 11). Measurements of tangential velocities from orbit are rare, because multiple satellite images taken of the same DD within a short time period are needed. In addition, contrast features in the DD cloud must be visible for measuring the displacement between the image observations. Cantor et al. (2006) measured a tangential velocity of 14.1 ± 0.3 m s^{-1} in the outermost visible part of a DD, with a diameter of ~370 m and a height of ~900 m, from two VO images taken 5 seconds apart. Choi and Dundas (2011) used the blue-green, red, and infrared central color swaths of the HiRISE camera, taken 0.1 seconds apart, to automatically track contrast features in four DDs with diameters between ~25 and 250 m and heights between ~150 and 650 m. Their wind vector measurements yielded typical tangential velocities approaching ~20 and 30 m s^{-1}, with maximum velocities reaching ~45 m s^{-1}. The strongest tangential velocities in all DDs occurred along the outer edge of the visible dust columns (Choi and Dundas 2011).

Terrestrial in situ measurements by Sinclair (1973) and laboratory studies by Greeley et al. (2003) of DD velocities are in good agreement with a Rankine vortex model, in which the core exhibits solid body rotation and tangential velocities linearly increase with radius *r*, reaching a peak outside the radius, and then decreasing as a function of r^{-1}. A radial profile of one DD measured by Choi and Dundas (2011) was in good agreement with the Rankine vortex model, but another one decreased as a function of $r^{-1/2}$ instead of r^{-1} outside the solidly rotating central region (Choi and Dundas 2011). A velocity profile closer to the $r^{-1/2}$ distribution was also measured in situ on Earth by Tratt et al. (2003) and attributed to nonconservation of angular momentum caused by frictional losses near the surface (Tratt et al. 2003; Balme and Greeley 2006). For further discussion of vortex models used to describe DDs, we refer the reader to Chapter 6.

Table 6 summarizes tangential velocity measurements of DDs by orbital instruments on Mars, by in situ measurements on Earth, and by modeling approaches based on in situ measurements for Mars. The tangential velocities of DDs on Mars measured from orbit by Choi and Dundas (2011) are about two to three times higher than terrestrial peak tangential velocities measured in situ by Ryan and Carroll (1970), Fitzjarrald (1973), Sinclair (1973), Metzger (1999), Tratt et al. (2003), and Metzger et al. (2011). One reason for this discrepancy might be that the martian orbital measurements are from large and relatively intense DDs (>50 m in diameter), whereas terrestrial measurements mainly sample smaller DDs (<10 m in diameter). The largest data set provided by Ryan and Carrol (1970) indicated that larger DDs are more intense, exhibiting greater tangential velocities (Balme and Greeley, 2006). The disparity between orbital measurements of martian DD tangential velocities and those measured *in situ* on Earth is yet another example of the disconnect in understanding between orbital and surface observations of DDs.

Tangential velocities are related to the pressure drop across the vortex by assuming cyclostrophic balance (Rennó et al. 1998). For further details we refer the reader to Renno et al. (1998) and Chapters 6 and 10. Tratt et al. (2003) applied this method to two terrestrial DDs passing directly over the instruments and observed a good agreement between measured and calculated tangential velocities. Theoretically-calculated minimum tangential velocities for DDs on Mars by Rennó et al. (2000) using meteorological data (pressure and temperature pertubations) from the Mars Pathfinder landing site ranged between 8.6 and 17.7 m s^{-1}. These predicted minimum values for convective vortices are uncertain because it is unclear if the DDs passed directly over the lander instruments.

Ringrose et al. (2003) analyzed meteorological data from VL2 and found that seven convective vortices passed directly over the instruments. They calculated tangential velocities ranging between 2.8 and 46 m s^{-1} for inferred core diameters between ~22 and ~313 m, using the Rankine vortex approximation. Their derived peak velocity of 46 m s^{-1} is in agreement with peak velocities derived from orbital measurements by Choi and Dundas (2011).

3.2.5.3 DD duration

Terrestrial observations and duration measurements of DDs imply that larger DDs are active longer than smaller ones (Flower 1936; Ives 1947; Sinclair 1969; Snow and McClelland 1990; Metzger 1999; Pathare et al. 2010). On Mars, Stanzel et al. (2008) and Reiss et al. (2011b)

constrained minimum DD durations with orbital data sets. Stanzel et al. (2008) measured translational ground speeds of 12 DDs in HRSC images and divided the length of their adjacent tracks (for a detailed review about DD tracks we refer the reader to Chapter 4) by their speed. The derived durations are minimum values, because the DDs used as the end point were still active during observation and likely continued. In addition, the starting point of the DD tracks are uncertain because their formation depends on surface substrate properties (see Chapter 4), hence the observed DDs might have been active before the track formation started. The calculated minimum durations by Stanzel et al. (2008) range between 3.7 and 32.5 minutes with a mean value of 13 minutes for DDs characterized by a mean diameter of about 185 m. Reiss et al. (2011b) observed DDs in HRSC data, some of which some could be retraced to DDs in a MOC WA image acquired 26 minutes earlier, using the measured translational ground speeds and directions of motion from the HRSC image data. Two DDs with mean diameters of ~700 m had a minimum lifetime of 26 minutes. The inferred minimum duration for one DD with a diameter of ~820 m is 74 minutes based on its adjacent track length and translational ground speed. Greeley et al. (2006; 2010) derived mean minimum durations of ~2.5 minutes for DDs with a mean diameter of ~30 m at the MER Spirit landing site in Gusev crater on Mars. Table 7 summarizes minimum and mean durations of DDs on Mars. There is a diameter-duration relationship for DDs on Mars in which larger DDs last longer than smaller ones; a similar relationship has been determined from *in situ* measurements on both Mars and Earth (Lorenz 2013), although the underlying reasons for it have yet to be determined.

3.2.6 Relation of DDs to regional/global circulation

The significance of the role of DDs in the martian climatic system has long been debated. Entrained dust affects both the thermal structure and the circulation of the atmosphere (e.g., Kahn et al. 1992). Therefore, if DDs loft a sufficient quantity of dust, they could contribute significantly to the seasonal and interannual dust cycles that dominate Mars' climate system. Years ago, it was postulated that DDs could trigger dust storms (Kahn et al. 1992), but orbital observations of DDs and dust storms clearly show that this is not the case (e.g., Balme et al. 2003; Cantor et al. 2006; Stanzel et al. 2008). Rather, DDs appear to be responsible for producing a global background haze (with optical depths in the visible of ~0.1-0.3) that persists year-round, even during northern spring when dust storm occurrence is at a minimum (e.g., Clancy et al. 2000). Evidence for this is inferred from dust flux estimates from both lander and orbiter observations of DD activity (Ryan and Lucich 1983; Murphy and Nelli 2002; Balme et al. 2003; Ferri et al. 2003; Fisher et al. 2005; Balme and Greeley 2006; Cantor et al. 2006;

Whelley and Greeley 2008; Reiss et al. 2011b). Regional to global-scale dust storms entrain much of the dust that contributes to the measured AOT, but it is clear that they do not account for all of it; DDs have been considered a major source of the remaining component (Guzewich et al. 2015). In addition, recent aerosol measurements indicate the presence of a fine particle population with a mean radius of ~50 nm (Federova et al. 2014). Without a continuous source from the surface, these aerosols would quickly coagulate; Federova et al. (2014) attributed their production to continuous lofting from both wind stress and DDs. Finally, many studies using GCM simulations agree that DDs are required to maintain the observed low-level background dust loading during the aphelion season, when dust storms are not prevalent and thus cannot be a reliable source of entrained dust (Newman et al. 2002a; Basu et al. 2004; Kahre et al. 2006).

A major question in martian science is to understand how long-term changes in dust loading affect the climate. Mars has undergone dramatic changes in orbital variations in the past 10 Ma, with the eccentricity ranging from 0 to 0.115 (currently at a relatively high value of 0.0935), obliquity ranging between 15º-45º (currently at a moderate value of 25.19º), and continual precession of the aerocentric longitude of perihelion (perihelion currently occurs at L_s=251º, nearly coinciding with southern summer solstice at L_s=270º); each of these orbital parameters oscillates with periods ranging from ~50 ka – 2.4 Ma (Laskar et al. 2004). Atmospheric modeling under different orbital states has provided some insight on how DD activity impacts erosion and deposition of dust on the surface. At a high obliquity (45º), DDs are predicted to be more active than they are today, but they would loft far less dust than that entrained by saltation impact driven by high wind stresses; conversely, at low obliquity (<15º), DDs may be the dominant source of atmospheric dust (Newman et al. 2005). In the current perihelion state, dust lifting is thought to be caused both by DDs and saltation impact; however, DDs are predicted to dominate dust entrainment in the opposing perihelion position, which last occurred 22.5 ka (Haberle et al. 2006).

Predictions of dust erosion and deposition rates by both wind stress and DDs can be used to place constraints on the age of dust deposits on the martian surface, connecting climate cycles to geological processes on the surface. Vast swaths of dust-covered terrain in the low and mid northern latitudes of Mars, often termed the “low thermal inertia continents”, are regions of net dust deposition (this includes Amazonis Planitia). Estimating that they could be as much as 2 m thick, Christensen (1986) proposed that these regions are currently accumulating new deposits, but that in opposing perihelion states, these deposits would erode, perhaps as a result of DD

activity, and reform elsewhere. Haberle et al. (2006) tested this hypothesis with GCM simulations, comparing the present day to that at 22.5 and 72.5 ka, when Mars was at the opposite longitude of perihelion. They found that over the last ~100 ka, DDs have caused net erosion of these deposits. Newman et al. (2005) looked at longer timescales when the obliquity was higher, finding that some of the dusty areas undergo accumulation at high obliquity (>35º), and that as a result these deposits may have formed ~>500 ka. However, their model results predict regions of net deposition that only partially correspond with the pattern of observed dust deposits, indicating that other processes that have not yet been considered must also impact the evolution of dust reservoirs on Mars. The full impact of DDs on dust erosion, transport, and deposition is not yet understood, but atmospheric modeling suggests that these processes can play a significant role in altering both the climate and surface geology on Mars; the reader is referred to Chapter 11 for further discussion.

4. Conclusions

4.1 High-level comparison of atmospheric dust on Earth and Mars

Although data sets and methods differ, it is possible to perform a semi-quantitative comparison of global mean dust measurements on Earth and Mars, placing these estimates in a planetary context. Table 8 lists the global mean AOT and DOT, dust emission rate, and the percentage estimated to be contributed by convective turbulence (e.g., by DDs).

Global mean AOT values (at a wavelength of 550 nm) for Earth have been measured by a number of sensors and simulated with at least one aerosol model, with estimates ranging from 0.118 to 0.188. However, there are not yet any estimates of the global mean DOT from orbital data sets. Chin et al. (2009) used GOCART to estimate that mineral dust consisted of ~30% of the AOT, with a 550 nm DOT of 0.042, second in magnitude only to sulfate aerosols. The AeroCom project simulated the Earth's atmospheric dust budget with a median model that uses monthly output from twelve aerosol models. Global DOT estimates from these models ranged from 0.01 to 0.053, with a median model estimate at 0.023.

A similar estimate can be made for Mars, using the climatology of Montabone et al. (2015). The 9.3 μm equivalent column DOTs were converted to broadband visible DOTs by multiplying by a factor of 2.0, which is consistent with that expected for 1.5-2.0 μm dust

particles (e.g., Lemmon et al. 2015). Further, full-extinction DOTs were estimated from absorption-only values by multiplying by an additional suggested factor of 1.3. The resulting area-weighted and annually-averaged DOTs for each of seven MYs are listed in Table 8, as is the mean DOT for all seven years (0.43). Also listed is the mean DOT excluding MYs 25 and 28 (0.39), which experienced global-scale dust events (see Figure 7, and note that the global mean DOT for MY 25 is twice that of MY 30). Although the martian DOTs are broadband equivalent values and the terrestrial DOTs were estimated at 550 nm, the low Angstrom coefficient values found for mineral dust imply that the terrestrial broadband AOT and DOT values are similar to those estimated at 550 nm, allowing for approximate comparisons of the two planetary atmospheres. The global mean martian optical depths are ~2.5-3 times that of terrestrial aerosols, and ~15-20 times that contributed by dust on Earth. Mars is, indeed, a dusty planet.

As stated in Sec. 2.1.1, annual mineral dust emission rates on Earth range from 1000-4000 Tg/EY (Boucher et al. 2013). To estimate a comparable mean flux of dust into the Martian atmosphere, we consider several observations. Optical depth is proportional to the column number density, area, and extinction efficiency. Column mass (*CM*) is proportional to column number density, volume, and particle density. Thus column mass may be expressed as $CM = (AOT/Q) \times (V/A) \times \rho$; where we estimate the particle volume to area ratio, *V/A*, to be 4/3 x 1.5×10^{-6} m (Lemmon et al. 2004). This estimate assumes the *CM* is close to that for mono-disperse spheres; the extinction efficiency, *Q*, is 2-4; and the particle density, ρ, is 2.5 g cm^{-3}. Thus for the 7 MY mean DOT, we find a column mass of 0.5-1.1×10^{-6} g m^{-2} and an atmospheric aerosol mass of 80-150 Tg. During the aftermath of the 1971, 1977a, 1977b, and 2007 global dust storms, when lifting was inhibited, the sedimentation timescale was 42-67 sols (Pollack et al. 1979; Fenton et al. 1997; Lemmon et al. 2015). Thus the characteristic supply (and sedimentation) rate must be ~1-4 Tg sol^{-1}, or ~400-1300 Tg per Earth year. Years without global-scale dust events have a slightly lower mean emission rate of ~400-1200 Tg yr^{-1}; the dustiest year with an available annual mean DOT is MY 25, which had a dust emission rate of ~600-2000 Tg yr^{-1}. The martian dust emission estimate is comparable, if on the low end, to that of Earth. Given that the continental surface area of Earth is close to the global surface area of Mars, this result suggests that the mean dust lifting rate per unit area is similar on both planets. This result is somewhat surprising, given the quite variable nature of dust emission in space and time on both Earth and Mars (e.g., little dust lifting is expected over terrestrial rain forests or on the martian polar caps). For comparison, meteoric input of dust to the Martian atmosphere is

relatively insignificant, at 0.002-0.003 Tg yr^{-1} (Flynn 1992), similar to that estimated for Earth, 0.0018-0.1 Tg yr^{-1} (Plane 2012).

Jemmett-Smith et al. (2015) estimated that only ~3.4% of the mineral dust emission rate is caused by convective turbulence. Without better measurements from the surface, it is difficult to make a similarly precise estimate for Mars. Atmospheric models that include parameterizations of dust flux from convective turbulence suggest that daytime convective activity contributes to as much as 30-50% of the global martian dust budget (Newman et al. 2002b; Kahre et al. 2006). A second approach makes use of the global-scale DD inventory of Cantor et al. (2006), who estimated a global dust flux >$4x10^{-3}$ kg m^{-2} MY^{-1}, which amounts to >600 Tg/MY (or >300 Tg yr^{-1}). Given the range of dust emission rates in a year without a global-scale dust event, DDs would contribute to >25-75% of the estimated dust flux, a percentage similar to that predicted by the atmospheric models.

From these rough estimates, we may conclude that, although mean dust emission rates are similar on Earth and Mars, Mars' dust budget is more dependent on small-scale convective turbulence, whereas Earth's dust budget is generated mainly by frontal storms. Such storms occur on Mars as well (e.g. Wang and Richardson 2015), but the current understanding suggests that, unlike on Earth, dust lofting by convective activity is comparable in magnitude to these storms on Mars.

4.2 Summary and knowledge gaps

This review demonstrates the breadth of work being done with orbiting spacecraft data to understand lofted dust, particularly that entrained by daytime convective turbulence (most notably by DDs), on both Earth and Mars. In the past two decades, the availability of several high quality, high resolution spacecraft instruments orbiting Earth has led to an improved understanding of the nature of entrained mineral dust. This includes not just dust sources, transport pathways, and sinks, but also characteristics of aerosol particle size, shape, composition, and optical properties. With this knowledge base, connections are being made between mineral dust patterns and weather patterns, both on daily and interannual time scales. The same is true of Mars, but to a much more limited extent, with progress being constrained by the type and extent of the available data sets. Despite this impediment, ongoing work into convectively-lofted dust on Mars is in many ways more advanced than that on Earth.

It is clear that on both Earth and Mars, mineral dust aerosols play a significant and yet largely unconstrained role in modulating the climate, by acting as an internal forcing mechanism in the climate system. Atmospheric dust appears to play a relatively more significant role on Mars, where dust is plentiful, sinks are more limited (i.e., there are no oceans), and there are fewer processes competing with dust (e.g., clouds and precipitation are limited). Similarly, convectively-lofted dust is much more prominent on Mars, where the thin atmosphere and typical daytime superadiabatic conditions produce vigorous turbulent activity that encourages the formation of dusty plumes and DDs.

Several years of monitoring dust and DD activity on Mars has led to a general understanding about the spatial and temporal patterns of dust lifting. DDs are widespread phenomena on Mars, reaching to nearly all latitudes and elevations. Like those on Earth, they occur most often when insolation is at its seasonal and diurnal peak. This correlation is modulated by weather patterns, most notably those that generate dust storms, which can either suppress or enhance DD production. In addition, local factors such as albedo contrast on the surface, nearby topographic relief, and changes in dust source availability also appear to influence DD formation. It is likely that remote monitoring of DD occurrence and density would be of value in studying similar processes on Earth.

Physical characteristics of martian DDs observed from orbit differ from those measured from landed missions, which are in some ways similar to many of the field surveys performed on Earth. From orbit, DDs are generally wider, taller, translate along the ground faster, and rotate faster than those measured from the surface. To some degree, these differences are a factor of image resolution: for example, only the largest DDs are visible from orbit, whereas measurements of much smaller and more plentiful DDs dominate the data sets from the surface (see also Fig. 9). Despite this measurement bias, some true physical variations are clear. Examples include the towering DDs of Amazonis Planitia, which are not common in most other locations on Mars, and the fact that many DD translational ground speeds are much higher than those measured on Earth. The failure to obtain simultaneous observations of individual DDs from orbit and the surface, despite valiant attempts to do so, leaves a gap in understanding the differences between the observed DD characteristics. Given that DD dimensions and translational speeds could be indicative of conditions within the PBL, it may be of value to resolve the discrepancy between orbital and surface measurements, both for Mars and Earth

atmospheric studies. This could be accomplished through coordinated orbital and surface observations on both Earth and Mars, or with LES that resolve individual DDs, thus allowing virtual viewing both from above and from the ground.

Despite decades of studying martian DDs, many questions remain: why are DDs so numerous and large in Amazonis Planitia, and less so at other similarly low-lying plains with comparable albedos, thermal inertias, and latitudes? why do DDs form at elevation on Arsia Mons, but not at the tops of other high-standing volcanoes on Mars? how do DDs contribute to surface erosion and the deposition of long-term dust reservoirs on the surface? how can DDs be used to characterize the present-day atmosphere of Mars, and how does interannual variation in DD activity interact with and reflect other interannual changes (e.g., albedo and thermal inertia patterns, annual H_2O and CO_2 cycles)? what locally-dependent factors control DD size and production rates? Further research on the expanding data sets will surely address many of these questions, as will continued attempts to model DD behavior under increasingly realistic conditions. Similar questions could be posed for Earth, using the available literature on Mars as a starting point. The first question to address is why terrestrial DDs have not yet been observed from orbit. We suggest that the numerous high resolution cameras, and perhaps lidars as well, continually monitoring the Earth's surface are an untapped resource for DD studies, both for comparative planetology with Mars and to better understand aerosol entrainment mechanisms on Earth.

In summary, dust entrained by daytime convective turbulence, particularly that of DDs, appears to impact (at least) local atmospheric conditions on Earth and the global climate on Mars. Much has been learned about atmospheric dust from orbital sensor data over the last few decades, but varying methods, data sets, and scientific goals have led to different insights on Earth and Mars. Future investigations on each planet have the potential to inform further research on the other planet. For example, scouring the extensive terrestrial image data sets for DDs, as has been done for Mars, could prove to be quite fruitful. Likewise, observations and validated simulations of terrestrial DDs from both the surface and from above could resolve the current discrepancy between landed and orbital spacecraft observations of martian DDs. Studies on both planets indicate that DDs are an integral part of the dust cycle, which likely varies in relative importance with temporal and spatial changes in climate. We propose that further progress can be accelerated when the terrestrial and planetary communities work together to determine how convectively-lofted dust impacts planetary atmospheres.

Acknowledgements

The authors would like to thank two anonymous reviewers and an editor for many suggestions that greatly improved the manuscript.

Figure Captions

Figure 1. Early spacecraft images of dust storms. a) An early image of dust over the Arabian Sea and Gulf of Oman; the view is towards the southwest, with Iran and Pakistan on the right and the Arabian Peninsula on the left. Image from Schnapf (1964). b) In 1971, Mariner 9 entered orbit around Mars during an intense, global dust storm, that obscured all surface features except for four tall volcano peaks (labeled A through D) and the south polar cap (white spot at lower right). Image from Masursky et al. (1972).

Figure 2. Visible MODIS images of dust plumes over a) the Yellow Sea and b) downwind of North Africa. Adapted from Marticorena and Formenti (2013).

Figure 3. Mean Aerosol Optical Depth (AOD, which is used interchangeably with AOT) from June 2000 through May 2010 from MISR. (NASA map by Robert Simmon, based on MISR data.)

Figure 4. Seasonal distribution of AOT (blue) and DOD (yellow to red) measured from MODIS Deep Blue aerosol products, from Ginoux et al. (2012). AOT is sensitive to all particulates, whereas DOD is derived from AOT and considered representative of mineral dust from natural sources.

Figure 5. Characteristic evolution of dust storms (from Wang and Richardson 2015) showing 60ºS to 60ºN in a cylindrical projection for L_s=214-228º in MY 27 (2005). Numbers indicate the relative sol.

Figure 6. Routes for storm sequences as described (modified from Wang and Richardson 2015). Black indicates storms of northern origin; green indicates those of southern origin; dashed lines indicate polar storms. Numbers indicate how many storms were observed in each trajectory segment.

Figure 7. Climatology of column dust optical depth (CDOD) at 9.3 μm spanning MYs 24-31 (April 1999 – July 2013), from Montabone et al. (2015).

Figure 8. Visible optical depth from the model assimilation at six intervals during the MY 23 (1997) Noachis dust storm, normalized to 610 Pa to remove topographic effects (from Lewis et al. 2007). The plots are in polar stereographic projection with the south pole at the center, the equator at the edge, and with the prime meridian pointing upward.

Figure 9. The minimum detected dust devil diameter on Mars from different orbital image surveys, showing a trend towards smaller dust devils with increased sensor resolution.

Figure 10. Examples of DDs imaged by cameras orbiting Mars. a) VO2 image 038B25, b) MOC WA image E23/01275, with box showing the location of the concurrent c) MOC NA image E23/01274, d) HRSC image H2054_0000_ND3, e) THEMIS VIS image V02326010, f) CTX image G21_026394_2155, with a box showing the location of the concurrent g) HiRISE image ESP_026394_2160 (both color and red images are shown).

Figure 11. A MOLA shaded relief map of Mars with colorized elevation, showing locations referred to in this work. DD monitoring sites for three global-scale surveys are noted. Note that Cantor et al. (2006)'s study included nearly the entire planet and that the regions indicated here are those with dedicated image targeting for DD activity.

Figure 12. Locations of MOC WA and NA images with DDs identified in the Cantor et al. (2006) survey, superposed on a composite of TES surface albedo and MOLA shaded relief. Note the high density of DDs in Amazonis Planitia, their widespread distribution in the southern midlatitudes, and the different spatial patterns of DDs detected by the two different cameras.

Figure 13. Multiple years of DD densities measured in Amazonis Planitia from a) MOC WA images, modified from Cantor et al. (2006) and b) CTX images, modified from Fenton and Lorenz (2015). Colored bars correspond to the duration of global-scale dust events.

Figure 14. A seasonally-repeating spiral cloud 50 km wide on the caldera floor of Arsia Mons, ~16.3 km above the datum.

Figure 15. DD diameter vs. height, based on measurements from orbital imagers described in the literature (see Table 4). Black lines show height-to-diameter ratios of 1, 5, and 20. Minimum detectable DD diameter depends on, among other factors, image resolution (see also Figure 9 and Table 4).

Table Captions

Table 1. Instruments on spacecraft orbiting Earth, discussed in the text, that are or were commonly used to study atmospheric dust.

Table 2. Instruments on spacecraft orbiting Mars, discussed in the text, that are or were commonly used to study atmospheric dust.

Table 3. Global-scale DD surveys on Mars.

Table 4. The range of DD diameters and heights measured from various orbital platforms on Mars, including the number of DDs measured (*N*).

Table 5. Translational speeds of martian DDs, including the number of DDs considered (*N*), the observed range, mean and median values.

Table 6. Tangential velocities of DDs on Mars and Earth, including the number of DDs considered (*N*), the mean velocity (V_{mean}), and the maximum velocity (V_{max}).

Table 7. DD durations on Mars, including the number of DDs measured (*N*), mean and minimum duration, and mean DD diameter.

Table 8. Comparison of dust loading measurements on Earth and Mars

References

A. Ansmann, M. Tesche, P. Knippertz, E. Bierwirth, D. Althausen, D. Müller, O. Schulz, Vertical profiling of convective dust plumes in southern Morocco during SAMUM, Tellus B. **61**, 340–353 (2009) doi: 10.1111/j.1600-0889.2008.00384.x

M.R. Balme, P.L Whelley, R. Greeley Mars: Dust devil track survey in Argyre Planitia and Hellas Basin, J Geophys Res **108**:5086 (2003) doi:10.1029/2003JE002096

M. Balme, R. Greeley, Dust devils on Earth and Mars, Rev. Geophys. **44**, RG3003 (2006) doi:10.1029/2005RG000188

M.R. Balme, A. Pathare, S.M. Metzger, M.C. Towner, S.R. Lewis, A. Spiga, L. Fenton, N.O. Renno, H. M. Elliott, F.A. Saca, T. Michaels, P. Russell, J. Verdasca, Field measurements of horizontal forward motion velocities of terrestrial dust devils: Towards a proxy for ambient winds on Mars and Earth, Icarus **221**, 632–645 (2012) doi:10.1016/j.Icarus2012.08.021

J.R. Banks, H.E. Brindley Evaluation of MSG-SEVIRI mineral dust retrieval products over North Africa and the Middle East, Remote Sens. Environ. **128**, 58–73 (2013) doi:10.1016/j.rse.2012.07.017

S. Basu, M.I. Richardson, R.J. Wilson, Simulation of the Martian dust cycle with the GFDL Mars GCM, J. Geophys. Res. **109**, E11006 (2004) doi:10.1029/2004JE002243.

S. Basu, J. Wilson, M.I. Richardson, A. Ingersoll, Simulation of spontaneous and variable global dust storms with the GFDL Mars GCM, J. Geophys. Res.-Planets **111** (2006) doi:10.1029/2005je002660

F. Bell, Dust devils and aviation, Meteorol. Note 27, Commonwealth of Australia, Bureau of Meteorology, pp. 10 (1967)

J.F. Bell, M.J. Wolff, M.C. Malin, W.M. Calvin, B.A. Cantor, M.A. Caplinger, R.T. Clancy, K.S. Edgett, L.J. Edwards, J. Fahle, F. Ghaemi, R.M. Haberle, A. Hale, P.B. James, S.W. Lee, T. McConnochie, E. Noe Dobrea, M.A. Ravine, D. Schaeffer, K.D. Supulver, P.C. Thomas, Mars Reconnaissance Orbiter Mars Color Imager (MARCI): Instrument description, calibration, and performance, J. Geophys. Res. **114** (2009) doi:10.1029/2008JE003315

S. Berthier, P. Chazette, P. Couvert, J. Pelon, F. Dulac, F. Thieuleux, C. Moulin, T. Pain, Desert dust aerosol columnar properties over ocean and continental Africa from Lidar In-Space Technology Experiment (LITE) and Meteosat synergy, J Geophys Res **111**, D21202 (2006) doi:10.1029/2005JD006999

K.K. Biener, P.E. Geissler, A.S. McEwen, C. Leovy, Observations of Martian Dust Devils in MOC Wide Angle Camera Images, in Lunar Planet. Sci. Conf. XXXIII, League City, TX, Abst. #2004 (2002)

O. Boucher, D. Randall, P. Artaxo P, C. Bretherton, G. Feingold, P. Forster, V.-M. Kerminen, Y. Kondo, H. Liao, U. Lohmann, P. Rasch, S.K. Satheesh, S. Sherwood, B. Stevens, X.Y.Zhang, in Climate Change 2013: The Physical Science Basis, ed. By T.F. Stocker, D. Qin, G.-K. Plattner, M. Tignor, S.K. Allen, J. Boschung, A. Nauels, Y. Xia, V. Bex, P.M. Midgley (Cambridge University Press, United Kingdom and New York, NY, USA, 2013) p. 571 doi:10.1017/CBO9781107415324.016

G.A. Briggs, W. A. Baum, J. Barnes, Viking Orbiter imaging observations of dust in the Martian atmosphere, J. Geophys. Res. **84**, 2795–2820 (1979) doi: 10.1029/JB084iB06p02795

B.A. Cantor, P.B. James, M. Caplinger, M.J. Wolff, Martian dust storms: 1999 Mars Orbiter Camera observations, J. Geophys. Res. **106**, 23,653 (2001) doi:10.1029/2000JE001310

B. Cantor, M. Malin, K.S. Edgett, Multiyear Mars Orbiter Camera (MOC) observations of repeated Martian weather phenomena during the northern summer season, J. Geophys. Res. **107**(E3), 5014 (2002) doi:10.1029/2001JE001588

B.A. Cantor, K.M. Kanak, K.S. Edgett, Mars Orbiter Camera observations of Martian dust devils and their tracks (September 1997 to January 2006) and evaluation of theoretical vortex models, J. Geophys. Res. **111**, E12002 (2006) doi:10.1029/2006JE002700

B.A. Cantor, MOC observations of the 2001 Mars planet-encircling dust storm, Icarus **186**(1), 60–96 (2007) doi:10.1016/j.icarus.2006.08.019

D. Carrer, X. Ceamanos, B. Six, J.-L. Roujean, AERUS-GEO: A newly available satellite-derived aerosol optical depth product over Europe and Africa, Geophys. Res. Lett. **41**, 7731–7738 (2014) doi:10.1002/2014GL061707

1688 I. Chiapello, C. Moulin, J.M. Prospero, Understanding the long-term variability of African dust transport
1689 across the Atlantic as recorded in both Barbados surface concentrations and large-scale TOMS
1690 optical thickness, J. Geophys. Res. **110**, D18S10 (2005) doi:10.1029/2004JD005132
1691 I. Chiapello, Dust observations and climatology, in: Mineral Dust: A Key Player in the Earth System,
1692 ed. By P. Knippertz, J.-B.W. Stuut (Springer, Dordrecht, 2014) p. 149 doi:10.1007/978-94-017-
1693 8978-3.
1694 M. Chin, T. Diehl, Q. Tan, J.M. Prospero, R.A. Kahn, L.A. Remer, H. Yu, A.M. Sayer, H. Bian, I.V.
1695 Geogdzhayev, B.N. Holben, S.G. Howell, B.J. Huebert, N.C. Hsu, D. Kim, T.L. Kucsera, R.C.
1696 Levy M.I. Mishchenko, X. Pan, P.K. Quinn, G.L. Schuster, D.G. Streets, S.A. Strode, O. Torres,
1697 X.-P. Zhao Multi-decadal aerosol variations from 1980 to 2009: a perspective from observations
1698 and a global model, Atmos. Chem. Phys. **14**, 3657–3690 (2014) doi:10.5194/acp-14-3657-2014
1699 D.S. Choi, C.M. Dundas, Measurements of martian dust devil winds with HiRISE, Geophys. Res. Lett.
1700 **38** (2011) doi:10.1029/2011GL049806.
1701 P.R. Christensen, Regional dust deposits on Mars: Physical properties, age, and history, J. Geophys.
1702 Res., **91**(B3), 3533–3545 (1986) doi:10.1029/JB091iB03p03533
1703 P.R. Christensen, Global albedo variations on Mars - Implications for active aeolian transport,
1704 deposition, and erosion, J. Geophys. Res. **93**(B7), 7611–7624 (1988)
1705 doi:10.1029/JB093iB07p07611
1706 P.R. Christensen, B.M. Jakosky, H.H. Kieffer, M.C. Malin, H.Y. McSween Jr., K. Nealson, G.L.
1707 Mehall, S.H. Silverman, S. Ferry, M. Caplinger, M. Ravine, The Thermal Emission Imaging
1708 System (THEMIS) for the Mars 2001 Odyssey Mission, Space Sci. Rev. **110**, 85 (2004)
1709 doi:10.1007/978-0-306-48600-5_3
1710 R.T. Clancy, B.J. Sandor, M.J. Wolff, P.R. Christensen, M.D. Smith, J.C. Pearl, B.J. Conrath, R.J.
1711 Wilson, An intercomparison of ground-based millimeter, MGS TES, and Viking atmospheric
1712 temperature measurements: Seasonal and interannual variability of temperatures and dust loading
1713 in the global Mars atmosphere. J Geophys Res **105**:9553–9571 (2000) doi: 10.1029/1999JE001089
1714 D.S. Colburn, J.B. Pollack, R.M. Haberle, Diurnal variations in optical depth at Mars, Icarus **79**, 159–
1715 189 (1989) doi:10.1016/0019-1035(89)90114-0.
1716 S.M. Cowie, P. Knippertz, J.H. Marsham, Are vegetation-related roughness changes the cause of the
1717 recent decrease in dust emission from the Sahel? Geophys. Res. Lett. **40**, 1868–1872 (2013)
1718 doi:10.1002/grl.50273
1719 G.E. Cushing, T.N. Titus, P.R. Christensen, THEMIS VIS and IR observations of a high-altitude
1720 Martian dust devil, Geophys. Res. Lett. **32**:23 (2005) doi:10.1029/2005GL024478
1721 J.W. Deardorff, Observed characteristics of the outer layer. in Short Course on the Planetary Boundary
1722 Layer, ed. By A.K. Blackadar (Am. Meteorol. Soc., Boston, Mass., 1978) 101pp.
1723 K.S. Edgett, M.C. Malin, Martian dust raising and surface albedo controls: Thin, dark (and sometimes
1724 bright) streaks and dust devils in MGS MOC high resolution images, in Lunar Planet. Sci. Conf.
1725 XXXI, Houston, TX, Abst. #1073 (2000)
1726 M.D. Ellehøj, H.P. Gunnlaugsson, P.A. Taylor, H. Kahanpää, K.M. Bean, B.A. Cantor, B.T. Gheynani,
1727 L. Drube, D. Fisher, A.-M. Harri, C. Holstein-Rathlou, M.T. Lemmon, M.B. Madsen, M.C. Malin,
1728 J. Polkko, P.H. Smith, L.K. Tamppari, W. Weng, J. Whiteway, Convective vortices and dust devils
1729 at the Phoenix Mars mission landing site, J. Geophys. Res. **115** (2010) doi:10.1029/2009JE003413
1730 A.T. Evan, J. Dunion, J.A. Foley, A.K. Heidinger, C.S. Velden, New evidence for a relationship
1731 between Atlantic tropical cyclone activity and African dust outbreaks, Geophys. Res. Lett. **33**,
1732 L19813, (2006) doi:10.1029/2006GL026408
1733 A.T. Evan, S. Mukhopadhyay, African dust over the northern tropical Atlantic: 1955–2008, J. Appl.
1734 Meteorol. Climatol. **49**, 2213–2229 (2010) doi:10.1175/2010JAMC2485.1
1735 A.T. Evan, C. Flamant, S. Fiedler, O. Doherty, An analysis of aeolian dust in climate models. Geophys.
1736 Res. Lett. **41**, 5996–6001 (2014) doi:10.1002/2014GL060545
1737 A.A. Fedorova, F. Montmessin, A. Rodin A, O.I. Korablev, A. Määttänen, L. Maltagliati, J.-L. Bertaux,
1738 Evidence for a bimodal size distribution for the suspended aerosol particles on Mars, Icarus **231**,
1739 239–260 (2014) doi: 10.1016/j.icarus.2013.12.015
1740 L.K. Fenton, J.C. Pearl, T.Z. Martin, Mapping Mariner 9 Dust Opacities, Icarus **130**, 115–124 (1997)
1741 doi:10.1006/icar.1997.5810
1742 L.K. Fenton, R. Lorenz, Dust devil height and spacing with relation to the martian planetary boundary
1743 layer thickness, Icarus **260**, 246–262 (2015) doi:10.1016/j.icarus2015.07.028

F. Ferri, P.H. Smith, M. Lemmon, N.O. Rennó, Dust devils as observed by Mars Pathfinder, J Geophys Res. **108** (2003) doi:10.1029/2000JE001421
J.A. Fisher, M.I. Richardson, C.E. Newman, M.A. Szwast, C. Graf, S. Basu, S.P. Ewald, A.D. Toigo, R.J. Wilson, A survey of Martian dust devil activity using Mars Global Surveyor Mars Orbiter Camera images, J. Geophys. Res. **110**, E03004 (2005) doi:10.1029/2003JE002165
D.E. Fitzjarrald, A field investigation of dust devils, J. Appl. Meteor. **12**, 808–813 (1973) doi:10.1175/1520-0450(1973)012<0808:AFIODD>2.0.CO;2
W.D. Flower, Sand devils. London Meteorol. Off. Prof. Notes. **5**, No. 71 (1936)
G.J. Flynn, The meteoritic contribution to dust and aerosols in the atmosphere of Mars, in Workshop on the Martian Surface and Atmosphere through Time, Boulder, CO, USA, Report No. NASA-CR-190418, 51-52 (1992)
G.R. Foltz, M.J. McPhaden, Trends in Saharan dust and tropical Atlantic climate during 1980–2006, Geophys Res Lett **35**, L20706 (2008) doi:10.1029/2008GL035042
F. Forget, F. Hourdin, R. Fournier, C. Hourdin, O. Talagrand, M. Collins, S.R. Lewis, P.L. Read, J.-P. Huot, Improved general circulation models of the martian atmosphere from the surface to above 80 km, J. Geophys. Res. **104**:E10, 24,155–24,175 (1999) doi:10.1029/1999JE001025
J.R. Garratt, The Atmospheric Boundary Layer (Cambridge Univ. Press, New York, 1994)
S. Gassó, A.F. Stein, Does dust from Patagonia reach the sub-Antarctic Atlantic Ocean? Geophys Res Lett **34**, L01801 (2007) doi:10.1029/2006GL027693
P.E. Geissler, Three decades of Martian surface changes, J. Geophys. Res. **110**:E02001 (2005) doi:10.1029/2004JE002345
A. Gibbons, F. Yang, P. Mlsna, P. Geissler, Automated procedures for detecting martian dust devils, in Lunar Planet. Sci. Con. XXXVI, League City, TX, Abst. #2005 (2005)
P.J. Gierasch, R.M. Goody, A model of a Martian Great dust storm, J. Atmos. Sci. **30**:2, 169–179 (1973) doi:10.1175/1520-0469(1973)030<0169:AMOAMG>2.0.CO;2
D.A. Gillette, P.C. Sinclair, Estimation of suspension of alkaline material by dust in the United States, Atmos. Environ. **24A**:5, 1135–1142 (1990) doi:10.1016/0960-1686(90)90078-2
P. Ginoux, J.M. Prospero, T.E. Gill, N.C. Hsu, M. Zhao Global-scale attribution of anthropogenic and natural dust sources and their emission rates based on MODIS Deep Blue aerosol products, Rev. Geophys. **50**:RG3005 (2012) doi:10.1029/2012RG000388
A. Goudie, N. Middleton, Desert Dust in the Global System (Springer, Berlin, 2006)
D. Grassi, V. Formisano, F. Forget, C. Fiorenza, N.I. Ignatiev, A. Maturilli, L.V. Zasova, The martian atmosphere in the region of Hellas basin as observed by the planetary Fourier spectrometer (PFS-MEX), Planet. Space Sci. **55**, 1346–1357 (2007) doi:10.1016/j.pss.2006.12.006
R. Greeley, J. Iversen, Wind as Geologic Process on Earth, Mars, Venus, and Titan (Cambridge Univ. Press, New York, 1985)
R. Greeley, M.R. Balme, J.D. Iversen, S.M. Metzger, R. Mickelson, J. Phoreman, B. White, Martian dust devils: Laboratory simulations of particle threshold. J. Geophys. Res. **108** (2003) doi:10.1029/2002JE001987
R. Greeley, P.L. Whelley, R.E. Arvidson, N.A. Cabrol, D.J. Foley, B.J. Franklin, P.G. Geissler, M.P. Golombek, R.O. Kuzmin, G.A. Landis, M.T. Lemmon, L.D.V. Neakrase, S.W. Squyres, S.D. Thompson, Active dust devils in Gusev crater, Mars: Observations from the Mars Exploration Rover Spirit, J. Geophys. Res. **111**:E12S09 (2006) doi:10.1029/2006JE002743
R. Greeley, D.A. Waller, N.A. Cabrol, G.A. Landis, M.T. Lemmon, L.D.V. Neakrase, M. Pendeleton Hoffer, S. D. Thompson, P. L. Whelley, Gusev crater, Mars: Observations of three dust devil seasons, J. Geophys. Res. **115**:E00F02 (2010) doi:10.1029/2010JE003608
S.D. Guzewich, A.D. Toigo, L. Kulowski, H. Wang, Mars Orbiter Camera climatology of textured dust storms, Icarus **258**, 1-13 (2015) doi:10.1016/j.icarus.2015.06.023
K. Gwinner et al., The High Resolution Stereo Camera (HRSC) of Mars Express and its approach to science analysis and mapping for Mars and its satellites. Planet. Space Sci., in revision.
R.M. Haberle, C.B. Leovy, J.B. Pollock, Some effects of global dust storms on the atmospheric circulation of Mars, Icarus **50**, 322–367 (1982) doi:10.1016/0019-1035(82)90129-4
R.M. Haberle, M.A. Kahre, J.R. Murphy, Role of dust devils and orbital precession in closing the Martian dust cycle, Geophys. Res. Lett. **33** (2006) doi:10.1029/2006GL026188
R. Hanel, B. Conrath, W. Hovis, V. Kunde, P. Lowman, W. Maguire, J. Pearl, J. Pirraglia, C. Prabhakara, B. Schlachman, G. Levin, P. Straat, T. Burke, Investigation of the Martian

environment by infrared spectroscopy on Mariner 9, Icarus **17**, 423–442 (1972) doi:10.1016/0019-1035(72)90009-7
N.G. Heavens, J.L. Benson, D.M. Kass, A. Kleinbohl, W.A. Abdou, D.J. McCleese, M.I. Richardson, J.T. Schofield, J.H. Shirley, P.M. Wolkenberg, Water ice clouds over the Martian tropics during northern summer, Geophys. Res. Lett. **37** (2010) doi:10.1029/2010gl044610
N.G. Heavens, D.J. McCleese, M.I. Richardson, D.M. Kass, A. Kleinböhl, J.T. Schofield, Structure and dynamics of the Martian lower and middle atmosphere as observed by the Mars Climate Sounder: 2. Implications of the thermal structure and aerosol distributions for the mean meridional circulation, J. Geophys. Res. Planets **116**:E01010 (2011a) doi:10.1029/2010JE003713
N.G. Heavens, M.I. Richardson, A. Kleinbohl, D.M. Kass, D.J. McCleese, W. Abdou, J.L. Benson, J.T. Schofield, J.H. Shirley, P.M. Wolkenberg, Vertical distribution of dust in the Martian atmosphere during northern spring and summer: High-altitude tropical dust maximum at northern summer solstice, J. Geophys. Res. Planets **116** (2011b) doi:10.1029/2010JE003692
N.G. Heavens, B.A. Cantor, P.O. Hayne, D.M. Kass, A. Kleinböhl, D.J. McCleese, S. Piqueux, J.T. Schofield, J.H. Shirley, Extreme detached dust layers near Martian volcanoes: Evidence for dust transport by mesoscale circulations forced by high topography, Geophys. Res. Lett. **42**, 3730–3738, (2015) doi:10.1002/2015GL064004J.R. Herman, P.K. Bhartia, O. Torres O, C. Hsu, C. Seftor, E. Celarier, Global distribution of UV-absorbing aerosols from Nimbus 7/TOMS data, J. Geophys. Res. **102**, 16,911 (1997) doi: 10.1029/96JD03680.
M. Herman, J.-L. Deuzé, A. Marchand, B. Roger, P. Lallart, Aerosol remote sensing from POLDER/ADEOS over the ocean: Improved retrieval using a nonspherical particle model, J. Geophys. Res. **110**:D10S02 (2005) doi:10.1029/2004JD004798
G.D. Hess, K.T. Spillane, Characteristics of dust devils in Australia, J. Appl. Meteorol. **29**, 498–506 (1990) doi:10.1175/1520-0450(1990)029<0498:CODDIA>2.0.CO;2
S.L. Hess, R.M. Henry, C.B. Leovy, J.A. Ryan, J.E. Tillman, Meteorological results from the surface of Mars: Viking 1 and 2, J. Geophys. Res. **82**, 4559–4574 (1977) doi:10.1029/JS082i028p04559
R. Hesse, Short-lived and long-lived dust devil tracks in the coastal desert of southern Peru, Aeolian Res. **5**, 101–106 (2012) doi:10.1016/j.aeolia.2011.10.003
D.P. Hinson, M. Pätzold, S. Tellmann, B. Häusler, G.L. Tyler, The depth of the convective boundary layer on Mars, Icarus **198**, 57–66 (2008) doi: 10.1016/j.icarus.2008.07.003
D.P. Hinson, H. Wang, Further observations of regional dust storms and baroclinic eddies in the northern hemisphere of Mars, Icarus **206**, 290–305 (2010) doi:10.1016/j.icarus.2009.08.019
D.P. Hinson, H. Wang, M.D. Smith, A multi-year survey of dynamics near the surface in the northern hemisphere of Mars: Short-period baroclinic waves and dust storms, Icarus **219**, 307–320 (2012) doi:10.1016/j.icarus.2012.03.001
D.P. Hinson, S.W. Asmar, D.S. Kahan, V. Akopian, R.M. Haberle, A. Spiga, J.T. Schofield, A. Kleinböhl, W.A. Abdou, S.R. Lewis, M. Paik, S.G. Maalouf, S.G. Initial results from radio occultation measurements with the Mars Reconnaissance Orbiter: A nocturnal mixed layer in the tropics and comparisons with polar profiles from the Mars Climate Sounder, Icarus **243**, 91–103. (2014) doi:10.1016/j.icarus.2014.09.019
N.C. Hsu, S.C. Tsay, M.D. King, J.R. Herman Aerosol properties over bright-reflecting source regions, IEEE Trans. Geosci. Remote Sens. **42**:3, 557–569 (2004) doi:10.1109/TGRS.2004.824067
N.C. Hsu NC, S.-C. Tsay, M.D. King, J.R. Herman, Deep Blue retrievals of Asian aerosol properties during ACE-Asia, IEEE Trans. Geosci. Remote Sens. **44**:11, 3180–3195 (2006) doi:10.1109/TGRS.2006.879540
N.C. Hsu, R. Gautam, A.M. Sayer, C. Bettenhausen, C. Li, M.J. Jeong. S.-C. Tsay, B.N. Holben, Global and regional trends of aerosol optical depth over land and ocean using SeaWiFS measurements from 1997 to 2010, Atmos. Chem. Phys. **12**, 8037–8053 (2012) doi:10.5194/acp-12-8037-2012
N.C. Hsu, M.-J. Jeong, C. Bettenhausen, A.M. Sayer, R. Hansell, C.S. Seftor, J. Huang, and S.-C. Tsay, Enhanced Deep Blue aerosol retrieval algorithm: The second generation, J. Geophys. Res. Atmos. **118**, 9296–9315 (2013) doi:10.1002/jgrd.50712
J. Huang, C. Zhang, J.M. Prospero, African dust outbreaks: a satellite perspective of temporal and spatial variability over the tropical Atlantic Ocean, J. Geophys. Res. **115**:D05202 (2010) doi:10.1029/2009JD012516
N. Huneeus, M. Schulz, Y. Balkanski, J. Griesfeller, J.A. Prospero, S. Kinne, S. Bauer, O. Boucher, M. Chin, F. Dentener, T. Diehl, R. Easter, D. Fillmore, S. Ghan, P. Ginoux, A. Grini, L. Horowitz, D.

Koch, M. Krol, W. Landing, X. Liu, N. Mahowald, R. Miller, J.-J. Morcrette, G. Myhre, J.E. Penner, J. Perlwitz, P. Stier, T. Takemura, and C. Zender, Global dust model intercomparison in AeroCom phase I, Atmos. Chem. Phys. **11**, 7781–7816 (2011) doi:10.5194/acp-11-7781-2011

G.E. Hunt, P.B. James, Martian extratropical cyclones. Nature **278**, 531–532 (1979) doi:10.1038/278531a0

R.B. Husar, J.M. Prospero, L.L. Stowe, Characterization of tropospheric aerosols over the oceans with the NOAA AVHRR optical thickness product, J. Geophys. Res. **102**, 16,889–16,909 (1997) doi:10.1029/96JD04009

R.L. Ives, Behavior of dust devils. Bull. Am. Meteorol. Soc. **28**, 168–174 (1947)

I. Jankowiak, D. Tanré, Satellite climatology of Saharan dust outbreaks: method and preliminary results, J. Clim. **5**:6, 646–656 (1992) doi: 10.1175/1520-0442(1992)005<0646:SCOSDO>2.0.CO;2

R. Jaumann, G. Neukum, T. Behnke, T. C. Duxbury, K. Eichentopf, J. Flohrer, S. van Gasselt, B. Giese, K. Gwinner, E. Hauber, H. Hoffmann, A. Hoffmeister, U. Köhler, K.-D. Matz, T. B. McCord, V. Mertens, J. Oberst, R. Pischel, D. Reiss, E. Ress, T. Roatsch, P. Saiger, F. Scholten, G. Schwarz, K. Stephan, M. Wählisch, the HRSC Co-Investigator Team, The high-resolution stereo camera (HRSC) experiment on Mars Express: Instrument aspects and experiment conduct from interplanetary cruise through the nominal mission, Planet. Space Sci. **55**, 928–952 (2007) doi:10.1016/j.pss.2006.12.003

B.C. Jemmett-Smith, J.H. Marsham, P. Knippertz, C.A. Gilkeson, Quantifying global dust devil occurrence from meteorological analyses, Geophys. Res. Lett. **42**,1275–1282 (2015) doi: 10.1002/2015GL063078.

R.A. Kahn, T.Z. Martin, R.W. Zurek, S.W. Lee, The Martian dust cycle, in Mars, ed. By H.H. Kieffer, B.M. Jakosky, C.W. Snyder, M.S. Matthews (Univ. of Ariz. Press, Tucson, Arizona,USA, 1992), p. 1017-1053

M.A. Kahre, J.R. Murphy, R.M. Haberle, Modeling the Martian dust cycle and surface dust reservoirs with the NASA Ames general circulation model, J. Geophys. Res. **111** (2006) doi: 10.1029/2005JE002588

K.M. Kanak, D.K. Lilly, J.T. Snow, The formation of vertical vortices in the convective boundary layer, Q. J. R. Meteorol. Soc., **126**, 2789–2810 (2000) doi:10.1002/qj.49712656910

Y.J. Kaufman, I. Koren, L.A. Remer, D. Tanré, P. Ginoux, S. Fan, Dust transport and deposition observed from the Terra-Moderate Resolution Imaging Spectrometer (MODIS) spacecraft over the Atlantic Ocean, J. Geophys Res **110**:D10S12 (2005) doi:10.1029/2003JD004436

H.H. Kieffer, B.M. Jakosky, C.W. Snyder, The planet Mars: from antiquity to the present, in Mars, ed. by H.H. Kieffer, B.M. Jakosky, C.W. Snyder, M.S. Matthews (The University of Arizona Press, Tucson, AZ, 1992) p. 12-13

A. Kleinböhl,, J.T. Schofield, D.M. Kass, W.A. Abdou, C.R. Backus, B. Sen, J.H. Shirley, W.G. Lawson, M.I. Richardson, F.W. Taylor, N.A. Teanby, D.J. McCleese, Mars Climate Sounder limb profile retrieval of atmospheric temperature, pressure, and dust and water ice opacity, J. Geophys. Res. **114**:E10006 (2009) doi:10.1029/2009JE003358

J. Koch, N.O. Renno, The role of convective plumes and vortices on the global aerosol budget, Geophys. Res. Lett., **32**:18, L18806, (2005) doi:10.1029/2005GL02342J.F. Kok, E.J.R. Parteli, T.I. Michaels, D.B. Karam, The physics of wind-blown sand and dust, Reports Prog. Phys. **75**:10 (2012) doi:10.1088/0034-4885/75/10/106901

O. Korablev, V.A. Krasnopolsky, A.V. Rodin, E. Chassefière, Vertical Structure of Martian Dust Measured by Solar Infrared Occultations from the Phobos Spacecraft, Icarus **102**, 76–87 (1993) doi:10.1006/icar.1993.1033

J. Laskar, A.C.M. Correia, M. Gastineau, F. Joutel, B. Levrard, P. Robutel, Long term evolution and chaotic diffusion of the insolation quantities of Mars, Icarus **170**, 343–364 (2004) doi:10.1016/j.icarus.2004.04.005

M. Legrand, C. N'doumé, I. Jankowiak, Satellite-derived climatology of the Saharan aerosol. in: Proc. SPIE 2309, Passive Infrared Remote Sensing of Clouds and the Atmosphere II, 127–135 (1994) doi:10.1117/12.196669

M. Legrand, A. Plana-Fattori, C. N'doumé C, Satellite detection of dust using the IR imagery of Meteosat: 1. Infrared difference dust index, J. Geophys. Res. **106**, 18,251–18,274 (2001) doi: 10.1029/2000JD900749

M.T. Lemmon, M.J. Wolff, M.D. Smith, R.T. Clancy, D. Banfield, G.A. Landis, A. Ghosh, P.H. Smith, N. Spanovich, B. Whitney, P. Whelley, R. Greeley, S. Thompson, J.F. Bell, S.W. Squyres, Atmospheric imaging results from the Mars exploration rovers: Spirit and Opportunity, Science **306**, 1753–1756 (2004) doi:10.1126/science.1104474

M.T. Lemmon, M.J. Wolff, J.F. Bell, M.D. Smith, B.A. Cantor, P.H. Smith, Dust aerosol, clouds, and the atmospheric optical depth record over 5 Mars years of the Mars Exploration Rover mission, Icarus **251**, 96–111 (2015) doi:10.1016/j.icarus.2014.03.029

J. Lenoble, L. Remer, D. Tanré, (2013) Aerosol Remote Sensing (Springer, Heidelberg, 2013) doi:10.1007/978-3-642-17725-5.

C.B. Leovy, R.W. Zurek, J.B. Pollack, Mechanisms for Mars dust storms, J. Atmos. Sci. **30**:5, 749–762, (1973) doi:10.1175/1520-0469(1973)030<0749:MFMDS>2.0.CO;2

R.C. Levy, S. Mattoo, L.A. Munchak, L.A. Remer, A.M. Sayer, F. Patadia, N.C. Hsu, The Collection 6 MODIS aerosol products over land and ocean, Atmos. Meas. Tech. **6**, 2989–3034, (2013) doi:10.5194/amt-6-2989-2013

S.R. Lewis, P.L. Read, B.J. Conrath, J.C. Pearl, M.D. Smith, Assimilation of thermal emission spectrometer atmospheric data during the Mars Global Surveyor aerobraking period, Icarus **192**, 327–347 (2007) doi:10.1016/j.icarus.2007.08.009

R. Lorenz, On the statistical distribution of dust devil diameters, Icarus **215**, 381-390 (2011) doi: 10.1016/j.icarus.2011.06.005

R. Lorenz, The longevity and aspect ratio of dust devils: Effects on detection efficiencies and comparison of landed and orbital imaging at Mars, Icarus **226**, 964–970 (2013) doi:10.1016/j.icarus.2013.06.031

R.D. Lorenz, M.J. Myers, Dust devil hazard to aviation: A review of United States air accident reports, J. Meteorol., **30**:298, 179–184 (2005)

A. Määttänen, T. Fouchet, O. Forni, F. Forget, H. Savijärvi, B. Gondet, R. Melchiorri, Y. Langevin, V. Formisano, M. Giuranna, J.-P. Bibring, A study of the properties of a local dust storm with Mars Express OMEGA and PFS data, Icarus **201**, 504–516 (2009) doi:10.1016/j.icarus.2009.01.024

A. Määttänen, C. Listowski, F. Montmessin, L. Maltagliati, A. Reberac, L. Joly, J.-L. Bertaux, A complete climatology of the aerosol vertical distribution on Mars from MEx/SPICAM UV solar occultations, Icarus **223**, 892–941 (2013) doi:10.1016/j.icarus.2012.12.001

J.-B. Madeleine, F. Forget, E. Millour, T. Navarro, A. Spiga, The influence of radiatively active water ice clouds on the Martian climate, Geophys. Res. Lett. **39**:L23202 (2012a) doi:10.1029/2012GL053564

J.-B. Madeleine, F. Forget, A. Spiga, M.J. Wolff, F. Montmessin, M. Vincendon, D. Jouglet, B. Gondet, J.-P. Bibring, Y. Langevin, B. Schmitt, Aphelion water-ice cloud mapping and property retrieval using the OMEGA imaging spectrometer onboard Mars Express, J. Geophys. Res. Planets **117**:E00J07 (2012b) doi:10.1029/2011JE003940

B.A. Maher, J.M. Prospero, D. Mackie, D. Gaiero, P.P. Hesse, Y. Balkanski, Global connections between aeolian dust, climate and ocean biogeochemistry at the present day and at the last glacial maximum, Earth Sci. Rev. **99**, 61–97 (2010) doi:10.1016/j.earscirev.2009.12.001

M.C. Malin, K.S. Edgett, Mars Global Surveyor Mars Orbiter Camera: Interplanetary cruise through primary mission, J. Geophys. Res. **106**(E10), 23,429–23,570 (2001) doi:10.1029/2000JE001455

M.C. Malin, K.S. Edgett, B.A. Cantor, M.A. Caplinger, G.E. Danielson, E.H. Jensen, M.A. Ravine, J.L. Sandoval, K.D. Supulver, An overview of the 1985-2006 Mars Orbiter Camera science investigation, Mars **5** (2010) doi:10.1555/mars.2010.0001

P. Markowski, C. Hannon, Multiple-doppler radar observations of the evolution of vorticity extrema in a convective boundary layer, Mon. Weather Rev. **134**, 355–374 (2006) doi:10.1175/MWR3060.1

B. Marticorena, B. Chatenet, J.L. Rajot, Temporal variability of mineral dust concentrations over West Africa: analyses of a pluriannual monitoring from the AMMA Sahelian Dust Transect, Atmos. Chem. Phys. **10**, 8899–8915 (2010) doi:10.5194/acp-10-8899-2010

B. Marticorena, P. Formenti, Fundamentals of aeolian sediment transport: Long-range transport of dust, in Treatise Geomorphol. Vol. 11, ed. By J. Shroder, N. Lancaster, D.J.Sherman, A.C.W. Bass, (Academic Press, San Diego, CA, USA, 2013) pp. 64-84

L.J. Martin, R.W. Zurek, An analysis of the history of dust activity on Mars, J. Geophys. Res. **98**, 3221 (1993) doi:10.1029/92JE02937

T.Z. Martin, Thermal infrared opacity of the Mars atmosphere, Icarus **66**, 2–21 (1986) doi:10.1016/0019-1035(86)90003-5

T.Z. Martin, M.I. Richardson, New dust opacity mapping from Viking Infrared Thermal Mapper Data, J. Geophys. Res. **98**, 10,941–10,949 (1993) doi:10.1029/93JE01044

J.V. Martonchik, D.J. Diner, R. Kahn, B. Gaitley, B.N. Holben Comparison of MISR and AERONET aerosol optical depths over desert sites, Geophys. Res. Lett. **31**, L16102 (2004) doi:10.1029/2004GL019807

H. Masursky, R.M. Batson, J.F. McCauley, L.A. Soderblom, R.L. Wildey, M.H. Carr, D.J. Milton, D.E. Wilhelms, B.A. Smith, T.B. Kirby, J.C. Robinson, C.B. Leovy, G.A. Briggs, T.C. Duxbury, C.H. Acton Jr., B.C. Murray, J.A. Cutts, R.P. Sharp, S. Smith, R.B. Leighton, C. Sagan, J. Veverka, M. Noland, J. Lederberg, E. Levinthal, J.B. Pollack, J.T. Moore Jr., W.K. Hartmann, E.N. Shipley, G. de Vaucouleurs, M.E. Davies, Mariner 9 television reconnaissance of Mars and its satellites: Preliminary results, Science **175,** 294–305 (1972) doi:10.1126/science.175.4019.294

J.O. Mattsson, T. Nihlén, W. Yue, Observations of dust devils in a semi-arid district of southern Tunisia. Weather. **48**, 359–363 (1993) doi:10.1002/j.1477-8696.1993.tb05814.x

T. Maxworthy, A vorticity source for large-scale dust devils and other comments on naturally occurring columnar vortices, J. Atmos. Sci. **30**, 1717–1722 (1973) doi:10.1175/1520-0469(1973)030<1717:AVSFLS>2.0.CO;2

D.J. McCleese, N.G. Heavens, J.T. Schofield, W.A. Abdou, J.L. Bandfield, S.B. Calcutt, P.G.J. Irwin, D.M. Kass, A. Kleinböhl, S.R. Lewis, D.A. Paige, P.L. Read, M.I. Richardson, J.H. Shirley, F.W. Taylor, N. Teanby, R.W. Zurek, Structure and dynamics of the Martian lower and middle atmosphere as observed by the Mars Climate Sounder: Seasonal variations in zonal mean temperature, dust, and water ice aerosols, J. Geophys. Res. Planets **115** (2010) doi:10.1029/2010JE003677

A.S. McEwen, M.E. Banks, N. Baugh, K. Becker, A. Boyd, J.W. Bergstrom, R.A. Beyer, E. Bortolini, N.T. Bridges, S. Byrne, B. Castalia, F.C. Chuang, L.S. Crumpler, I. Daubar, A.K. Davatzes, D.G. Deardorff, A. DeJong, W.A. Delamere, E. Noe Dobrea, C.M. Dundas, E.M. Eliason, Y. Espinoza, A. Fennema, K.E. Fishbaugh, T. Forrester, P.E. Geissler, J.A. Grant, J.L. Griffes, J.P. Grotzinger, V.C. Gulick, C.J. Hansen, K.E. Herkenhoff, R. Heyd, W.L. Jaeger, D. Jones, B. Kanefsky, L. Keszthelyi, R. King, R.L. Kirk, E.J. Kolb, J. Lasco, A. Lefort, R. Leis, K.W. Lewis, S. Martinez-Alonso, S. Mattson, G. McArthur, M.T. Mellon, J.M. Metz, M.P. Milazzo, R.E. Milliken, T. Motazedian, C.H. Okubo, A. Ortiz, A.J. Philippoff, J. Plassmann, A. Polit, P.S. Russell, C. Schaller, M.L. Searls, T. Spriggs, S.W. Squyres, S. Tarr, N. Thomas, B.J. Thomson, L.L. Tornabene, C. Van Houten, C. Verba, C. Weitz, J.J. Wray, The High Resolution Imaging Science Experiment (HiRISE) during MRO's Primary Science Phase (PSP), Icarus **205**, 2–37 (2010) doi:10.1016/j.icarus.2009.04.023

J.B. McGinnigle, Dust whirls in north-west Libya, Weather **21**, 272–276 (1966) doi:10.1002/j.1477-8696.1966.tb05204.x

S.M. Metzger, Dust devils as aeolian transport mechanisms in southern Nevada and in the Mars Pathfinder landing site, PhD thesis, Univ. Nevada, Reno, 208 pp. (1999)

S.M. Metzger, M.R. Balme, M.C. Towner, B.J. Bos, T.J. Ringrose, M.R. Patel, In situ measurements of particle load and transport in dust devils, Icarus **214**, 766–772 (2011) doi:10.1016/j.icarus.2011.03.013

L. Montabone, F. Forget, E. Millour, R.J. Wilson, S.R. Lewis, B. Cantor, D. Kass, A. Kleinböhl, M.T., Lemmon, M.D. Smith, M.J. Wolff, Eight-year climatology of dust optical depth on Mars, Icarus **251**, 65–95 (2015) doi:10.1016/j.icarus.2014.12.034

L. Montabone, S.R. Lewis, P.L. Read, Interannual variability of Martian dust storms in assimilation of several years of Mars global surveyor observations, Adv. Space Res. **36**, 2146–2155 (2005) doi:10.1016/j.asr.2005.07.047

F. Montmessin, F. Forget, P. Rannou, M. Cabane, R.M. Haberle, Origin and role of water ice clouds in the Martian water cycle as inferred from a general circulation model, J. Geophys. Res. Planets **109**:E10004 (2004) doi:10.1029/2004JE002284

C. Moulin, I. Chiapello, Evidence of the control of summer atmospheric transport of African dust over the Atlantic by Sahel sources from TOMS satellites (1979–2000), Geophys. Res. Lett. **31**:L02107 (2004) doi:10.1029/2003GL018931

2021 D.R. Muhs, S.R. Cattle, O. Crouvi, D.-D. Rousseau, J. Sun, M.A. Zárate, Loess records, in Mineral
2022 Dust: A Key Player in the Earth System, ed. by P. Knippertz, J.-B.W. Stuut (Springer, Dordrecht,
2023 2014) p. 411 doi:10.1007/978-94-017-8978-3D.P. Mulholland, P.L. Read, S.R. Lewis, Simulating
2024 the interannual variability of major dust storms on Mars using variable lifting thresholds, Icarus
2025 **223**, 344–358 (2013) doi:10.1016/j.icarus.2012.12.003
2026 D.P. Mulholland, A. Spiga, C. Listowski, P.L. Read, An assessment of the impact of local processes on
2027 dust lifting in martian climate models, Icarus **252**, 212–227 (2015)
2028 doi:10.1016/j.icarus.2015.01.017
2029 S. Murchie et al., R. Arvidson, P. Bedini, K. Beisser, J.-P. Bibring, J. Bishop, J. Boldt, P. Cavender, T.
2030 Choo, R.T. Clancy, E.H. Darlington, D. Des Marais, R. Espiritu, D. Fort, R. Green, E. Guinness, J.
2031 Hayes, C. Hash, K. Heffernan, J. Hemmler, G. Heyler, D. Humm, J. Hutcheson, N. Izenberg, R.
2032 Lee, J. Lees, D. Lohr, E. Malaret, T. Martin, J.A. McGovern, P. McGuire, R. Morris, J. Mustard, S.
2033 Pelkey, E. Rhodes, M. Robinson, T. Roush, E. Schaefer, G. Seagrave, G. Seelos, P. Silverglate, S.
2034 Slavney, M. Smith, W.J. Shyong, K. Strohbehn, H. Taylor, P. Thompson, B. Tossman, M.
2035 Wirzburger, M. Wolff, Compact Reconnaissance Imaging Spectrometer for Mars (CRISM) on
2036 Mars Reconnaissance Orbiter (MRO), J. Geophys. Res. **112** (2007) doi:10.1029/2006JE002682
2037 J.R. Murphy, S. Nelli, Mars Pathfinder convective vortices: Frequency of occurrence, Geophys. Res.
2038 Lett **29**, 11–14 (2002) doi: 10.1029/2002GL015214
2039 T. Navarro, J.-B. Madeleine, F. Forget, A. Spiga, E. Millour, F. Montmessin, A. Määttänen, Global
2040 climate modeling of the Martian water cycle with improved microphysics and radiatively active
2041 water ice clouds, J. Geophys. Res. Planets **119**, 1479–1495 (2014) doi:10.1002/2013JE004550
2042 L.D.V. Neakrase, J. McHone, P.L. Whelley, R. Greeley, Saharan dust devil tracks: Mars analog field
2043 study areas, in Abstracts with Programs, Geol. Soc. Am., Houston, TX, Abst#. 40, 262 (2008)
2044 L.D.V. Neakrase, J. McHone, P.L. Whelley, R. Greeley, Terrestrial analogs to Mars: East-central
2045 Saharan dust devil tracks, in Lunar Planet. Sci. Conf. XLIII, League City, TX, Abst. #2009 (2012).
2046 F.M. Neubauer, Thermal convection in the martian atmosphere, J. Geophys. Res. **71**:10, 2419–2426
2047 (1966) doi:10.1029/JZ071i010p02419
2048 G.A. Neumann, D.E. Smith, M.T. Zuber, Two Mars years of clouds detected by the Mars Orbiter Laser
2049 Altimeter, J. Geophys. Res. **108**, 5023 (2003) doi:10.1029/2002JE001849
2050 C.E. Newman, S.R. Lewis, P.L. Read, F. Forget, Modeling the Martian dust cycle, 1. Representations of
2051 dust transport processes, J. Geophys. Res., **107**:E12, 5123 (2002a) doi:10.1029/2002JE001910
2052 C.E. Newman, S.R. Lewis, P.L. Read, F. Forget, Modeling the Martian dust cycle 2. Multiannual
2053 radiatively active dust transport simulations, J. Geophys. Res. **107**:E12, 5124 (2002b)
2054 doi:10.1029/2002JE001920
2055 C.E. Newman, S.R. Lewis, P.L. Read The atmospheric circulation and dust activity in different orbital
2056 epochs on Mars, Icarus **174**, 135–160 (2005) doi: 10.1016/j.icarus.2004.10.023
2057 A.H. Omar, D.M. Winker, M.A. Vaughan, Y. Hu, C.R. Trepte, R.A. Ferrare, K.-P. Lee, C.A. Hostetler,
2058 C. Kittaka, R. Rogers, R.E. Kuehn, Z. Liu, The CALIPSO Automated Aerosol Classification and
2059 Lidar Ratio Selection Algorithm. J Atmos. Oceanic Technol., **26**, 1994–2014 (2009)
2060 doi:10.1175/2009JTECHA1231.1
2061 A.V. Pathare, M.R. Balme, S.M. Metzger, A. Spiga, M.C. Towner, N.O. Renno, F. Saca, Assessing the
2062 power law hypothesis for the size–frequency distribution of terrestrial and martian dust devils,
2063 Icarus **209**, 851–853 (2010) doi:10.1016/j.icarus2010.06.027
2064 S. Peyridieu, A. Chédin, D. Tanré, V. Capelle, C. Pierangelo, N. Lamquin, R. Armante, Saharan dust
2065 infrared optical depth and altitude retrieved from AIRS: a focus over North Atlantic – comparison
2066 to MODIS and CALIPSO, Atmos. Chem. Phys. **10**:4, 1953-1967 (2010) doi:10.5194/acp-10-1953-
2067 2010
2068 A. Petrosyan, B. Galperin, S.E. Larsen, S.R. Lewis, A. Määttänen, P.L. Read, N. Renno, L.P.H.T.
2069 Rogberg, H. Savijrvi, T. Siili, A. Spiga, A. Toigo, L. Vázquez, The Martian atmospheric boundary
2070 layer, Rev. Geophys. **49** (2011) doi:10.1029/2010RG000351
2071 J.M.C. Plane, Cosmic dust in the Earth's atmosphere, Chem. Soc. Rev. **41**:19, 6507–6518 (2012)
2072 doi:10.1039/C2CS35132C
2073 J.B. Pollack, D.S. Colburn, F.M. Flasar, R. Kahn, C.E. Carlston, D. Pidek, Properties and effects of dust
2074 particles suspended in the Martian atmosphere, J. Geophys. Res. **84**, (1979)
2075 doi:10.1029/JB084iB06p02929

2076 J.M. Prospero, P.J. Lamb, African droughts and dust transport to the Caribbean: climate change
2077 implications, Science **302**, 1024–1027 (2003) doi:10.1126/science.1089915
2078 J.M. Prospero, P. Ginoux, O. Torres, S.E. Nicholson, T.E. Gill, Environmental characterization of global
2079 sources of atmospheric soil dust identified with the Nimbus 7 Total Ozone Mapping Spectrometer
2080 (TOMS) absorbing aerosol product, Rev. Geophys. **40**:1, 1002 (2002) doi:10.1029/2000RG000095
2081 J.M. Prospero, J.E. Bullard, R. Hodgkins, High-latitude dust over the North Atlantic: Inputs from
2082 Icelandic proglacial dust storms, Science **335**, 1078–1082 (2012) doi:10.1126/science.1217447
2083 N. Putzig, M. Mellon, K. Kretke, R. Arvidson, Global thermal inertia and surface properties of Mars
2084 from the MGS mapping mission, Icarus **173**:2, 325–341 (2005) doi:10.1016/j.icarus.2004.08.017
2085 S.C.R. Rafkin, The potential importance of non-local, deep transport on the energetics, momentum,
2086 chemistry, and aerosol distributions in the atmospheres of Earth, Mars, and Titan, Planet. Space
2087 Sci. **60**, 147–154 (2012) doi:10.1016/j.pss.2011.07.015
2088 S.C.R. Rafkin, M.R.V. Sta. Maria, T.I. Michaels, Simulation of the atmospheric thermal circulation of a
2089 martian volcano using a mesoscale numerical model, Nature **419**:6908, 697–699 (2002)
2090 doi:10.1038/nature01206
2091 P.L. Read, S.R. Lewis, The Martian Climate Revisited: Atmosphere and Environment of a Desert Planet
2092 (Springer Praxis Books, Berlin, New York, 2004)
2093 H.E. Redmond, K.D. Dial KD, J.E. Thompson, Light scattering and absorption by wind blown dust:
2094 Theory, measurement, and recent data, Aeolian Res **2**:1, 5–26 (2010)
2095 doi:10.1016/j.aeolia.2009.09.002
2096 D. Reiss, D. Lüsebrink, H. Hiesinger, T. Kelling, G. Wurm, J. Teiser, High altitude dust devils on Arsia
2097 Mons: Testing the greenhouse and thermophoresis hypothesis of dust lifting, in Lunar and
2098 Planetary Science Conference XL, The Woodlands, TX, Abst. #1961 (2009)
2099 D. Reiss, J. Raack, A.P. Rossi, G. Di Achille, H. Hiesinger, First in-situ analysis of dust devil tracks on
2100 Earth and their comparison with tracks on Mars, Geophys. Res. Lett. **37**:L14203 (2010) doi:
2101 10.1029/2010GL044016
2102 D. Reiss, J. Raack, H. Hiesinger, Bright dust devil tracks on Earth: Implications for their formation on
2103 Mars, Icarus **211**, 917–920 (2011a) doi:10.1016/j.icarus.2010.09.009
2104 D. Reiss, M. Zanetti, G. Neukum, Multitemporal observations of identical active dust devils on Mars
2105 with the High Resolution Stereo Camera (HRSC) and Mars Orbiter Camera (MOC), Icarus **215**,
2106 358–369 (2011b) doi:10.1016/j.icarus.2011.06.011
2107 D. Reiss, M.I. Zimmerman, D.C. Lewellen, Formation of cycloidal dust devil tracks by redeposition of
2108 coarse sands in southern Peru: Implications for Mars, Earth Planet. Sci. Lett. **383**, 7–15 (2013)
2109 10.1016/j.epsl.2013.09.033
2110 D. Reiss, A. Spiga, G. Erkeling, The horizontal motion of dust devils on Mars derived from CRISM and
2111 CTX/HiRISE observations, Icarus **227**, 8–20 (2014a) 10.1016/j.icarus.2013.08.028
2112 D. Reiss, N.M. Hoekzema, O.J. Stenzel, Dust deflation by dust devils on Mars derived from optical
2113 depth measurements using the shadow method in HiRISE images, Planet. Space Sci. **93-94**, 54–64
2114 (2014b) 10.1016/j.pss.2014.01.016
2115 L.A. Remer, R.G. Kleidman, R.C. Levy, Y.J. Kaufman, D. Tanré, S. Mattoo, J.V. Martins, C. Ichoku, I.
2116 Koren, H. Yu, B.N. Holben, Global aerosol climatology from the MODIS satellite sensors, J.
2117 Geophys. Res. **113**, D14S07 (2008) doi:10.1029/2007JD009661
2118 N.O. Rennó, M.L. Burkett, M.P. Larkin, A simple thermodynamical theory for dust devils, J. Atmos.
2119 Sci. **55**, 3244–3252 (1998) doi:10.1175/1520-0469(1998)055<3244:ASTTFD>2.0.CO;2
2120 N.O. Rennó, A.A. Nash, J. Lunine, J. Murphy, Martian and terrestrial dust devils: Test of a scaling
2121 theory using Pathfinder data, J. Geophys. Res. **105**, 1859–1865 (2000) doi:10.1029/1999JE001037
2122 N.O. Rennó, V.J. Abreu, J. Koch, P.H. Smith, O.K. Hartogensis, H.A.R. De Bruin, D. Burose, G.T.
2123 Delory, W.M. Farrell, C.J. Watts, J. Garatuza, M. Parker, A. Carswell, MATADOR 2002: A pilot
2124 field experiment on convective plumes and dust devils, J. Geophys. Res. **109** (2004)
2125 doi:10.1029/2003JE002219
2126 T.J. Ringrose, M.C. Towner, J.C. Zarnecki, Convective vortices on Mars: a reanalysis of Viking Lander
2127 2 meteorological data, sols 1–60, Icarus **163**, 78–87 (2003) doi:10.1016/S0019-1035(03)00073-3
2128 A.P. Rossi, L. Marinangeli, The first terrestrial analogue to Martian dust devil tracks found in Ténéré
2129 Desert, Niger, Geophys. Res. Lett. **31**, L06702 (2004) doi:10.1029/2004GL019428
2130 J.A. Ryan, Notes on the martian yellow clouds, J. Geophys. Res. **69**:18, 3759–3770 (1964)
2131 doi:10.1029/JZ069i018p03759

J.A. Ryan, J.J. Carroll, Dust devil wind velocities: Mature state, J. Geophys. Res. **75**, 531–541 (1970) doi:10.1029/JC075i003p00531
J.A. Ryan, R.D. Lucich, Possible dust devils, vortices on Mars, J. Geophys. Res. **88**:C15, 11,005–11,011, (1983) doi:10.1029/JC088iC15p11005.
K. Schepanski, I. Tegen, M.C. Todd, B. Heinold, G. Bonisch, B. Laurent, A. Macke, Meteorological processes forcing Saharan dust emission inferred from MSG-SEVIRI observations of subdaily dust source activation and numerical models, J. Geophys. Res. **114**:D10201 (2009) doi:10.1029/2008JD010325.
A. Schnapf, TIROS: A Story of Achievement, AED P-5167A (Radio Corporation of America, Princeton, New Jersey, USA, 1964), p. 37
J.T. Schofield, J.R. Barnes, D. Crisp, R.M. Haberle, S. Larsen, J.A. Magalhães, J.R. Murphy, A. Seiff, G. Wilson, The Mars Pathfinder atmospheric structure investigation meteorology (ASI/MET) experiment, Science **278**, 1752–1758 (1997) doi:10.1126/science.278.5344.1752
P. C. Sinclair, Some preliminary dust devil measurements, Mon. Weather Rev. **92**, 363–367 (1964) doi:10.1126/science.27.693.594
P.C. Sinclair, On the rotation of dust devils, Bull. Am. Meteorol. Soc. **46**, 388–391 (1965)
P.C. Sinclair, General characteristics of dust devils, J. Appl. Meteorol. **8**, 32–45 (1969) doi:10.1175/1520-0450(1969)008<0032:GCODD>2.0.CO;2
P.C. Sinclair, The lower structure of dust devils, J. Atmos. Sci. **30**, 1599–1619 (1973) doi:10.1175/1520-0469(1973)030<1599:TLSODD>2.0.CO;2
A. Slingo, T.P. Ackerman, R.P. Allan, E.I. Kassianov, S.A. McFarlane, G.J. Robinson, J.C. Barnard, M.A. Miller, J.E. Harries, J.E. Russell, S. Dewitte, Observations of the impact of a major Saharan dust storm on the atmospheric radiation balance, Geophys Res Lett **33**:L24817 (2006) doi:10.1029/2006GL027869D.E. Smith, M.T. Zuber, H.V. Frey, J.B. Garvin, J.W. Head, D.O. Muhleman, G.H. Pettengill, R.J. Phillips, S.C. Solomon, H.J. Zwally, W.B. Bannerdt, T.C. Duxbury, M.P. Golombek, F.g. Lemoine, G.A. Neumann, D.D. Rowlands, O. Aharonson, P.G. Ford, A.B. Ivanov, C.L. Johnson, P.J. McGovern, J.B. Abshire, R.S. Afzal, X. Sun, Mars Orbiter Laser Altimeter: Experiment summary after the first year of global mapping of Mars, J. Geophys. Res. **106**, 23,689–23,722 (2001) doi:10.1029/2000JE001364
M.D. Smith, J.C. Pearl, B.J. Conrath, P.R. Christensen, Mars Global Surveyor Thermal Emission Spectrometer (TES) observations of dust opacity during aerobraking and science phasing, J. Geophys. Res. **105**, 9539–9552 (2000) doi:10.1029/1999JE0010
M.D. Smith, J.C. Pearl, B.J. Conrath, P.R. Christensen, One Martian year of atmospheric observations by the Thermal Emission Spectrometer, Geophys. Res. Lett. **28**, 4263–4266 (2001) doi:10.1029/2001GL013608
M.D. Smith, Interannual variability in TES atmospheric observations of Mars during 1999–2003, Icarus **167**:1, 148–165 (2004) doi:10.1016/j.icarus.2003.09.010
M.D. Smith, M.J. Wolff, M.T. Lemmon, N. Spanovich, D. Banfield, C.J. Budney, R.T. Clancy, A. Ghosh, G.A. Landis, P. Smith, B. Whitney, P.R. Christensen, S.W. Squyres, First atmospheric science results from the Mars exploration rovers Mini-TES, Science **306**, 1750–1753 (2004) doi:10.1126/science.1104257
M.D. Smith, M.J. Wolff, R.T. Clancy, A. Kleinböhl, S.L. Murchie, Vertical distribution of dust and water ice aerosols from CRISM limb-geometry observations, J. Geophys. Res. **118**, 321–334 (2013) doi:10.1002/jgre.20047
P.H. Smith, M. Lemmon, Opacity of the Martian atmosphere measured by the Imager for Mars Pathfinder, J. Geophys. Res. **104**, 8975 (1999) doi:10.1029/1998JE900017
J.T. Snow, T.M. McClelland, Dust devils at White Sands Missile Range, New Mexico 1. Temporal and spatial distributions, J. Geophys. Res. **95**, 13707–13721 (1990) doi:10.1029/JD095iD09p13707
C.W. Snyder, V.I. Moroz, Spacecraft exploration of Mars, in: Mars, ed. By H.H. Kieffer, B.M. Jakosky, C.W. Snyder, M.S. Matthews (University of Arizona Press, Tucson, 1992) pp. 71-119
A. Spiga, F. Forget, A new model to simulate the Martian mesoscale and microscale atmospheric circulation: Validation and first results, J. Geophys. Res. **114** (2009) doi:10.1029/2008je003242
A. Spiga, F. Forget, S.R. Lewis, D.P. Hinson, Structure and dynamics of the convective boundary layer on mars as inferred from large-eddy simulations and remote-sensing measurements, Q. J. R. Meteorol. Soc. **136**, 414–428 (2010) doi:10.1002/qj.563

2187 A. Spiga, S.R. Lewis, Martian mesoscale and microscale wind variability of relevance for dust lifting,
2188 Mars **5**, 146–158 (2010) doi:10.1555/mars.2010.0006
2189 J.D. Spinhirne, S.P. Palm, W.D. Hart WD, D.L. Hlavka, E.J. Welton, Cloud and aerosol measurements
2190 from GLAS: Overview an initial results, Geophys. Res. Lett. **32** (2005) doi:
2191 10.1029/2005GL023507
2192 C. Stanzel, M. Pätzold, R. Greeley, E. Hauber, G. Neukum, Dust devils on Mars observed by the High
2193 Resolution Stereo Camera, Geophys. Res. Lett. **33**:L11202 (2006) doi:10.1029/2006GL025816
2194 C. Stanzel, Studying martian dust devils by applying pattern recognition algorithms to multi-mission
2195 camera images, PhD Thesis, University of Cologne (2007) 158 pp.
2196 C. Stanzel, M. Pätzold, D.A. Williams, P.L. Whelley, R. Greeley, G. Neukum, The HRSC Co-
2197 Investigator Team, Dust devil speeds, directions of motion and general characteristics observed by
2198 the Mars Express High Resolution Stereo Camera, Icarus **197**, 39–51 (2008)
2199 doi:10.1016/j.icarus2008.04.017
2200 L.J. Steele, S.R. Lewis, M.R. Patel, The radiative impact of water ice clouds from a reanalysis of Mars
2201 Climate Sounder data, Geophys. Res. Lett. **41**, 4471–4478 (2014a) doi:10.1002/2014GL060235
2202 L.J. Steele, S.R. Lewis, M.R. Patel, F. Montmessin, F. Forget, M.D. Smith, The seasonal cycle of water
2203 vapour on Mars from assimilation of thermal emission spectrometer data, Icarus **237**, 97–115
2204 (2014b) doi:10.1016/j.icarus.2014.04.017
2205 M.J. Strausberg, H. Wang, M.I. Richardson, S.P. Ewald, A.D. Toigo, Observations of the initiation and
2206 evolution of the 2001 Mars global dust storm, J. Geophys. Res. **110**:E02006 (2005)
2207 doi:10.1029/2004JE002361
2208 R. Swap, S. Ulanski, M. Cobbett, M. Garstang, Temporal and spatial characteristics of Saharan dust
2209 outbreaks, J. Geophys. Res. **101**:D2, 4205–4220 (1996) doi:10.1029/95JD03236
2210 M.A. Szwast, M.I. Richardson, A.R. Vasavada, Surface dust redistribution on Mars as observed by the
2211 Mars Global Surveyor and Viking orbiters, J. Geophys. Res. **111**:E11008 (2006)
2212 doi:10.1029/2005JE002485
2213 D. Tanré, F.M. Bréon, J.L. Deuzé, O. Dubovik, F. Ducos, P. François, P. Goloub, M. Herman, A.
2214 Lifermann, F. Waquet, Remote sensing of aerosols by using polarized, directional and spectral
2215 measurements within the A-Train: the PARASOL mission, Atmos. Meas. Tech. **4**, 1383-1395,
2216 (2011) doi: 10.5194/amt-4-1383-2011
2217 P. Thomas, P.J. Gierasch, Dust devils on Mars, Science **230**, 175–177 (1985)
2218 doi:10.1126/science.230.4722.175
2219 O. Torres, P.K. Bhartia, J.R. Herman, Z. Ahmad, Derivation of aerosol properties from satellite
2220 measurements of backscattered ultraviolet radiation: Theoretical basis, J. Geophys. Res. **103**,
2221 17,099–17,110 (1998) doi:10.1029/98JD00900
2222 M.C. Towner, Characteristics of large Martian dust devils using Mars Odyssey Thermal Emission
2223 Imaging System visual and infrared images, J. Geophys. Res. **114**, E02010 (2009)
2224 doi:10.1029/2008JE003220
2225 D.M. Tratt, M.H. Hecht, D.C. Catling, E.C. Samulon, P.H. Smith, In situ measurement of dust devil
2226 dynamics: Toward a strategy for Mars, J. Geophys. Res. **108** (2003) doi:10.1029/2003JE002161
2227 United States, Catalogue of meteorological satellite data – TIROS VI television cloud photography. Key
2228 to Meteorological Records Documentation No. **5**:36, (1964) 400 pp.
2229 P. Vallelonga, A. Svensson, Ice core archives of mineral dust, in Mineral Dust: A Key Player in the
2230 Earth System, ed. By P. Knippertz, J.-B.W. Stuut (Springer, Dordrecht, 2014) p. 463
2231 doi:10.1007/978-94-017-8978-3
2232 H. Wang, M.I. Richardson, R.J. Wilson, A.P. Ingersoll, A.D. Toigo, R.W. Zurek, Cyclones, tides, and
2233 the origin of a cross-equatorial dust storm on Mars, Geophys. Res. Lett. **30** (2003)
2234 doi:10.1029/2002GL016828
2235 H. Wang, Dust storms originating in the northern hemisphere during the third mapping year of Mars
2236 Global Surveyor, Icarus **189**, 325–343 (2007) doi: 10.1016/j.icarus.2007.01.014
2237 H. Wang, J.A. Fisher, North polar frontal clouds and dust storms on Mars during spring and summer,
2238 Icarus **204**, 103–113 (2009) doi:10.1016/j.icarus.2009.05.028
2239 H. Wang, M.I. Richardson, The origin, evolution, and trajectory of large dust storms on Mars during
2240 Mars years 24–30 (1999–2011), Icarus **251**, 112–127 (2015) doi:10.1016/j.icarus.2013.10.033
2241 A. Wennmacher, F.M. Neubauer, M. Pätzold, J. Schmitt, K. Schulte, A search for dust devils on Mars,
2242 in Lunar Planet. Sci. Conf. XXVII, League City, TX, Abst. #1417 (1996)

P.L. Whelley, R. Greeley, The distribution of dust devil activity on Mars, J. Geophys. Res. **113**:E7 (2008) doi:10.1029/2007JE002966
N.R. Williams, Development of dust whirls and similar small-scale vortices, Bull. Am. Meteorol. Soc. **29**, 106–117 (1948)
G.E. Willis, J.W. Deardorff, Laboratory observations of turbulent penetrative convection planforms, J. Geophys. Res. **84**, 295–302 (1979) doi:10.1029/JC084iC01p00295
R.J. Wilson, S.R. Lewis, L. Montabone, M.D. Smith, Influence of water ice clouds on Martian tropical atmospheric temperatures, Geophys. Res. Lett. **35** (2008) doi:10.1029/2007GL032405
G. Winckler, R.F. Anderson, D. McGee, M.Q. Fleisher, N. Mahowald, Half a million years of coherent dust flux variations in the tropical Pacific and Antarctica, in 8th Annual V M Goldschmidt Conference (Pergamon-Elsevier Science Ltd., Vancouver, Canada) pp. A1026
D.M. Winker, J. Pelon J.A. Coakley Jr., S.A. Ackerman, R.J. Charlson, P.R. Colarco, P. Flamant, Q. Fu, R.M. Hoff, C. Kittaka, T.L. Kubar, H. Le Treut, M.P. McCormick, G. Mégie, L. Poole, K. Powell, C. Trepte, M.A. Vaughan, B.A. Wielicki, The CALIPSO mission: A global 3D view of aerosols and clouds, Bull. Amer. Meteor. Soc. **91**, 1211–1229 (2010) doi:10.1175/2010BAMS3009.1
M.J. Wolff, M.D. Smith, R.T. Clancy, R. Arvidson, M. Kahre, F. Seelos, S. Murchie, H. Savijärvi, Wavelength dependence of dust aerosol single scattering albedo as observed by the Compact Reconnaissance Imaging Spectrometer, J. Geophys. Res. **114**:E00D04 (2009) doi:10.1029/2009JE003350
S. Wong, A.E. Dessler, N.M. Mahowald, P. Yang, Q. Feng, Maintenance of lower tropospheric temperature inversion in the Saharan Air Layer by dust and dry anomaly, J. Climate **22**:19, 5149-5162 (2009) doi:10.1175/2009JCLI2847.1
F. Yang, P.A. Mlsna, P. Geissler, Gaussian-based filters for detecting martian dust devils, in 2006 IEEE Southwest Symp. Image Anal. Interpret. **3**, 46–50 (2006) doi:10.1109/SSIAI.2006.1633719
H. Yu, M. Chin, T. Yuan, H. Bian, L.A. Remer, J.M. Prospero, A. Omar, D. Winker, Y. Yang, Y. Zhang, Z. Zhang, C. Zhao, The fertilizing role of African dust in the Amazon rainforest: A first multiyear assessment based on data from Cloud-Aerosol Lidar and Infrared Pathfinder Satellite Observations, Geophys. Res. Lett. **42** (2015) doi:10.1002/2015GL063040
M.T. Zuber, D.E. Smith, S.C. Solomon, D.O. Muhleman, J.W. Head, J.B. Garvin, J.B. Abshire, and J.L. Bufton, The Mars Observer Laser Altimeter Investigation, J. Geophys. Res. **97**:E5, 7781–7797 (1992) doi:10.1029/92JE00341.
Zasova, L. V. Formisano, N. Moroz, D. Grassi, N. Ignatiev, M. Giuranna, G. Hansen, M. Blecka, A. Ekonomov, E. Lellouch, S. Fonti, A. Grigoriev, H. Hirsch, I. Khatuntsev, A. Mattana, A. Maturilli, A. Moshkin, D. Patsaev, G. Piccioni, M. Rataj, B. Saggin, Water clouds and dust aerosols observations with PFS MEX at Mars, Planet. Space Sci. **53**, 1065–1077 (2005) doi:10.1016/j.pss.2004.12.010
A. Zhu, V. Ramanathan, F. Li, D. Kim, Dust plumes over the Pacific, Indian, and Atlantic oceans: Climatology and radiative impact, J. Geophys. Res. **112**:D16208 (2007) doi:10.1029/2007JD008427
R.W. Zurek, J.R. Barnes, R.M. Haberle, J.B. Pollack, J.E. Tillman, C.B. Leovy, Dynamics of the atmosphere of Mars, in: Mars, ed. By H.H. Kieffer, B.M. Jakosky, C.W. Snyder, M.S. Matthews (University of Arizona Press, Tucson, 1992) pp. 835–933

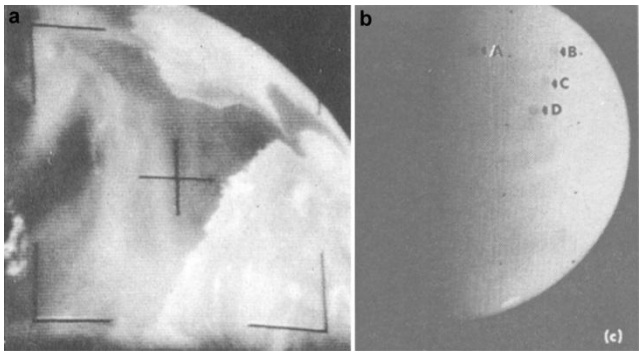

Figure 1. Early spacecraft images of dust storms. a) An early image of dust over the Arabian Sea and Gulf of Oman; the view is towards the southwest, with Iran and Pakistan on the right and the Arabian Peninsula on the left. (Image from Schnapf, 1964) b) In 1971, Mariner 9 entered orbit around Mars during an intense, global dust storm, that obscured all surface features except for four tall volcano peaks (labeled A through D) and the south polar cap (white spot at lower right). Image from Masursky et al. 1972.

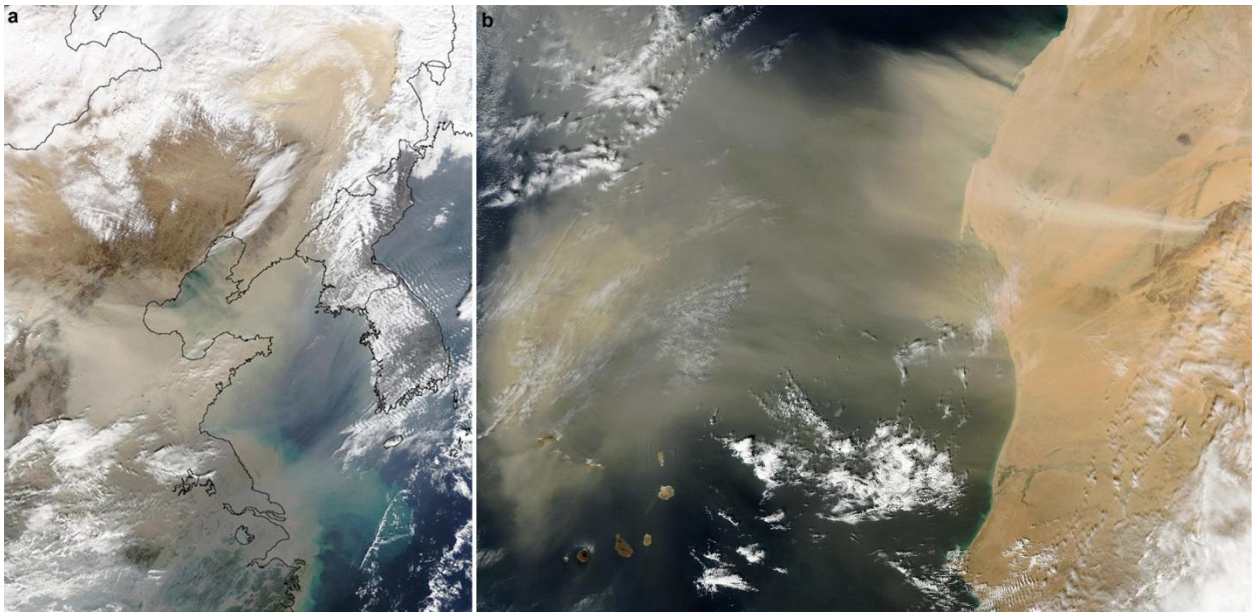

Figure 2. Visible MODIS images of dust plumes over a) the Yellow Sea and b) downwind of North Africa. Adapted from Marticorena and Formenti (2013).

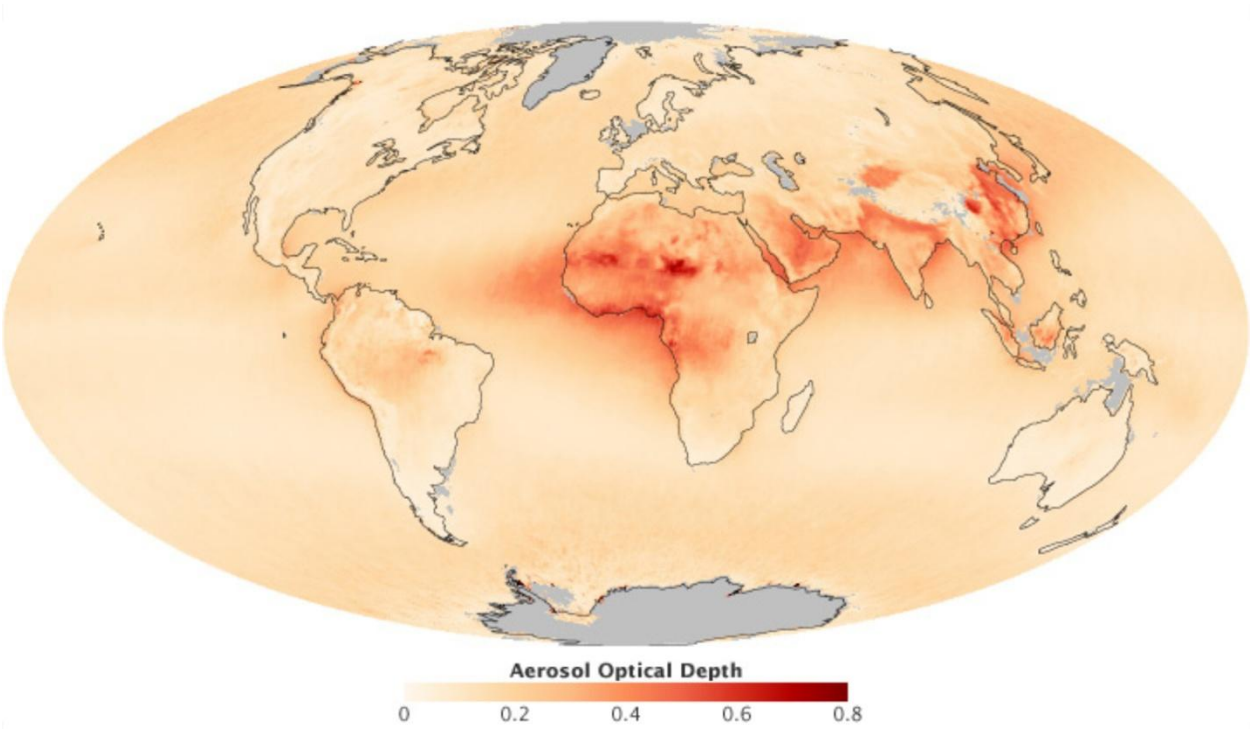

Figure 3. Mean Aerosol Optical Depth (AOD, which is used interchangeably with AOT) from June 2000 through May 2010 from MISR. (NASA map by Robert Simmon, based on MISR data.)

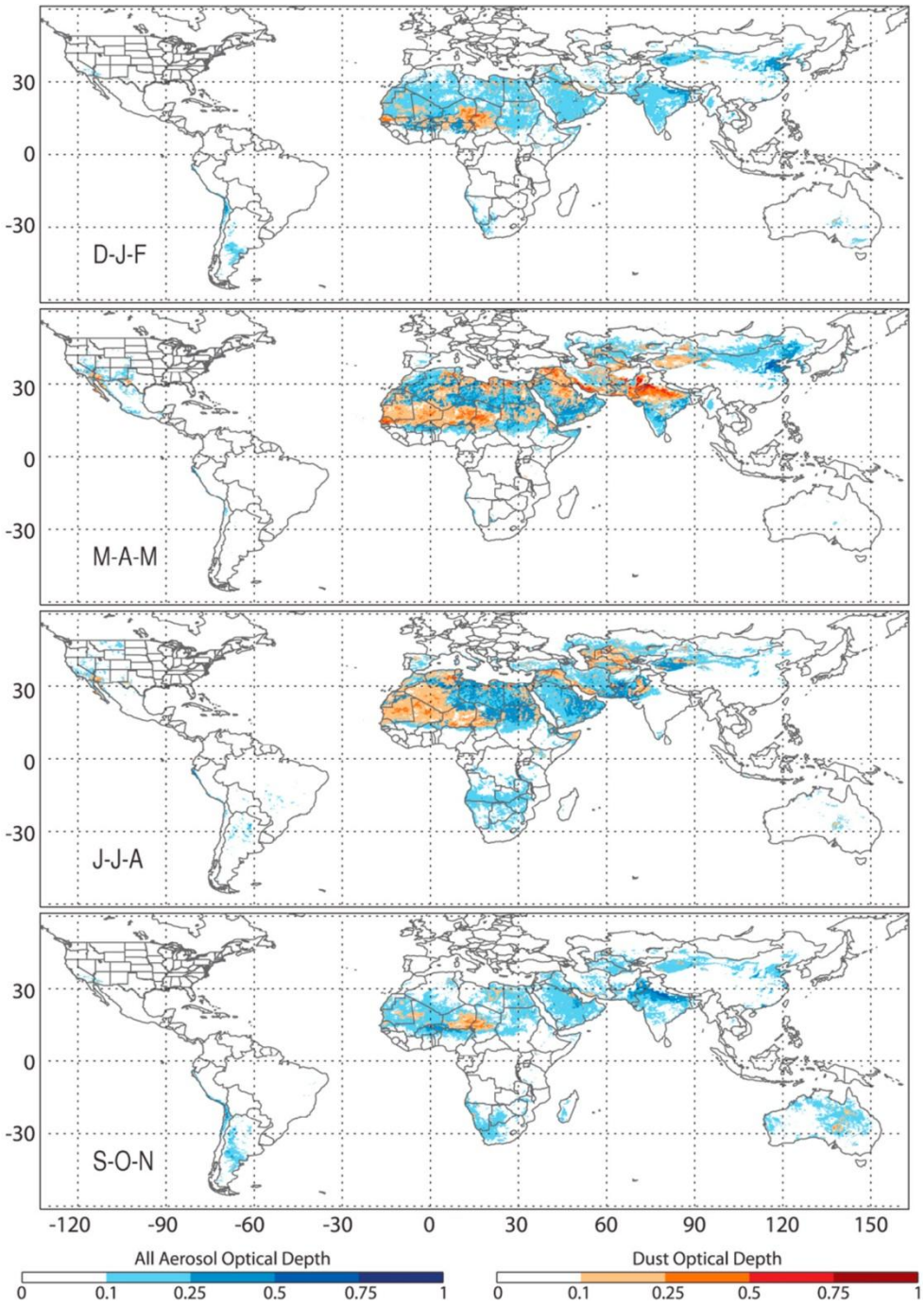

Figure 4. Seasonal distribution of AOT (blue) and DOD (yellow to red) measured from MODIS Deep Blue aerosol products, from Ginoux et al. (2012). AOT is sensitive to all particulates, whereas DOD is derived from AOT and considered representative of mineral dust from natural sources.

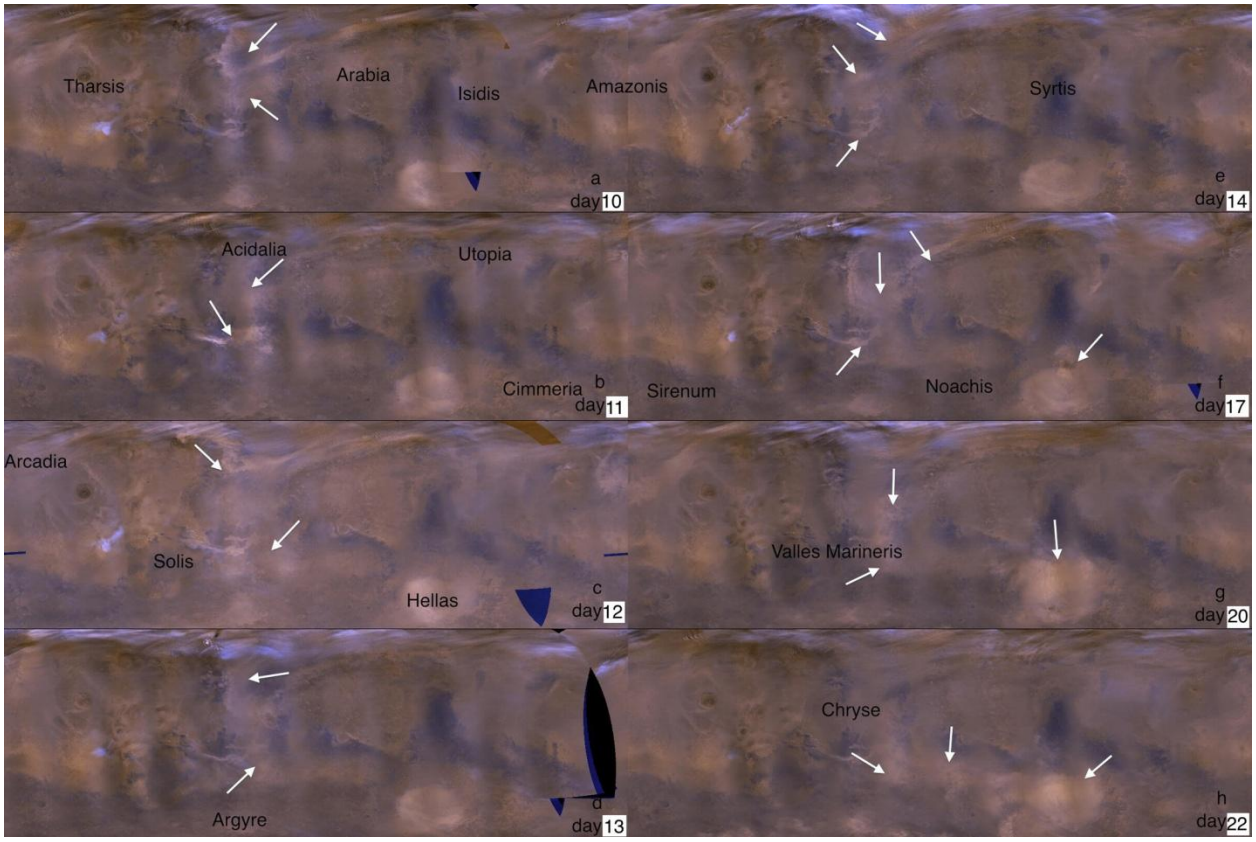

Figure 5. Characteristic evolution of dust storms (from Wang and Richardson 2015) showing 60ºS to 60ºN in a cylindrical projection for L_s=214-228º in MY 27 (2005). Numbers indicate the relative sol.

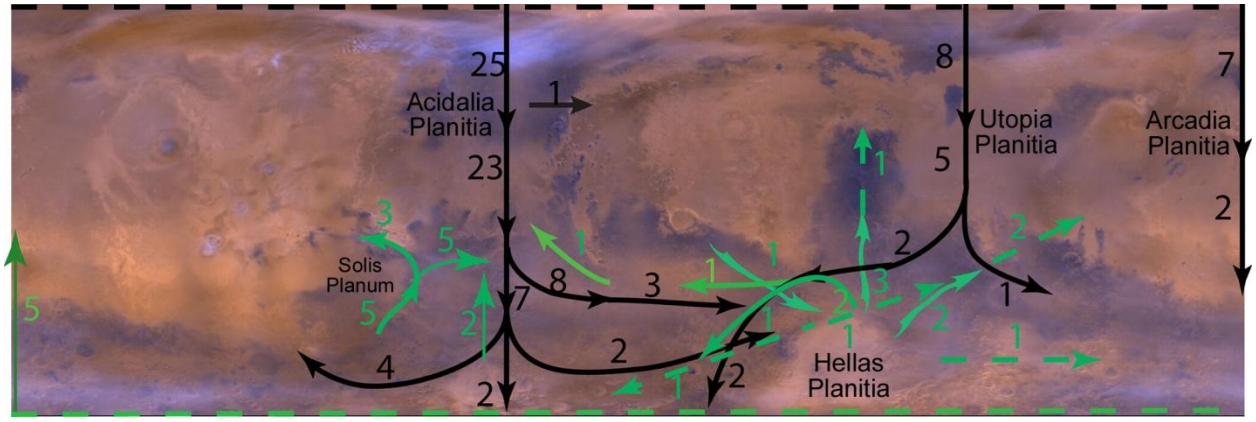

Figure 6. Routes for storm sequences as described (modified from Wang and Richardson 2015). Black indicates storms of northern origin; green indicates those of southern origin; dashed lines indicate polar storms. Numbers indicate how many storms were observed in each trajectory segment.

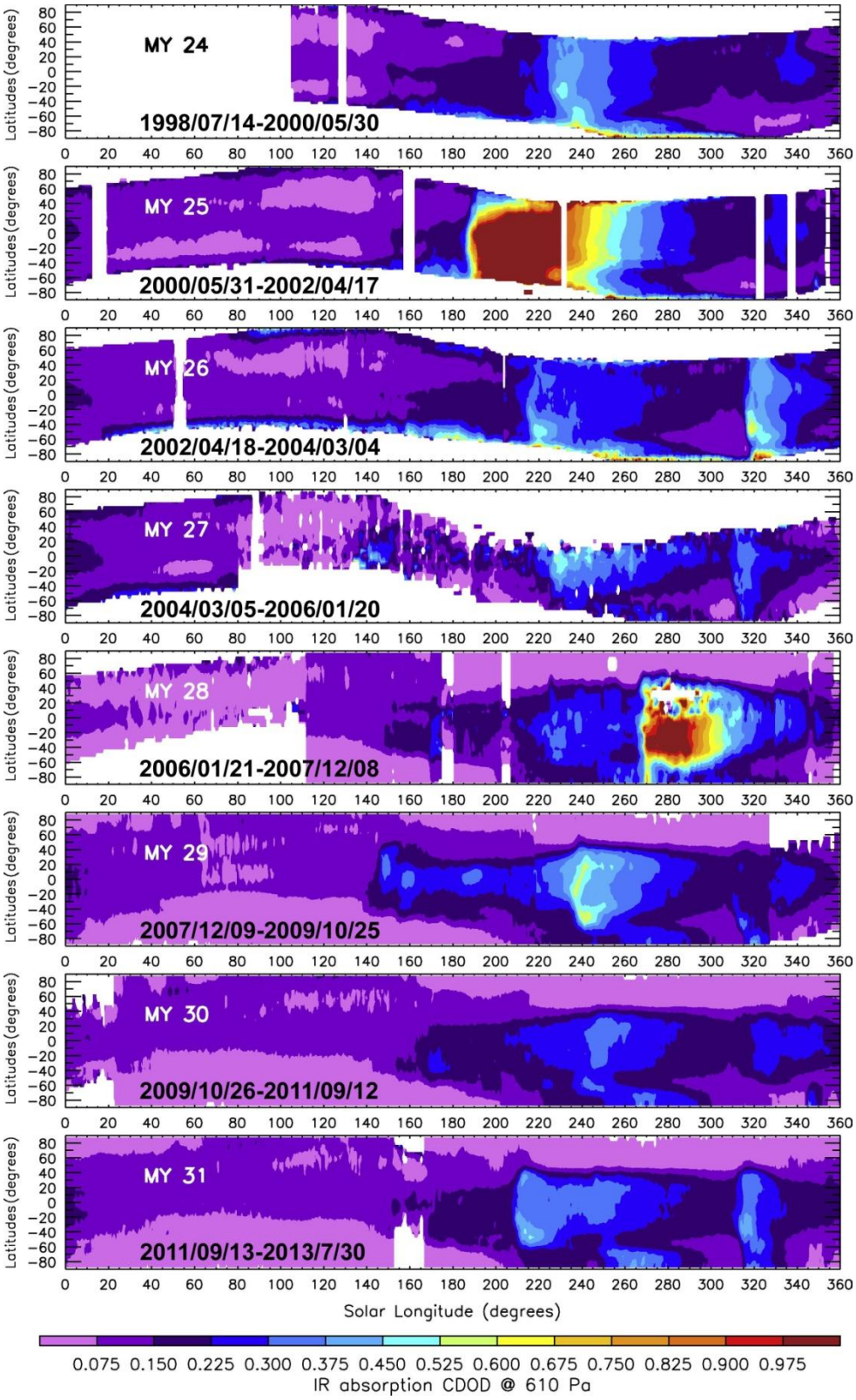

Figure 7. Climatology of column dust optical depth (CDOD) at 9.3 µm spanning MYs 24-31 (April 1999 – July 2013), from Montabone et al. (2015).

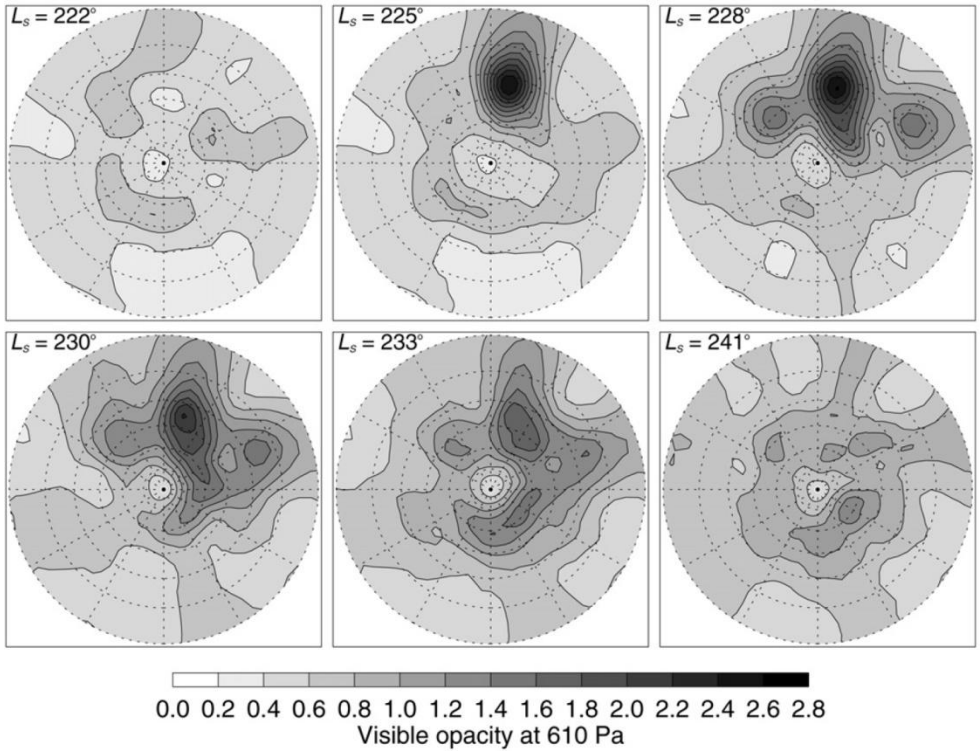

Figure 8. Visible optical depth from the model assimilation at six intervals during the MY 23 (1997) Noachis dust storm, normalized to 610 Pa to remove topographic effects (from Lewis et al. 2007). The plots are in polar stereographic projection with the south pole at the center, the equator at the edge, and with the prime meridian pointing upward.

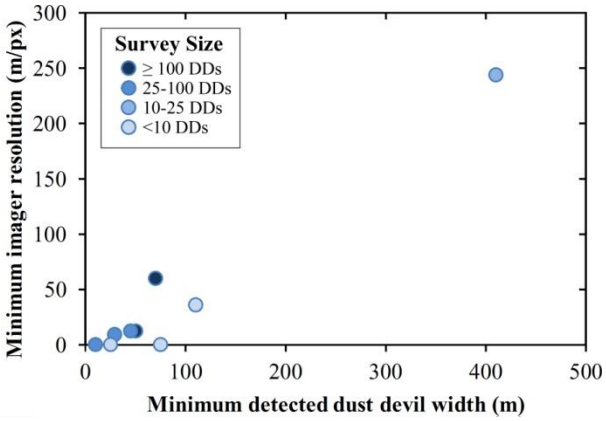

Figure 9. The minimum detected dust devil diameter on Mars from different orbital image surveys, showing a trend towards smaller dust devils with increased sensor resolution.

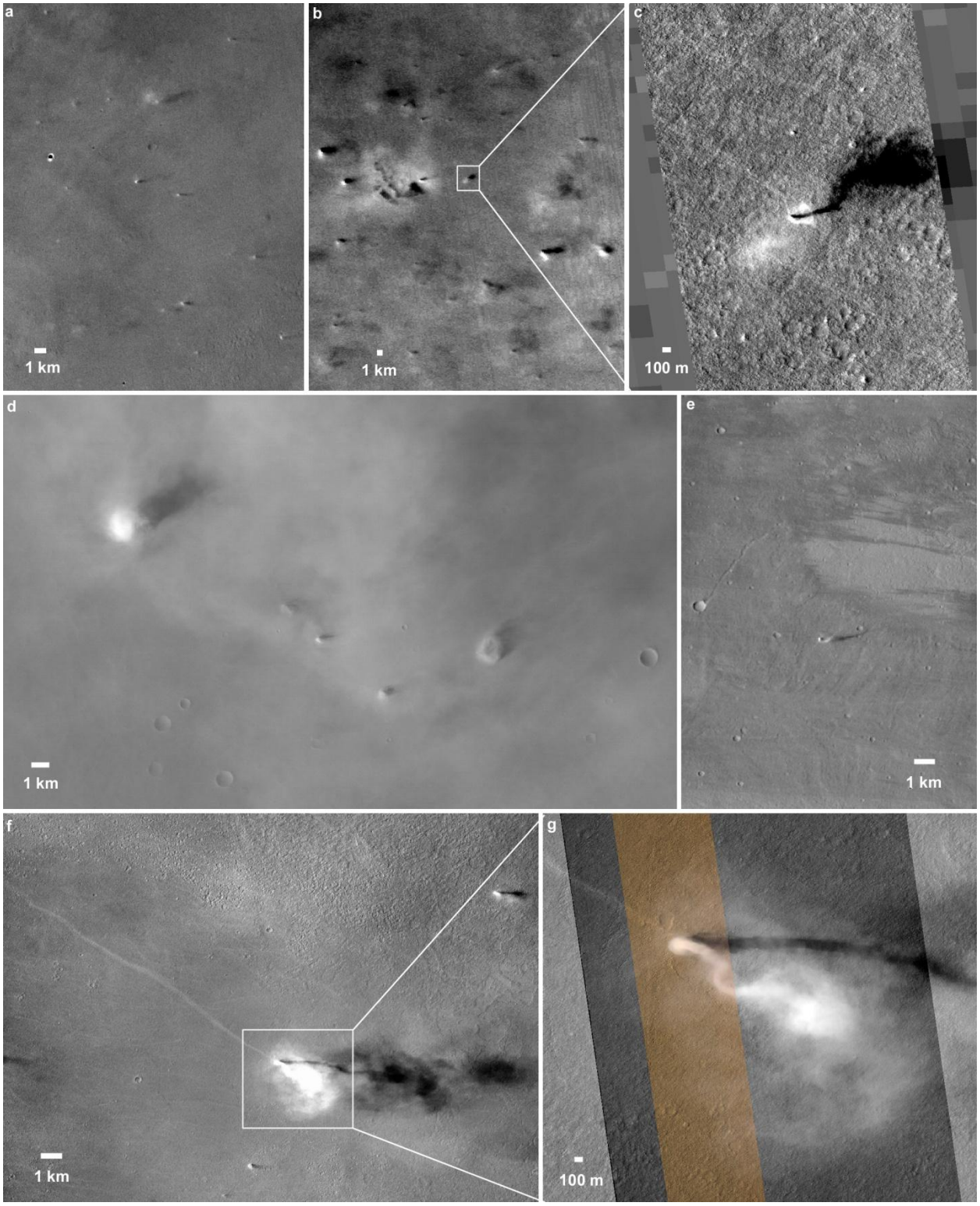

Figure 10. Examples of dust devils imaged by cameras orbiting Mars. a) VO2 image 038B25, b) MOC WA image E23/01275, with box showing the location of the concurrent c) MOC NA image E23/01274, d) HRSC image H2054_0000_ND3, e) THEMIS VIS image V02326010, f) CTX image G21_026394_2155, with a box

showing the location of the concurrent g) HiRISE image ESP_026394_2160 (both color and red images are shown).

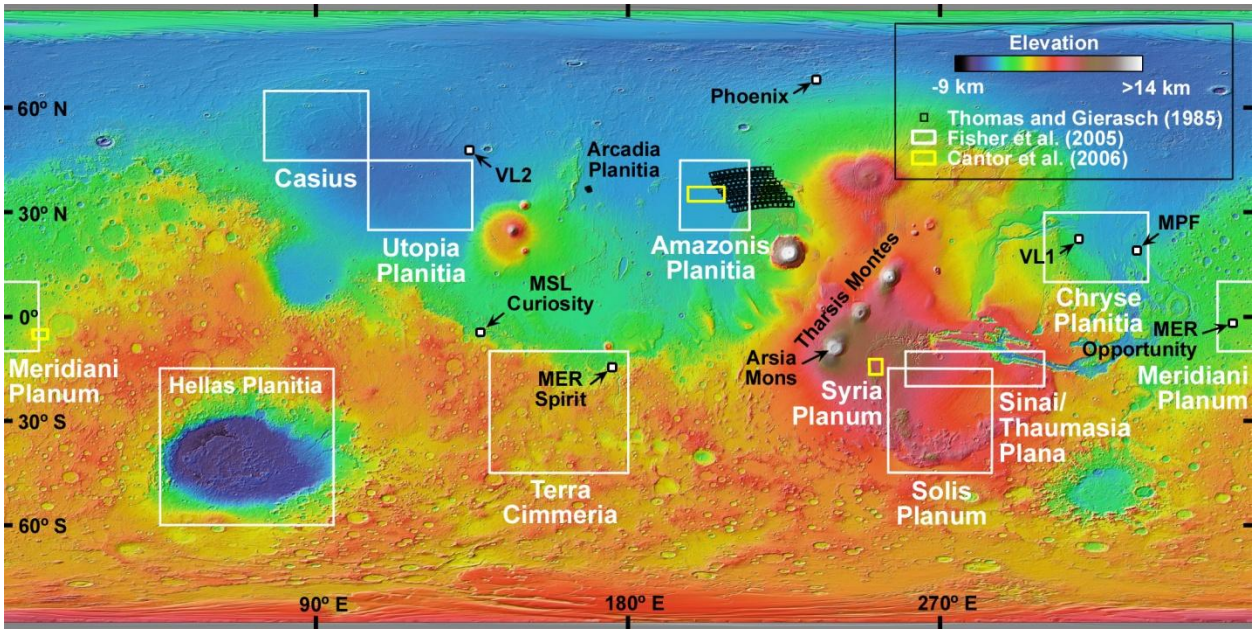

Figure 11. A MOLA shaded relief map of Mars with colorized elevation, showing locations referred to in this work. DD monitoring sites for three global-scale surveys are noted. Note that Cetal06's study included nearly the entire planet and that the regions indicated here are those with dedicated image targeting for DD activity.

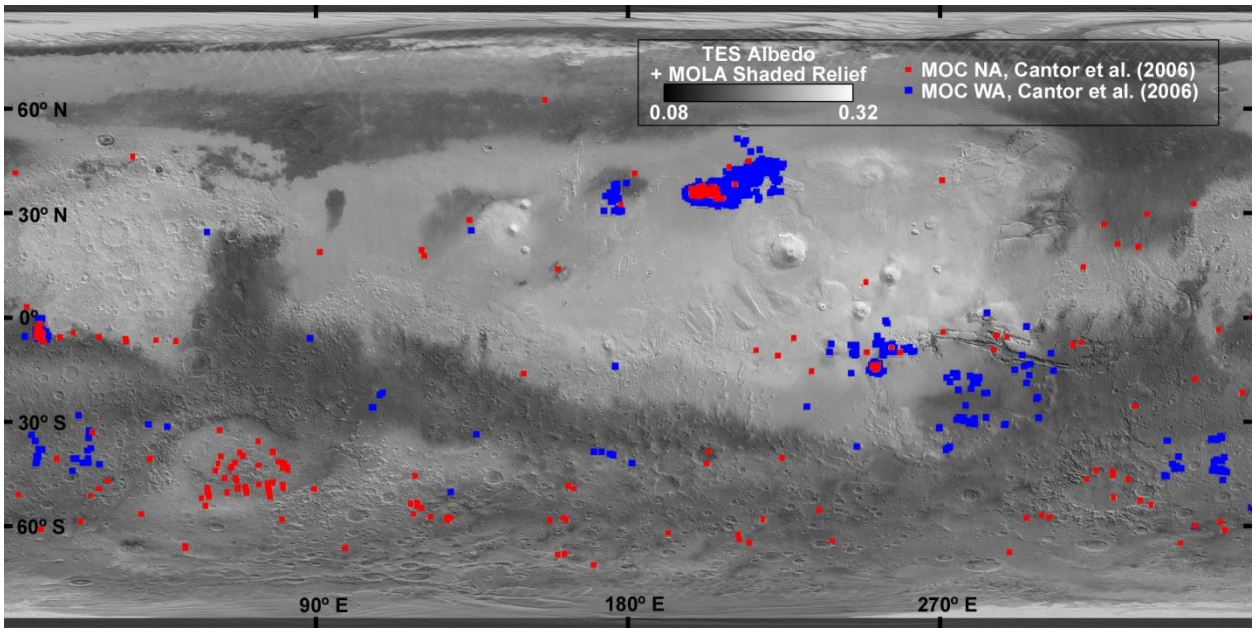

Figure 12. Locations of MOC WA and NA images with DDs identified in the Cetal06 survey, superposed on a composite of TES surface albedo and MOLA shaded relief. Note the high density of DDs in Amazonis Planitia, their widespread distribution in the southern midlatitudes, and the different spatial patterns of DDs detected by the two different cameras.

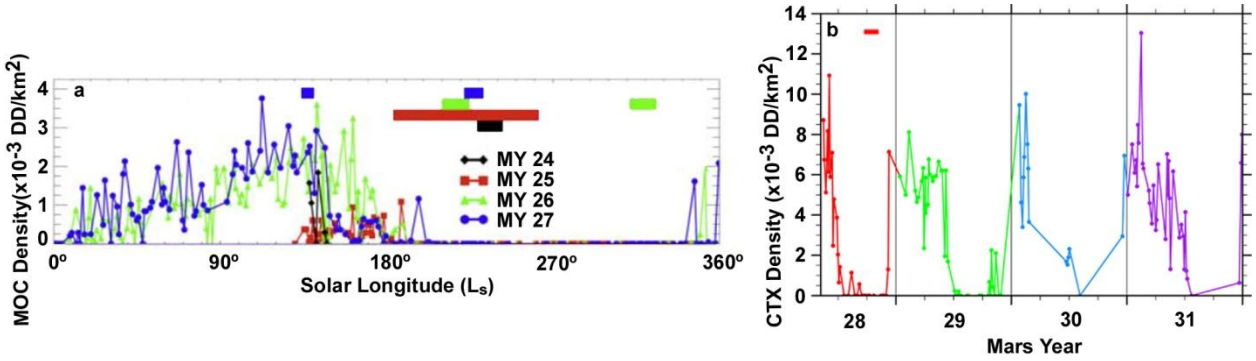

Figure 13. Multiple years of DD densities measured in Amazonis Planitia from a) MOC WA images, modified from Cantor et al. (2006) and b) CTX images, modified from Fenton and Lorenz (2015). Colored bars correspond to the duration of global-scale dust events.

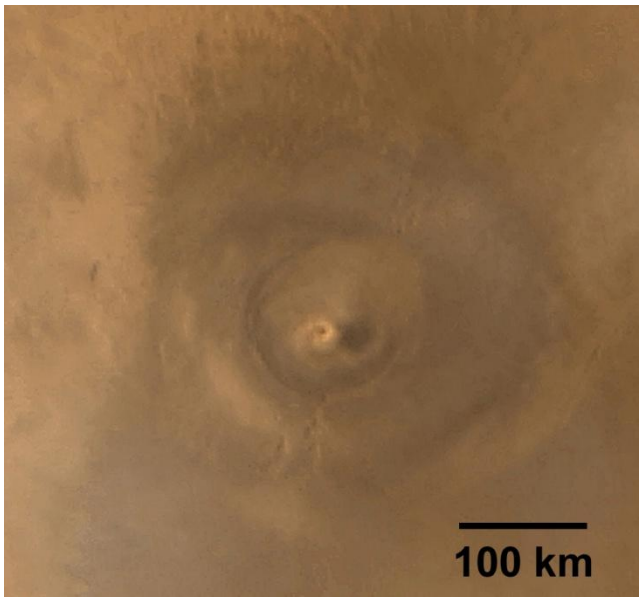

Figure 14. A seasonally-repeating spiral cloud 50 km wide on the caldera floor of Arsia Mons, ~16.3 km above the datum. MOC WA images E05/01721 and E05/01722.

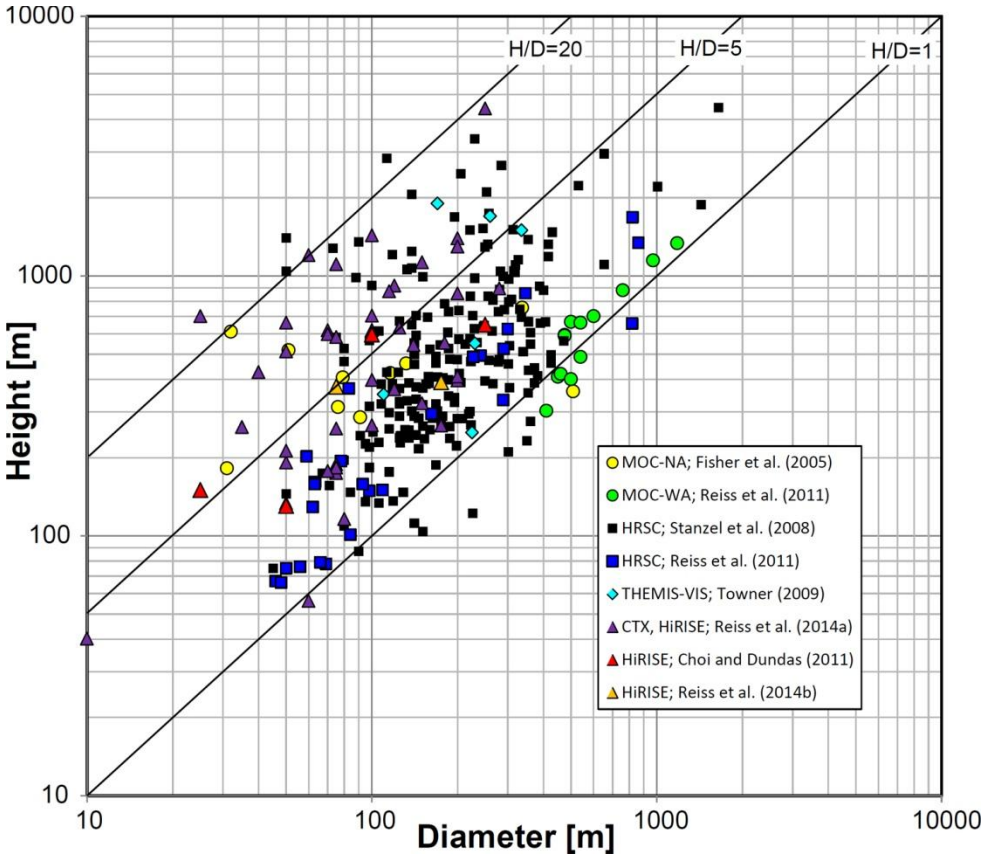

Figure 15. DD diameter vs. height, based on measurements from orbital imagers described in the literature (see Table 4). Black lines show height-to-diameter ratios of 1, 5, and 20. Minimum detectable DD diameter depends on, among other factors, image resolution (see also Fig. 9 and Table 4).

Table 1. Instruments on spacecraft orbiting Earth, discussed in the text, that are or were commonly used to study atmospheric dust.

Mission: Instrument	**Spectral Range (μm)**	**Spatial Resolution (m/px)**	**Footprint Area (km^2) or Coverage**	**Local Time**
TIROS-6 (1962-1963):				
VCS-MA	1 band: visible	2500	$518x10^3$	Various
Meteosat-1 to Meteosat-7:				
MVIRI	0.5-0.9 μm	2500	Full disk	Every 30 min
	5.7-7.1 μm	5000		
	10.5-12.5 μm	5000		
Meteosat-8 to Meteosat-11:				
SEVIRI	1 band: 0.6-0.9 μm	1000	Full disk	Every 15 min
	12 bands: 0.56-14.4 μm	3000		
NOAA-6, NOAA-8, NOAA-10, TIROS-N:				
AVHRR	1 band: 0.55-0.68 μm	1100	Global: 1x/day	07:30, 14:30
	3 bands: 0.725-11.5 μm		Global: 2x/day	
NOAA-7, NOAA-9, NOAA-11 to NOAA-14:				
AVHRR/2	1 band: 0.55-0.68 μm	1100	Global: 1x/day	Various
	4 bands: 0.725-12.5 μm		Global: 2x/day	
NOAA-15 to NOAA-19, Metop-A to Metop-C:				
AVHRR/3	1 band: 0.58-0.68 μm	1100	Global: 1x/day	Various
	5 bands: 0.725-12.5 μm		Global: 2x/day	
ADEOS, Meteor-3 to Meteor-5, Nimbus-7, TOMS Earth Probe:				
TOMS	6 bands: 312.5-380 nm	50 km	Global: 1x/day	Various
Terra, Aqua:				
MODIS	2 bands: 645, 858 nm	250	Global: 1x/day	10:30, 13:30
	5 bands: 0.469-2.130 μm	500	Global: 1x/day	
	29 bands: 0.412-14.235 μm	1000	Global: 2x/day	
MISR (terra)	4 bands: 0.4464-0.8664 μm	250-275	Global: 1x/9 days	10:30
OrbView-2:				
SeaWiFS	8 bands: 0.412-0.865 μm	1100, 4500	Global: 1x/day	12:00
ADEOS-2:				
GLI	29 bands: 0.38-2.21 μm	250	Global: 0.5x/day	10:30
	6 bands: 3.715-12.0 μm	1000	Global: 1x/day	
ADEOS, ADEOS-2, PARASOL:				
POLDER	9 bands: 0.444-10.2 μm	6500	~Global: 1x/day	Various
	3 polarizations			
ICESat:				
GLAS	532, 1064 nm	Horiz.: 66	-	Various
		Vert.: 76.8		
Space Shuttle Discovery:				
LITE	355, 532, 1064 nm	Horiz.: 300	-	Various
		Vert.: 15		
CALIPSO:				
CALIOP	532, 1064 nm	Horiz: 70	-	13:30
	2 polarizations	Vert: 30		

Table 2. Instruments on spacecraft orbiting Mars, discussed in the text, that have been used to study atmospheric dust.

Mission: Instrument	# Bands/Channels: Spectral Range[a] (μm)	Spatial Resolution[b] (m/px)	Footprint Area (km^2)	Local Time
Mariner 9 (14 November 1971 – 27 October 1972):				
IRIS	750: 5-50	110 km/px	~9500	various
VO1 (19 June 1976 – 17 August 1980), VO2 (7 August 1976 – 25 July 1978):				
VIS	5: 0.35-0.7	60-80	~$7x10^3$	
IRTM	broadband: 0.3-3.5 28: 6-30	>1500	>2	various
Phobos 2 (29 January 1989 – 27 March 1989)				
Auguste	2: 1.9, 3.7	occultation	occultation	various
MGS (12 September 1997 – 2 November 2006):				
MOC WA	Red: 0.575-0.625 Blue: 0.4-0.45	230-7000	~21-240x10^3	
MOC NA	0.5-0.9	1.4-13	~10-600	
TES	VNIR: 0.3-2.9 Thermal IR: 5.1-150 300: 5.8-50	~6x3 km/px	~18	~13:00-15:00
MOLA	1.064	160	0.02	
ODY (24 October 2001 – present):				
THEMIS VIS	5: 0.42-0.86	18-70	~300-20x10^3	~14:00-18:00
THEMIS IR	9: 6.8-14.9	100	~840-47x10^3	
MEX (25 December 2003 – present):				
HRSC	4: 0.53-0.97	>12.5	~60-400x10^3	
PFS	1.2-45	10, 20 km/px	100, 400	
OMEGA	0.38-1.05 0.93-5.1	350-12000	various	Various
SPICAM-UV	118-320 nm	various	various	
SPICAM-IR	1-1.7	various	various	
MRO (10 March 2006 – present):				
CTX	1: 0.5-0.8	4.9-10.6	~$8x10^3$	
HiRISE	3: 0.57-0.83	0.25-1	~10-600	
CRISM	545: 0.362-3.920	18-36	various	~14:00-16:00
MARCI	7: 0.258-0.718	1-10 km/px	various	
MCS	broadband: 0.3-3.0 8: 11.8-42.1	sounder	various	

[a]Units are in μm unless otherwise stated. [b]Units are in m/px unless otherwise stated.

Table 3. Global-scale DD surveys on Mars.

Global Survey	Earth Date: YYYY/MM/DD	Mars Date: MY/L_s	Mission: Camera
Thomas and Gierasch (1985)	1976/06/22-1980/07/30	12/84º-14/142º	VO1: VIS VO2: VIS
Fisher et al. (2005)	1999/03/9-2001/07/31	24/107º – 25/206º	MGS: MOC WA MGS: MOC NA MO: THEMIS VIS
Cantor et al. (2006)	1997/09/15-2006/01/21	23/181º – 27/359º	MGS: MOC WA MGS: MOC NA
Stanzel et al. (2008)	2004/01-2006/07	26/325º – 28/86º	MEX: HRSC
Towner (2009)	2004/04/18-2006/03/03	27/20º – 28/19º	MO: THEMIS IR MO: THEMIS VIS
Reiss et al. (2014)	2008/01-2011/12	29/11º-31/50º	MRO: CRISM MRO: CTX MRO: HiRISE

Table 4. The range of DD diameters and heights measured from various orbital platforms on Mars, including the number of DDs measured (*N*).

Reference	Instrument	Minimum resolution (m/px)	*N*	Diameter range (m)	Height range (km)
Thomas and Gierasch (1985)	VO1/VO2 VIS	60	~100	70 - 1000	1 - 2.5
Neumann et al. (2003)	MOLA	~160	7	N/A	8-10
Fisher et al. (2005)	MOC NA	9.28	~25	30 - 510	0.03 - 0.8
Fisher et al. (2005)	MOC WA	230	14	N/A	3.5 - 8.5
Stanzel et al. (2008)	HRSC	12.5	~200	45 - 1650	0.1 - 2.2
Towner (2009)	THEMIS VIS	36	8	110 - 335	0.25 - 1.9
Choi and Dundas (2011)	HiRISE	0.25	4	25 - 250	0.13 - 0.65
Reiss et al. (2011b)	MOC WA	244	13	410 - 1180	0.3 - 1.35
Reiss et al. (2011b)	HRSC	12.5	26	45 - 860	0.06 - 1.7
Reiss et al. (2014a)	CTX or HiRISE	0.25	44	10 - 280	0.04 - 4.4
Reiss et al. (2014b)	HiRISE	0.25	3	75 - 175	0.37 - 0.87
Fenton and Lorenz (2015)	CTX	5.77	2038	N/A	< 0.1 - 16.5
		Mean/median of the above data sets:		220/160	0.63/0.45

Table 5. Translational speeds of martian DDs, including the number of DDs considered (*N*), the observed range, mean and median values.

Method	Reference	*N*	Range (m/s)	Mean, (m/s)	Median, (m/s)
Orbiter images	Stanzel et al. (2008)	194	1-59	13	10.4
	Reiss et al. (2011b)	26	3-22	12	11.1
	Reiss et al. (2014a)	44	4-25	12	11.5
Lander images	Greeley et al. (2010)	498	0.1-27	N/A	1.5-2.5[a]

[a]Range of medians from three analyzed seasons

Table 6. Tangential velocities of DDs on Mars and Earth, including the number of DDs considered (*N*), the mean velocity (V_{mean}), and the maximum velocity (V_{max}).

Method	**Reference**	***N***	V_{mean} **(m s^{-1})**	V_{max} **(m s^{-1})**
Orbiter images (Mars)	Cantor et al. (2006)	1	14.3	
	Choi and Dundas (2011)	4	25	45
In situ (Earth)	Ryan and Carroll (1970)	80	4.2	9.5
	Fitzjarrald (1973)	11	7.3	11.5
	Sinclair (1973)	3	10.8	11.5
	Metzger (1999)	5	13.6	22
	Metzger (2011)	12	11.7	16
Theoretical calculation (Mars)	Renno et al. (2000)	19	11.5	17.7
	Ringrose et al. (2003)	7	16.6	46

Table 7. DD durations on Mars, including the number of DDs measured (*N*), mean and minimum duration, and mean DD diameter.

Method	**Reference**	***N***	**Mean duration (min)**	**Minimum duration (min)**	**Mean diameter (m)**
Orbiter images	Stanzel et al. (2008)	12	13	3.7-32.5	185
	Reiss et al. (2011)	2	N/A	26	700
	Reiss et al. (2011)	1	N/A	74	820
Lander images	Greeley et al. (2006)	533	2.83	0.35-32.27	19
	Greeley et al. (2010)	101	2.15	N/A	24
	Greeley et al. (2010)	127	2.6	N/A	39

Table 8. Comparison of dust loading measurements on Earth and Mars

EARTH			MARS	
Global mean AOT and DOT:				
Data/Model	EY	550 nm AOT	MY (EY)	DOT
MODIS	2002	0.188[a]	25 (00/05-02/04)	*0.67
	2001	0.159[b]	26 (02/04-04/03)	0.43
SeaWiFS	2001	0.124[b]	27 (04/03-06/01)	0.40
	1997-2010	0.13[c]	28 (06/01-07/12)	*0.47
TOMS	2001	0.153[b]	29 (07/12-09/10)	0.38
MISR	2001	0.167[b]	30 (09/10-11/09)	0.33
GOCART	2001	0.118[b]	31 (11/09/13/07)	0.36
	2000-2007	0.14[d]	7 MY mean	0.43
			MY w/o GDE	0.39
Model	EY	550 nm DOT		
GOCART	2000-2007	0.042[d]		
AeroCom	N/A	0.023[e]		
Mineral dust emission (Tg/Earth yr):				
1000-4000[f]			7 MY mean	400-1300
			MY w/o GDE	400-1200
			MY 25	600-2000
Percentage lofted by daytime dry convective turbulence:				
~3.4%[g]			~25-75%[h,i,j]	

*MYs with a global-scale dust event.

Table values from [a]Bellouin et al. (2008), [b]Chin et al. (2014), [c]Hsu et al. (2012), [d]Chin et al. (2009), [e]Huneeus et al. (2011), [f]Boucher et al. (2013), [g]Jemmett-Smith et al. (2015), [h]Cantor et al. (2006), [i]Kahre et al. (2006), [j]Newman et al. (2002b)